2008

The effect of free chlorine and monochloramine on lead in drinking water and epitaxial electrodeposition of tin sulfide

Sansanee Boonsalee

Department: Chemistry

THE EFFECT OF FREE CHLORINE AND MONOCHLORAMINE ON LEAD IN DRINKING WATER AND EPITAXIAL ELECTRODEPOSITION OF TIN SULFIDE

by

SANSANEE BOONSALEE

A DISSERTATION

Presented to the Faculty of the Graduate School of the

MISSOURI UNIVERSITY OF SCIENCE AND TECHNOLOGY

In Partial Fulfillment of the Requirements for the Degree

DOCTOR OF PHILOSOPHY

in

CHEMISTRY

2008

Approved by

Jay A. Switzer, Advisor

Harvest L. Collier

Charles C. Chusuei

F. Scott Miller

Ekkehard Sinn

PUBLICATION DISSERTATION OPTION

This dissertation consists of the following four articles that have been published or submitted for publication:

Pages 35-49 have been published in Environmental Science and Technology.

Pages 50-74 have been published in Environmental Science and Technology.

Pages 75-98 are intended for submission to Environmental Sciences.

Pages 99-116 are intended for submission to Chemistry of Materials.

ABSTRACT

Electrochemical deposition is utilized in various electronic and photovoltaic applications and in the protective coating industries. This dissertation primarily addresses the environmental aspects of electrochemical deposition. In the first part of this study, Pb dissolution in drinking water was investigated in the presence of two disinfectants: free chlorine (in the form of $HOCl/OCl^-$) and monochloramine (NH_2Cl). In the second part of this study, epitaxial SnS nanodisks were electrodeposited onto a Au(100) substrate.

Water utility systems use either free chlorine or monochloramine in their disinfection program. Whereas free chlorine reacts with natural organic matter in the water to produce halogenated organic byproducts that are suspected to be carcinogens, NH_2Cl, a weaker oxidant, may lead to elevated Pb levels in drinking water. Thermodynamically, NH_2Cl is capable of oxidizing Pb and Pb^{2+} species to PbO_2, which is a stable and insoluble oxide of Pb and should minimize the Pb dissolution. However, experimental results utilizing EQCM, XRD, and SEM show that NH_2Cl elevated Pb levels in water by oxidizing Pb or reducing PbO_2 films to soluble Pb^{2+} species. The solubility of PbO_2 in NH_2Cl increases if the concentration of NH_2Cl increases or the pH of the water decreases from pH 10 to pH 7.

Epitaxial films of δ-SnS were deposited electrochemically on single-crystal Au(100) surfaces from an acidic solution at 70 ºC. The films grew with [100] and [301] out-of-plane orientations and four equivalent in-plane orientations. For the SnS(100) orientation, the in-plane mismatch was 2.4% in the [010] direction and 6.1% in the [001] direction. For the (301) orientation, the in-plane mismatch was 2.4% in the [010] direction and 3.4% in the $[10\bar{3}]$ direction. SEM images of the deposit show a disk-like morphology with a diameter of 300 nm and a thickness of 50 nm.

ACKNOWLEDGMENTS

I would like to express my deepest gratitude to my advisor, Dr. Jay A. Switzer, for his guidance, direction, support, and patience throughout my graduate studies. I would also like to thank Dr. Harvest L. Collier, Dr. Ekkehard Sinn, Dr. Charles C. Chusuei, and Dr. Scott Miller for sparing time from their busy schedules to be a part of my graduate committee.

I would like to specially thank Dr. Eric W. Bohannan and Dr. Vishnu V. Rajasekharan for their discussion of the Pb studies and guidance on the Pb project. I also wish to thank my wonderful friend, Elizabeth A. Kulp, for her generous help and emotional support. I would like to express my appreciation to Dr. Hiten Kothari for his help with all aspects of electrochemistry and Dr. Oratai Jongprateep for her generosity and helpful discussion of materials chemistry. I would also like to thank the post-doctoral associates of the Switzer group: Dr. Shuji Nakanishi, Dr. Run Lui, Dr. Philippe Poizot, Dr. Igor Nicic, Dr. Steven Limmer, and Dr. Shaibal Sarkar. I wish to thank fellow group members Rakesh Gudavarthy, Guojun Mu, Niharika Burla, Zhen He, and Brandi Clark. I would also like to thank many faculty members and staff members at the Materials Research Center and in the Department of Chemistry for their assistance. I wish to acknowledge the financial support of the Chemistry Department, the National Science Foundation, and especially the Royal Thai government, who granted me the opportunity to pursue my studies in the United States.

I would like to reserve special thanks for my parents and brother, who have always supported me from a distance, for their unconditional love, encouragement, and endless patience throughout my graduate studies.

TABLE OF CONTENTS

LIST OF ILLUSTRATIONS

Figure Page

INTRODUCTION

PAPER I

PAPER II

PAPER III

PAPER IV

LIST OF TABLES

Table Page

PAPER II

1. INTRODUCTION

This dissertation presents an investigation of the electrodeposition of polycrystalline and epitaxial films on conducting substrates such as polycrystalline and single crystal gold. This low cost room temperature deposition technique is advantageous for the synthesis of metal oxide and metal chalcogenide films. In the first part of the study, lead (Pb) and lead oxide (PbO_2) films were investigated in the presence of free chlorine ($HOCl/OCl^-$) and monochloramine (NH_2Cl) disinfectants. A weaker oxidant, NH_2Cl, increases Pb levels in drinking water by either oxidizing Pb or reducing PbO_2 to soluble Pb^{2+} species. A stronger oxidant, $HOCl/OCl^-$, prevents Pb dissolution by oxidizing Pb and Pb^{2+} to PbO_2 insoluble layers. In the second part of the study, electrochemical deposition was utilized to grow tin sulfide (SnS) films a on Au(100) substrate. The films grew epitaxially with preferred [100] and [301] out-of-plane orientations. In this introduction, background information on the studies described in these papers will be provided.

1.1 BACKGROUND

Electrodeposition offers several advantages as a means of materials synthesis. The technique is fast, inexpensive, and can be used to deposit films onto conducting substrates with different shapes and sizes. Electrodeposition can also be performed at room temperature, which helps minimize solid state diffusion in the film and substrate. As a result, the applications of the electrodeposition technique include semiconductors, protective coatings, metal plating, and energy storage materials. The driving force and deposition rate can be accurately controlled by varying the electrode potential or current

density. The amount of material deposited on the electrode can be determined from the accumulated charge passed during deposition, as stated by Faraday's Law in equation 1.

$$N = \frac{Q}{nF} \tag{1}$$

where N is the number of moles of the material produced at the electrode (mol), Q is the total charge (coulombs), n is the number of electrons, and F is the Faraday constant (96485 C mol^{-1}). If the film is dense, the film thickness (cm) can be estimated using Faraday's Law according to eq 2.

$$\text{thickness} = \frac{QM}{nFA\rho} \tag{2}$$

where M is the molecular weight of the deposit, A is the area of the electrode (cm^2), and ρ is the density of the material (g/cm^3). This technique has been used to deposit a wide variety of materials, including metals,[1,2] ceramics,[3-5] alloys,[6] semiconductors,[7,8] superlattices,[9-12] and superconductors.[13] The focus of the Switzer group at the Missouri University of Science and Technology is electrodepositing nanostructured metal oxide semiconductors, magnetic materials, and catalysts. By varying deposition parameters such as applied current density, potential, pH, solution temperature, and organic additives, the crystallographic orientation of the electrochemically deposited films on polycrystalline and single crystal substrates can be modified. Recently, the group has also published some work on environmental science and biomineralization.[14-16]

Of specific interest in this dissertation is the effect of $HOCl/OCl^-$ and NH_2Cl on Pb and PbO_2 dissolution in drinking water. Films of Pb and PbO_2 were electrodeposited on gold quartz crystals using the redox change method, in which a metal of a low oxidation state that is stable in the deposition solution is reduced or oxidized at the

electrode surface. In this case, Pb^{2+} ions in the deposition bath were reduced to form Pb metal or were oxidized to form PbO_2 films.

Reduction: $Pb^{2+} + 2e^- \rightarrow Pb$ (3)

Oxidation: $PbO + 2OH^- \rightarrow PbO_2 + H_2O + 2e^-$ (4)

It should be noted that PbO is amphoteric and dissolves as biplumbite ions ($HPbO_2^-$) in very strong alkaline solutions.[17] The deposited Pb or PbO_2 films were immersed in disinfectant solutions for mass change monitoring via quartz crystal microbalance (QCM).

The QCM is a versatile gravimetric device with detection limits in the nanogram range.[18] It consists of a thin quartz crystal sandwiched between two metal electrodes that establishes an alternating electric field across the crystal, causing vibrational motion of the crystal at its resonant frequency. The vibrational motion of the quartz crystal establishes a transverse acoustic wave that propagates across the thickness of the crystal, reflecting back into the crystal at the surfaces. When a uniform layer of a foreign material is added to the surface of the quartz crystal, the acoustic wave will travel across the interface between the quartz and the layer and will propagate through the foreign layer.[18] Assuming that the foreign material and the quartz exhibit the acoustic properties, a fractional change in film thickness then results in a fractional change in frequency. This relationship between the change in mass and frequency is known as Sauerbrey equation:

$$\Delta f = \frac{-2 f_0^2 \Delta m}{(\rho \mu)^{1/2} A} \quad (5)$$

where Δf is the measured frequency shift, f_0 is the resonant frequency of the quartz crystal (5 MHz), Δm is the mass change, ρ is the density of quartz (2.648 g/cm^3), μ is the shear modulus of quartz (2.947x10^{11} dyn/cm^2), and A is the piezoelectrically active area.

The ability to expose one side of the QCM as a working electrode in an electrochemical solution while simultaneously measuring mass changes has provided a powerful approach to examining electrochemical processes involving thin films, including monolayer and submonolayer films.[18] Electrochemical quartz crystal microbalances (the abbreviations EQCM and QCM are used to distinguish between electrochemical and nonelectrochemical applications of QCM technology) have been used in wide variety of studies such as underpotential deposition of metals,[19] sensors for heavy metal ions,[20] protein-DNA interaction,[21] and oscillation of Cu/Cu_2O layered nanostructures.[22,23] In this dissertation, the QCM is used to study the dissolution of Pb **(Paper I)** and PbO_2 **(Paper III)** films in disinfectant solutions.

1.2 CHEMICAL THERMODYNAMICS VERSUS KINETICS

For any given chemical reaction, two concepts influence the product distribution: thermodynamics and kinetics. Chemical thermodynamics is concerned with macroscopic properties that can be measured. It is used to predict what types of chemical and physical processes are possible (and under what conditions) and to calculate the final quantity of the products in the state of equilibrium after a process has been carried out. Chemical kinetics, the study of the rates and mechanisms of chemical reactions, gives information about how rapidly a reaction is achieved. For example, perchlorate (ClO_4^-) is a very strong oxidizing agent, yet it is being used as an electrolyte in many electrochemical

studies because the rate at which perchlorate reacts with other redox species in a solution is slow. Therefore, the two concepts are taught separately in most physical chemistry textbooks. In the second paper of this dissertation, electrochemical measurements are used to compare the kinetics and thermodynamics of the electron-transfer reactions of free chlorine and NH_2Cl. The thermodynamics of the two disinfectant reductions are compared by calculating the standard reduction potentials from thermodynamic cycles and by performing equilibrium (open-circuit) potential measurements. The reduction kinetics of the two disinfectants was studied using a Au rotating disk electrode (RDE). The RDE was used to minimize mass transport to the electrode, so that the kinetics can be examined separately from mass transport.

1.2.1 Chemical Thermodynamics. When a chemical reaction has reached equilibrium, the equilibrium constant, K, is related to the free energy (ΔG^o) by the equation

$$\Delta G^\circ = -RT \ln K \tag{6}$$

where R is the molar gas constant (8.314 $mol^{-1}K^{-1}$) and T is the absolute temperature (Kelvin). In an electrochemical cell, ΔG^o is related to a standard electrode potential (E^o) by

$$\Delta G^\circ = -nFE^\circ \tag{7}$$

where n is the number of moles of electrons and F is the Faraday's constant (96485 C mol^{-1}). As a result, the standard electrode potential of any redox couple in both acidic and alkaline solutions can be calculated using eq 6 and 7 assuming that the equilibrium constant is known. The standard electrode potential is defined when an electrochemical reaction has reached its equilibrium and both the oxidized and reduced species are in unit

activity. When the standard state has been deviated, the formal potential for the reaction can be calculate using the Nernst equation:

$$E = E^{\circ} - \frac{RT}{nF} \ln Q \tag{8}$$

where E is the formal potential (V) and Q is the reaction quotient (dimensionless).

An equilibrium potential or open-circuit potential is the electrical potential of an electrode, which is measured against the reference electrode when no current is passing through the electrode. Equilibrium potentials are sometimes referred to in the literature as oxidation-reduction potentials (ORPs).[24] The equilibrium potential of a redox couples can be measured using an inert electrode such as Au or Pt in a solution containing equimolar of the redox species.

In electrochemistry, the current (or electrode reaction rate) is carried by ions in a solution. These groups of ions move in certain directions from the bulk solution to the electrode surface and, thus, produce a drift or flux of ions. A flux of ions fuels the charge-transfer reactions which occur near the electrode surface[25]. This movement of material from one place to another in solution is called mass transfer. If the movement is caused by the concentration gradient, it is called diffusion. If differences in electrostatic potential cause an electric field to be produced in the solution, which in turn results in the movement of ions, it is called migration. Finally, if a difference of pressure or density or temperature causes the liquid to move, this mass transfer mode is called convection.

1.2.2 Kinetics. In an electrochemical cell, the reaction rate is generally governed by mass transfer of species or by the kinetics of the electrode reaction itself. When studying the kinetics of the reaction, care must be taken to exclude mass transfer from kinetic control. Mass transfer effects can be minimized by forced convection of the

solution using a rotating disk electrode (RDE). The standard heterogeneous rate constant (k^o) and the exchange current density (j_0) can be determined using the RDE by both Koutecky-Levich analysis and by a linear approximation to the Butler-Volmer equation used at very low overpotential[26]. Both methods assume that the open circuit potential is known. The Koutecky-Levich equation is given in eq 9.

$$\frac{1}{i} = \frac{1}{i_k} + \frac{1}{i_l} = \frac{1}{i_k} + \frac{1}{0.62nFAD^{2/3}\omega^{1/2}\nu^{-1/6}C} \tag{9}$$

where

i is the measured current (A),

i_k is the current in the absence of mass –transport effects (A),

i_l is the limiting current at high overpotential (A),

n is the number of electrons transferred,

F is Faraday's constant (96485 $Cmol^{-1}$),

A is the electrode area (cm^2),

D is the diffusion coefficient (cm^2s^{-1}),

ω is the angular frequency of rotation (s^{-1}),

v is the kinematic viscosity (cm^2s^{-1}), and

C is the concentration ($molcm^{-3}$)

A plot of $1/i$ vs. $1/\omega^{1/2}$ (also called the Koutecky-Levich plot) should be linear with the intercept equal to $1/i_k$. Determination of i_k at different values of overpotentials then allows determination of the forward rate constant (k_f), the standard heterogeneous rate constant (k^o), and the transfer coefficient (α).

The standard heterogeneous rate constant (k^o) can also be estimated from the Butler-Volmer equation

$$i = i_0\left[e^{-\alpha F\eta/RT} - e^{(1-\alpha)F\eta/RT}\right] \tag{10}$$

where i is the measured current (A), i_0 is the exchange current (A), α is the transfer coefficient (dimensionless), and η is the applied overpotential. At low overpotential (where mass-transport effects are minimal) and for small values of η, the Butler-Volmer equation given in eq 10 becomes eq 11[26].

$$j = \frac{-j_0 F\eta}{RT} \tag{11}$$

where j is the measured current density (Acm^{-2}), and j_0 is the exchange current density (Acm^{-2}). From eq. 11, j_0 can be calculated from the slope of j versus η graph. The standard heterogeneous rate constant (k^o) is related to j_0 by the equation

$$j_0 = nFk^{\circ}C \tag{12}$$

1.3 EPITAXIAL ELECTRODEPOSITION

Epitaxial films are useful in devices such as solar cells or semiconductors because the intrinsic properties of the material, rather than its grain boundaries, can be exploited. Epitaxy can be defined as the "the growth of crystals on a crystalline substrate that determines their orientation."[27] Given this definition, the film's crystallographic orientation for a desired property can be selected by carefully choosing the substrate. Epitaxial films are typically deposited onto single crystal substrates through vapor deposition, for example, molecular beam epitaxy (MBE).[28,29] In MBE, thin films are crystallized via reactions between thermally energetic atomic or molecular beams of the

desired elements on a crystalline substrate that is maintained at an elevated temperature. The entire process takes place in an ultrahigh vacuum. MBE is the first technique to demonstrate monolayer-scale heterostructures. Although widely used, the technique is quite expensive. The growth of epitaxial films by electrodeposition is a low-cost alternative to this process.

Extensive work has been done on epitaxial growth using electrodeposition.[30-34] Single-crystal Cu-Ni strained layer superlattices on Cu(100) have been prepared electrochemically.[12] Lincot has electrodeposited epitaxial CdTe films onto InP(111)[35] and ZnO onto GaN(0002)[36] single crystals. Epitaxial quantum dots of CdSe have been electrochemically prepared on Au(100) substrate.[37] A hybrid electrochemical/chemical method (EC) of semiconductor nanocrystals has been prepared on graphite.[38] The Switzer group has demonstrated that it is possible to form epitaxial films of δ-Bi_2O_3[39], Cu_2O[40,41], CuO[42], ZnO[43,44], Fe_3O_4[45], and α-PbO_2[46] on single-crystal Au. Epitaxial Cu_2O films with tunable morphologies have been deposited on Si and InP single-crystals by the same group.[47-49] This dissertation extends the epitaxial electrodeposition technique of δ-SnS on a Au(100) substrate in **Paper IV**.

In a highly oriented epitaxial film, only reflections from a single set of planes are observed in the standard 2θ x-ray pattern [e.g., (100), (200), (300), etc.]. In order to determine whether the film has an in-plane orientation, it is necessary to examine other reflections that are oriented in-plane with respect to the sample normal. X-ray diffraction pole figures are used to examine the in-plane orientation of the electrodeposited films. To bring other allowed reflections into the Bragg condition, the sample must be tilted using a goniometer. Once the sample is tilted to the appropriate angle (χ) plane, it is then

rotated about the sample normal through the azimuthal angle (φ). If the sample has an in-plane orientation, the azimuthal scan will show separated peaks. If the sample has a fiber texture, the azimuthal scan will consist of no distinct peaks and equal intensity will be observed at all azimuthal angles. The same analysis can be performed on the substrate to determine whether there is a rotation of the film with respect to the substrate. An azimuthal scan is obtained when the measurement is carried out for only one tilt angle, χ. A pole figure is obtained when the measurement is carried out by varying χ from 0-90º. X-ray rocking curves are another analysis that can be used to measure the crystallographic quality (i.e., mosaicity) of the films relative to the substrate.

1.4 EFFECTS OF FREE CHLORINE AND MONOCHLORAMINE ON LEAD IN DRINKING WATER

Controlling lead dissolution from lead service lines, brass fixtures, and solders is a goal for all water utilities systems. According to the U.S. Environmental Protection Agency's Lead and Copper Rule, the action limit for Pb in drinking water is 15 ppb.[50-52] In 2003, elevated Pb levels of up to 48,000 ppb were observed in many water districts, including Washington, D.C. and Greenville, North Carolina.[53-55] One hypothesis about elevated Pb levels is that changing the disinfection program from free chlorine to NH_2Cl could have caused lead leaching.[14,15,55] Free chlorine has traditionally been used as a disinfectant in drinking water because of its ability to inactivate most pathogenic microorganisms.[56] The side effect of using such a strong oxidant is that free chlorine also reacts with organic compounds present in water to produce chlorinated hydrocarbons such as trihalomethanes, which are suspected carcinogens.[57] Switching to a less powerful oxidant, NH_2Cl, seems to lower the water's oxidation reduction potentials(ORPs) which

also cause the PbO_2 protective layers in the Pb service lines to dissolve and the Pb levels to increase.[15,24,58]

Although previous theoretical studies[14,59-62] based on standard reduction potentials suggest that both free chlorine and NH_2Cl are strong enough to oxidize Pb to PbO_2, experimental results and reports in real systems show that only free chlorine forms PbO_2, while NH_2Cl forms Pb(II) species.[14,54,63,64] The quartz crystal microbalance (QCM) is used to compare the effects of free chlorine and NH_2Cl on the dissolution of Pb **(Paper I)** and PbO_2 **(Paper II)** films. The rotating disk electrode is used to estimate the heterogeneous rate constants **(Paper II)**. The equilibrium constants are determined using the polycrystalline Au electrode. The Pb and PbO_2 films are examined by scanning electron microscopy (SEM) and glancing-angle X-ray diffraction.

1.4.1 Experimental. All experiments were conducted using HPLC-grade water. Free chlorine solutions were made from a concentrated sodium hypochlorite solution with 10-13 vol % available chlorine. NH_2Cl solutions were prepared by mixing free chlorine with a 5-fold molar excess of aqueous NH_3 to minimize dichloramine ($NHCl_2$) formation.[65,66] The concentration of free chlorine and NH_2Cl were determined spectrophotometrically using a CARY 5 UV-Vis-NIR spectrophotometer.

Films of Pb or PbO_2 were deposited electrochemically onto Au-coated, commercially available 9 MHz QCM crystals from the solution precursor of Pb^{2+} using a constant current. A quartz crystal analyzer was used to monitor the mass change as a function of time while the film was immersed in a disinfectant solution. The solutions for kinetic studies were maintained at pH 9 using $NaHCO_3$ as a buffer and Na_2SO_4 as an electrolyte. For the equilibrium potential measurements, the potentials were collected

from pH 7 to pH 12 using a polycrystalline Au or Pt as an electrode. NaH_2PO_4, $NaHCO_3$, and H_3BO_3 buffers were used. Grazing incidence X-ray diffraction patterns were obtained using a Philips X'Pert diffractometer with Cu Kα source radiation. SEM micrographs were obtained using a Hitachi model S4700 cold field-emission scanning electron microscope.

1.4.2 Results and Discussion. A total of 112 μg of Pb film is deposited on QCM electrode and then immersed in 1 mM free chlorine or NH_2Cl solution at pH 8. After 22 hrs, the decrease in mass of the Pb film in free chlorine is approximately 5 μg, while the decrease in mass in the NH_2Cl solution is 107 μg (Figure 1). The Pb film turned red after treatment with free chlorine, but white after treatment with NH_2Cl. The glancing-angle XRD patterns reveal that the Pb film is oxidized to α-PbO_2 after treatment with free chlorine, which is consistent with the red color of the film. A weaker oxidant, NH_2Cl, only oxidizes the Pb film to divalent Pb in the form of $Pb_3(CO_3)_2(OH)_2$ or hydrocerrusite, as is confirmed by the XRD. The SEM images show that after treatment in free chlorine the Pb film is covered with nanoscale PbO_2 with a particle size of 11 nm. The Scherrer equation is used to determine the particle size from the broadening of the (111) reflection in the PbO_2's XRD pattern.[67] The unreacted Pb film underneath is also visible in both the XRD scans and SEM images. The surface of the Pb film after NH_2Cl treatment contains only platelets with no unreacted Pb. The results from QCM, SEM, and XRD experiments clearly show that exposing the Pb to NH_2Cl causes the Pb to dissolve and form $Pb_3(CO_3)_2(OH)_2$. Hydrocerrusite is commonly found as a coating on the inside of Pb service lines.[15,68]

To validate the hypothesis that the increase in Pb levels in Washington, DC, is caused by the switch from free chlorine to NH_2Cl, films of α-PbO_2 are electrodeposited on a QCM electrode and treated in NH_2Cl solution to monitor the mass change. Schock et al. have suggested that PbO_2 deposits are formed in chlorinated water if the oxidation-reduction potential (ORP) is maintained at high enough levels.[69,70] These PbO_2 layers are insoluble and stable, which may cause them to serve as passivation layers for Pb-bearing materials. If a weaker oxidant such as NH_2Cl is used, PbO_2 can be reduced to soluble Pb(II) species that can cause the Pb levels to increase.

The QCM results for the 55 μg PbO_2 film immersed in 1 mM free chlorine, 1 mM NH_2Cl, and 1 mM NH_2Cl+0.05 mM phosphate at pH 7 are shown in Figure 2. The mass versus time plots show that the PbO_2 film treated in just NH_2Cl solution has a mass loss of 17 μg, as compared to the film treated in free chlorine solution, which has a mass increase of 0.5 μg. However, when phosphate is added to the NH_2Cl solution, the film is passivated and a mass of 3.5 μg is gained. The SEM image in Figure 3b also shows that the PbO_2 particles dissolved after being treated in NH_2Cl. When phosphate is added to NH_2Cl, the PbO_2 film morphology does not change, as shown in Figure 3d. Instead, fiber-like particles are formed over the PbO_2 deposit. The spot-mode EDS reveals that these fibers contain phosphorous. The glancing-angle XRD patterns in Figure 4 confirm a mixture of crystalline PbO_2 and lead phosphate hydroxide ($Pb_5(PO_4)_3(OH)$. The X-ray pattern of the film after treatment in only NH_2Cl does not contain hydrocerrusite, just crystalline PbO_2 remainder, as shown in Figure 4b. The dissolution of PbO_2 depends on the concentration of NH_2Cl and the solution pH. The rate of dissolution increases at higher NH_2Cl concentrations and at lower pHs.

The kinetics of the reduction of free chlorine and NH_2Cl is carried out using a rotating disk electrode (RDE). The standard heterogeneous rate constant (k_0) and the exchange current density (j_0) can be determined by using both Koutecky-Levich analysis (eq 9) and a linear approximation to the Butler-Volmer equation at low overpotential (eq 10). The methods give similar results for k_0 and j_0. The rate constant and the exchange current density for the reduction of free chlorine (predominantly OCl^- at pH 9) at equilibrium is about twice as large as those for the reduction of NH_2Cl.

The standard reduction potential of the NH_2Cl/Cl^- couple in both acidic and alkaline solutions can be estimated using the thermodynamic cycle **(Paper II)**. Using the equilibrium constant for NH_2Cl hydrolysis (K = 2.63 x 10^{-11}),[71] the standard reduction potentials for NH_2Cl in acidic media (eq 13) and alkaline media (eq 14) can be determined.

$$NH_2Cl + 2H^+ + 2e^- \leftrightarrow Cl^- + NH_4^+ \qquad E^0 = +1.45 \text{ V vs NHE} \qquad (13)$$

$$NH_2Cl + H_2O + 2e^- \leftrightarrow Cl^- + OH^- + NH_3 \qquad E^0 = +0.74 \text{ V vs NHE} \qquad (14)$$

The measured open circuit potentials for NH_2Cl were performed on a polycrystalline Au electrode (area = 0.02 cm^2) in solutions containing equimolar quantities of the redox species in 60 mM buffered solutions, as shown in Figure 5. The solid line in Figure 5 is the calculated formal potential obtained from the Nernst equation (eq 8) at the same molar concentrations. The open circuit potentials (open circles) are approximately 300 mV more negative than the calculated formal potential. The deviation from the calculated potentials may be caused by either an error in the equilibrium constant or the reduction reactions of NH_2Cl not proceeding as shown in eq 13 and eq 14. Competing reactions, such as the production of amidogen radical ($NH_2^{\bullet}$) which can

couple to form hydrazine, can cause the measured open circuit potentials to be different from the calculated formal potentials.[72]

Measuring open circuit potentials in free chlorine and NH_2Cl solutions is important because it may be a useful diagnostic tool for determining the stability of Pb in the presence of these disinfectants. Figure 6 shows the Pourbaix diagram for Pb-H_2O-CO_2 system with the concentration of dissolve Pb species of 15 ppb. The measured open circuit potentials are shown as open squares for free chlorine and as open circles for NH_2Cl. For the operating pH range of drinking water (pH 6.5-8.5), the open circuit potentials for NH_2Cl are in the Pb(II) region, while free chlorine lie in the PbO_2 region. The plot suggests that NH_2Cl is a weaker oxidant that will oxidize Pb^0 or reduce PbO_2 to soluble Pb^{2+} species, increasing the Pb levels in drinking water. Free chlorine will oxidize any form of Pb species only to insoluble PbO_2, forming the protective coating of the Pb service line.

1.4.3 Conclusion. The QCM was used to compare the effect of Pb dissolution in free chlorine ($HOCl/OCl^-$) and monochloramine (NH_2Cl) disinfectant solutions. The EQCM results show that both Pb and PbO_2 films dissolve in NH_2Cl. The kinetic studies reveal that the NH_2Cl rate constant is half as large that of free chlorine. The thermodynamic studies also confirm that NH_2Cl is a weaker oxidant than free chlorine. All experimental results indicate that only free chlorine can oxidize Pb to PbO_2, but NH_2Cl will convert films of Pb and PbO_2 to soluble Pb(II) species at pH lower than 9.5. The PbO_2 dissolution rate depends on pH and the NH_2Cl concentration.

1.5 ELECTRODEPOSITION OF EPITAXIAL TIN SULFIDE NANODISKS ON SINGLE CRYSTAL AU(100)

Tin sulfide is a p-type layered semiconductor with a band gap ranging from 1.05 to 1.48 eV[73-76], which is near the optimum energy bandgap of 1.5 eV required for efficient light absorption for solar energy applications.[77] According to the study by Reddy et al. on optical properties of SnS films at different temperatures, the optical band gap of SnS films strong depends on the lattice parameters.[78] Another investigation by Reddy and co-workers have reported that SnS could have a conversion efficiency as high as 25%.[79] Sn and S are also inexpensive, environmentally benign, and ubiquitous in nature. These properties make SnS suitable for use in making photovoltaic and photoelectrochemical cells.

Epitaxial films are typically deposited onto single crystal substrates using vapor deposition. The advantages of electrochemical deposition over other deposition methods are its versatility, controlability, simplicity, and economy. The electrodeposition is usually carried out at or near room temperature, which helps minimize solid state diffusion between the film and the substrate. The thickness of the film is easily controlled by the charge passed through the electrode. Electrochemical deposition method can be used to deposit materials on substrates of any shape or size. Additionally, the departure from equilibrium is controlled through the applied overpotential and the morphology of the deposits is often dependent on solution additives and pH.

In this dissertation, epitaxial nanostructures of δ-SnS are electrodeposited onto single-crystal Au(100). The high mismatch between the orthorhombic and the

face-centered cubic structure is minimized when the δ-SnS deposits with its *a* axis perpendicularly oriented to the surface of the Au(100) substrate.

1.5.1 Experimental. SnS was deposited using the method developed by Brownson et al.[19] The deposition solution contained 50 mM $SnCl_2$, 150 mM $Na_2S_2O_3$ (sodium thiosulfate), 0.2 M L-tartaric acid, and 0.1 M HCl. The final pH of the solution was adjusted to 2.5 with 6 M NaOH. The bath temperature was maintained at 70 ºC. A standard three-electrode set up was used. Platinum was used as a counter electrode and Ag/AgCl was used as a reference electrode. The working electrode was a Au(100) single crystal with a gold wire fitted around it to serve as an electrical contact. The working electrode was placed in the solution using the meniscus method. Prior to deposition, the working electrode was electropolished and annealed under a H_2 flame. δ-SnS was deposited at a constant cathodic current density of 3 mA/cm^2 for 30 min using an EG&G Princeton Applied Research model 273A potentiostat/galvanostat.

X-ray diffraction (XRD) measurements were taken with a high–resolution Philips X'Pert diffractometer. The XRD scan was obtained using Cu Kα source radiation. Pole figures were run on the same instrument in point-focus mode using a crossed slit collimator as the primary optics and a flat graphite monochrometer as the secondary optics. Stereographic projections were generated using Carine Crystallography Software (version 3.1). Scanning electron microscopy (SEM) images were taken with a Hitachi S-4700 cold field emission SEM at an accelerating voltage of 5 keV.

1.5.2 Results and Discussion. The epitaxial deposition of SnS nanodisks are achieved by electrochemical reduction of $SnCl_2$ in the presence of $Na_2S_2O_3$ as a source of sulfur. The chemistry of tin monosulfide electrodeposition is described by Brownson et

al.[74] The XRD θ-2θ diffraction pattern of the SnS deposit on Au(100) is shown in Figure 7. Only three peaks are observed for SnS, which correspond well to the (200), (400), and (800) reflections of SnS. No other reflections are observed in the 2θ scan, indicating preferential [100] orientation of the film. The lattice parameter, *a*, is determined to be 11.31 Å, which is similar to the δ-SnS polymorph reported by Brownson et al. (*a* = 11.380 Å, *b* = 4.029 Å, *c* = 4.837 Å).[74] To determine the in-plane orientations of the deposit, a SnS(210) pole figure was run as shown in Figure 8a. Two different types of reflections can be seen in the pole figure. To verify the assignment of in-plane orientations from the pole figure, the stereographic projections were generated in Figure 8b-8d. Figure 8d is the stereographic projection resulting when Figure 8b and c are overlaid, then rotated by 90º, 180º, and 270º. By comparing the pole figure to the stereographic projections, the four equally-spaced ($\Delta\varphi$ = 90º) peaks at χ = 54º are determined to correspond to the {100} reflections. The other eight peaks at χ = 64º correspond to the {301} reflection.

For the Sn{100} orientation, the lattice mismatch is calculated as 2.4% in the [010] in-plane direction and 6.1% in the [001] in-plane direction. For the SnS{301} orientation, the mismatches in the [010] are 2.4% and 3.4% in the $[10\bar{3}]$ in-plane direction. The quality of the epitaxial δ-SnS nanostructure can be evaluated via x-ray azimuthal scans and x-ray rocking curves. The average full width at half-maximum (fwhm) of δ-SnS in the azimuthal scan is 3.16º. The average peak intensity of δ-SnS relative to the background is 16 to 1, indicating that δ-SnS has a [100] orientation with little or no fiber texture. The x-ray rocking curve of SnS(400)/(301) indicates that δ-SnS has a [100] out-of-plane orientation with a 2.9º mosaic spread. The scanning electron

micrograph in Figure 9 shows that the δ-SnS deposit has a disk-like structure. The disks are approximately 300 nm in diameter and 50 nm in thickness. The ratio of Sn:S is 1:1.08 when measured by energy-dispersive spectroscopy (EDS).

1.5.3 Conclusion. Epitaxial δ-SnS nanodisks are electrodeposited on Au(100) single crystal using the cathodic deposition approach. The δ-SnS deposit grows with two different out-of-plane orientations of [100] and [301], which are aligned with the Au substrate. The quality of the δ-SnS is analyzed by azimuthal and rocking curve scans. The rocking curve shows that the film has a 2.9º mosaic spread. EDS also confirms a 1:1 Sn to S ratio.

REFERENCES

1. Bockris, J. O'M.; Khan, S. U. M. Surface *Chemistry-A Molecular Level Approach*, Plenum Press: New York, 1993.
2. Budevski, E.; Staikov, G.; Lorenz, W. J. *Electrochemical Phase Formation and Growth: An Introduction to the Initial Stages of Metal Deposition*; Wiley-VCH, Weinheim, Germany, 1996.
3. Switzer, J. A. *Am. Ceram. Soc. Bull*. **1987**, *66*, 1521.
4. Breyfogle, B. E.; Phillips, R. J.; Switzer, J. A. *Chem. Mater*. **1992**, *4*, 1356.
5. Feng, J.; Johnson, D. C. *J. Electrochem. Soc*. **1990**, *137*, 506.
6. Svedberg, E. B.; Mallett, J. J.; Sayan, S.; Shapiro, A. J.; Alexander, J.; Egelhoff, W. F.; Moffat, T. *Appl. Phys. Letts*. **2004**, *85*, 1353.
7. Rajeshwar, K. *Adv. Mater*. **1992**, *4*, 23.
8. Stickney, J. L. *Electroanal. Chem.*; **1999**, *21*, 75.
9. Switzer, J. A.; Shane, M. J.; Phillips, R. J. *Science* **1990**, *247*, 444.
10. Switzer, J. A.; Raffaelle, R. P.; Phillips, R. J. Hung, C. J.; Golden, T. D. *Science* **1992**, *258*, 1918.
11. Switzer, J. A.; Hung, C. J.; Breyfogle, B. E.; Shumsky, M. G.; Van Leeuwen, R.; Golden, T. D. *Science* **1994**, *264*, 1573.
12. Moffat, T. P. *J. Electrochem. Soc*. **1995**, *142*, 3767.
13. Norton, M. L. *Mater. Res. Bull*. **1989**, *24*, 1391.
14. Switzer, J. A.; Rajasekharan, V. V.; Boonsalee, S.; Kulp, E. A.; Bohannan, E. W. *Environ. Sci. Technol*. **2006**, *40*, 3384.

15. Rajasekharan, V. V.; Clark, B. N.; Boonsalee, S.; Switzer, J. A. *Environ. Sci. Technol*. **2007**, *41*, 4252.

16. Kulp, E. A; Switzer, J. A. *J. Am. Chem. Soc*. **2007**, *129*, 15120.

17. Pourbaix, M. *Atlas of Electrochemical Equilibria in Aqueous Solutions*, 2nd ed.; National Association of Corrosion Engineers: Houston, TX, 1974.

18. Buttry, D. A.; Ward, M. D. *Chem. Rev*. **1992**, *92*, 1355.

19. Niece, B. K.; Gewirth, A. A. *Langmuir* **1997**, *13*, 6302.

20. Ng, S. C.; Zhou, X. C.; Chen, Z. K.; Miao, P.; Chan, H. S. O.; Li, S. F. Y.; Fu, P. *Langmuir* **1998**, *14*, 1748.

21. Okanata, Y.; Niikura, K.; Sugiura, Y.; Sawada, M.; Morii, T. *Biochemistry* **1998**, *37*, 5666.

22. Bohannan, E. W.; Huang, L-Y.; Miller, F. S.; Shumsky, M. G.; Switzer, J. A. *Langmuir* **1999**, *15*, 813.

23. Eskhult, J.; Nyholm, L. *J. Electrochem. Soc*. **2008**, *155*, D115.

24. James, C. N; Copeland, R. C.; Lytle, D. A. *Proceeding of the AWWA Water Quality Technology Conference*, San Antonio, TX, November 14-18, 2004; pp1-13.

25. Bockris, J. O'M.; Reddy, A. K. N. Modern *Electrochemistry: An Introduction to an Interdisciplinary Area*, A Plenum/Rosetta Ed.; Plenum Press: New York, 1970.

26. Bard, A. J.; Faulkner, L. R. *Electrochemical Methods: Fundamentals and Applications*, 2nd ed.; John Wiley & Sons: NY, 2001.

27. Bauer, E. G.; Dodson, B. W.; Ehrlich, D. J.; Feldman, L. C.; Flynn, C. P.; Geiss, M. W.; Harbison, J. P.; Matyi, R.; Peercy, P. S.; Petroff, P. M.; Phillips, J. M.; Stringfellow, G. B.; Zangwill, A. *J. Mater. Res*. **1990**, *5*, 852.

28. Herman, M. A.; Sitter, H, Editors, *Molecular Beam Epitaxy-Fundamentals and Current Status*; Springer-Verlag, Berlin, (1989).

29. Meier, H. P.; Giesen, E. V.; Walker, W.; Harder, C.; Krahl, M.; Bimberg, D. *Appl. Phys. Lett*. **1989**, *54*, 433.

30. Pauporte, Th.; Cortes, R.; Froment, M.; Beaumont, B.; Lincot, D. *Chem. Mater*. **2002**, *14*, 4702.

31. Froment, M.; Bernard, M. C.; Cortes, R.; Mokili, B.; Lincot, D. *J. Electrochem. Soc*. **1995**, *142*, 2642.

32. Colletti, L. P.; Flowers, B. H. Jr.; Stickney, J. L. *J. Electrochem. Soc*. **1998**, *145*, 1442.

33. Yang, F. Y.; Liu, K.; Hong, K.; Reich, D. H.; Searson, P. C.; Chien, C. L. *Science* **1999**, *284*. 1335.

34. Mallett, J. J.; Svedberg, E. B.; Vaudin, M. D.; Bendersky, L. A.; Shapiro, A. J.; Egelhoff, W. F. Jr.; Moffat, T. P. *Phys. Rev. B*. **2007**, *75*, 085304.

35. Lincot, D.; Kampmann, A.; Mokili, B.; Vedel, J.; Cortes, R.; Froment, M. *Appl. Phys. Lett*. **1995**, *67*, 2355.

36. Pauporte, T.; Lincot, D. *Appl. Phys. Lett*. **1999**, *75*, 3817.

37. Ruach-Nir, I.; Zhang, Y.; Popovitz-Biro, R.; Rubinstein, I.; Hodes, G. *J. Phys. Chem. B* **2003**, *107*, 2174.

38. Penner, R., Hodes, G., Editors, *Electrochemistry of Nanomaterials*; Wiley-VCH Verlag HmbH, Germany, (2001).

39. Switzer, J. A.; Shumsky, M. G.; Bohannan, E. W. *Science* **1999**, *284*, 293.

40. Bohannan, E. W.; Shumsky, M. G.; Switzer, J. A. *Chem. Mater*. **1999**, *11*, 2289.

41. Switzer, J. A.; Kothari, H. M.; Bohannan, E. W. *J. Phys. Chem. B*. **2002**, *106*, 4027.

42. Switzer, J. A.; Kothari, H. M.; Poizot, P.; Nakanishi, S.; Bohannan, E. W. *Nature* **2003**, *425*, 490.

43. Liu, R.; Vertegel, A. A.; Bohannan, E. W.; Sorenson, T. A.; Switzer, J. A. *Chem. Mater*. **2001**, *13*, 508.

44. Limmer, S. J.; Kulp, E. A.; Switzer, J. A. *Langmuir* **2006**, *22*, 10535.

45. Sorenson, T. A.; Morton, S. A.; Waddill, G. D.; Switzer, J. A. *J. Am. Chem. Soc*. **2002**, *124*, 7604.

46. Vertegel, A. A.; Bohannan, E. W.; Shumsky, M. G.; Switzer, J. A. *J. Electrochem. Soc*. **2001**, *148*, C253.

47. Switzer, J. A.; Liu, R.; Bohannan, E. W.; Ernst, F. *J. Phys. Chem. B*. **2002**, *106*, 12369.

48. Liu, R.; Bohannan, E. W.; Switzer, J. A.; Oba, F.; Ernst, F. *Appl. Phys. Lett.* **2003**, *83*, 1944.

49. Liu, R.; Oba, F.; Bohannan, E. W.; Ernst, F.; Switzer, J. A. *Chem. Mater*. **2003**, *15*, 4882.

50. U.S. Environmental Protection Agency. Drinking water regulations: Maximum contaminant level goals and national primary drinking water regulations for lead and copper, final rule; correction. *Fed. Regis*. **1991a**, *56*, 32112.

51. U.S. Environmental Protection Agency. Maximum contaminant level goals and national primary drinking water regulations for lead and copper, final rule. *Fed. Regis*. **1991b**, *56*, 26460.

52. U.S. Environmental Protection Agency. Drinking water regulations: Maximum contaminant level goals and national primary drinking water regulations for lead and copper, final rule; correcting amendments. *Fed. Regis*. **1992**, *57*, 28785.

53. Johnson, J. *Chem. Eng. News*. **2004**, *82*, 9.

54. Edwards, M.; Dudi, A. *J. Am. Water Works Assoc*. **2004**, *96*, 69.

55. Renner, R. *Environ. Sci. Technol.* **2004**, *38*, 224A.

56. White, G. C. *Handbook of Chlorination and Alternative Disinfectants*; Van Nostrand Reinhold Co.: New York, 1986.

57. U.S. Environmental Protection Agency. National interim primary drinking water regulations; control of trihalomethanes in drinking water. *Fed. Regist*. **1979**, *44*, 68624.

58. Boonsalee, S.; Bohannan, E. W.; Clark, B. N.; Switzer, J. A. Manuscript in preparation.

59. Jolly, W. L. *J. Phys. Chem*. **1956**, *60*, 507.

60. Soulard, M.; Bloc, F.; Hatterer, A. *J. Chem. Soc., Dalton Trans*. **1981**, 2300.

61. Gray, E. T., Jr.; Margerum, D. W.; Huffman, R. P. *ACS Symp. Ser*. **1978**, *82*, 264.

62. Wrona, P. K. *J. Electroanal. Chem*. **1998**, *453*, 197.

63. Renner, R. *Environ. Sci. Technol.* **2005**, *39*, 314A.

64. Renner, R. *Environ. Sci. Technol.* **2004**, *38*, 342A.

65. Yiin, B. S.; Margerum, D. W. *Inorg. Chem*. **1990**, *29*, 2135.

66. Qiang, Z.; Adams, C. D. *Environ, Sci. Technol*. **2004**, *38*, 1435.

67. Cullity, B. D.; Stock, S. R. *Elements of X-ray Diffraction*, 3rd ed.; Prentice Hall: Upper Saddle River, NJ, 2001.

68. Schock, M. R. *J. Am. Water Works Assoc*. **1989**, *81*, 88.

69. Schock, M. R.; Harmon, S. M.; Swertfeger, J.; Lohmann, R. *Proc.-Water Quality Technol. Conf.* **2001**, 2270.

70. Lytle, D. A.; Schock, M. R. *J. Am. Water Works Assoc*. **2005**, *97*, 102.

71. Margerum, D. W.; Schurter, L. M.; Hobson, J.; Moore, E. E. *Environ. Sci. Technol*. **1994**, *28*, 331.

72. Piela, B.; Wrona, P. K. *J. Electrochem. Soc*. **2003**, *150*, E255.

73. Brownson, J. R. S.; Georges, C.; Lévy-Clément, C. *Chem. Mater*. **2006**, *18*, 6397; Brownson, J. R. S.; Georges, C.; Lévy-Clément, C. *Chem. Mater*. **2007**, *19*, 3080.

74. Brownson, J. R. S.; Georges, C.; Larramona, G.; Jacob, A.; Delatouche, B.; Lévy-Clément, C. *J. Electrochem. Soc.* **2008**, *155*, D40.

75. Cheng, S.; Chen, G.; Chen, Y.; Huang, C. *Optical Materials* **2006**, *29*, 439.

76. Cheng, S.; Chen, Y.; Huang, C.; Chen, G. *Thin Solid Films* **2006**, *500*, 96.

77. Partain, L. D. *Solar Cells and Their Applications*; John Wiley & Sons: New York, 1995.

78. Koteeswara Reddy, N.; Hahn, Y. B.; Devika, M.; Sumana, H. R.; Gunasekhar, K. R. *J. Appl. Phys*. **2007**, *101*, 093522.

79. Ramakrishna Reddy, K. T.; Koteeswara Reddy, N.; Miles, R. W. *Sol. Energy Mater. Sol. Cells* **2006**, *90*, 3041.

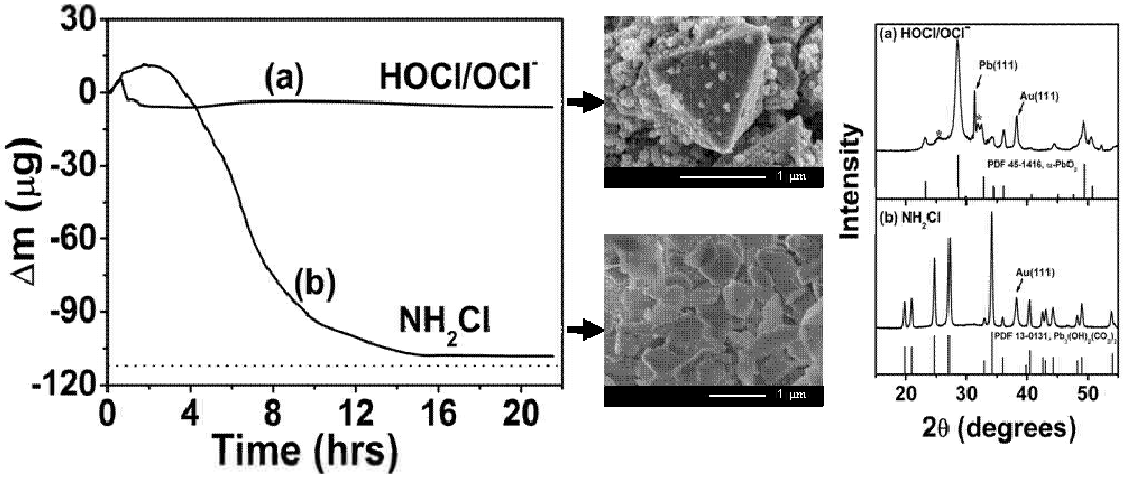

Figure 1: Pb QCM electrodes after treatment in free chlorine and monochloramine solution at pH 8.

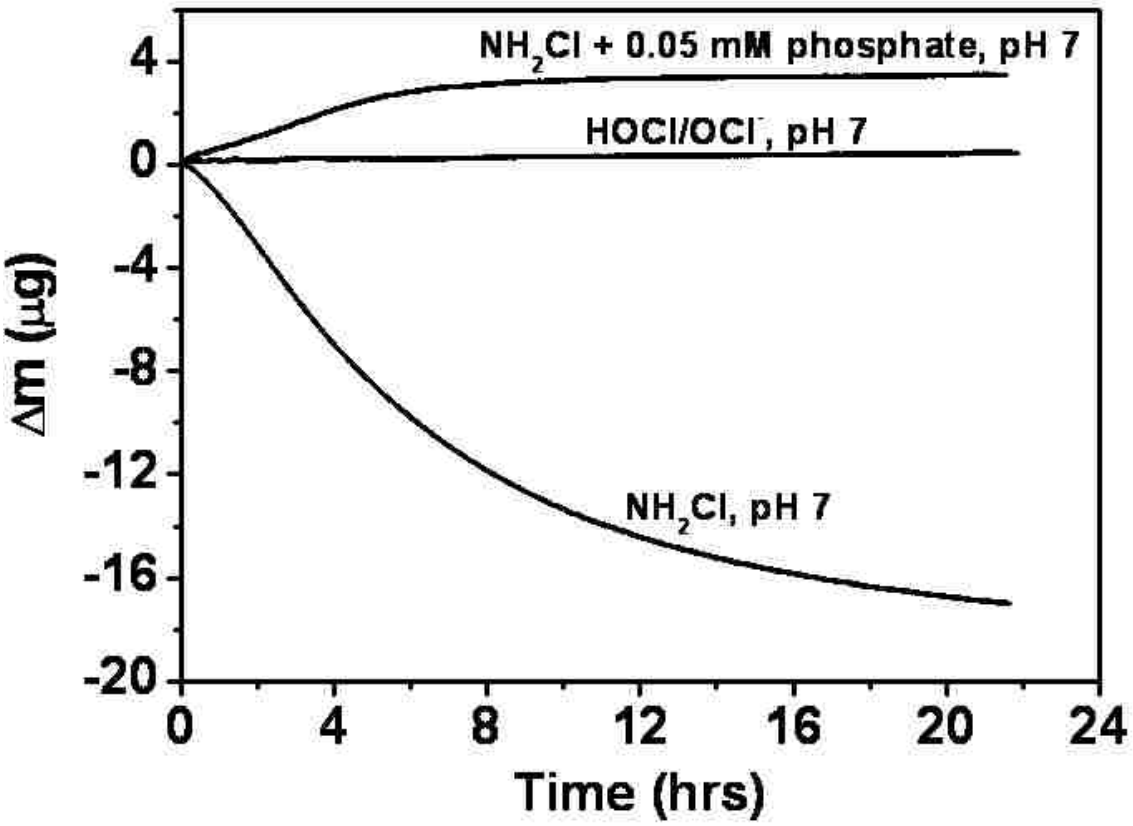

Figure 2: QCM measurements of the change in mass of 0.3 μm thick PbO_2 films immersed in solution at pH 7 of 1 mM NH_2Cl, 1 mM free chlorine, and 1 mM NH_2Cl + 0.05 mM orthophosphate.

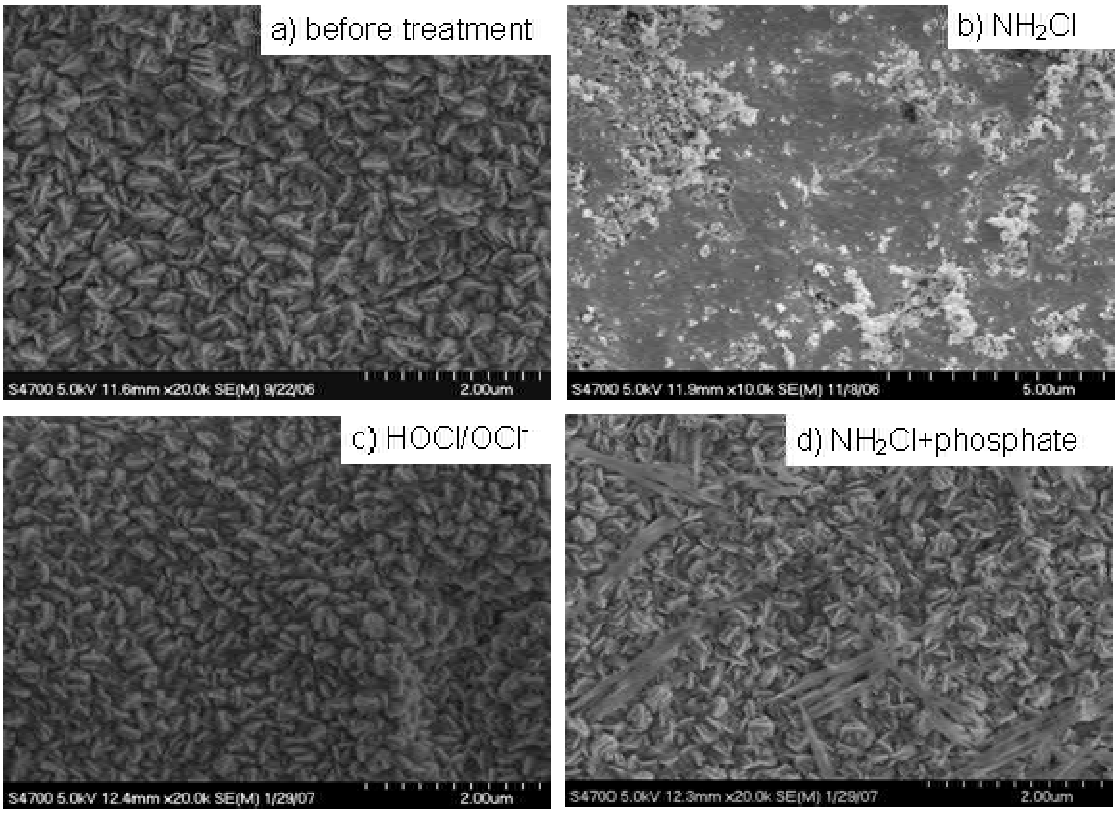

Figure 3: Scanning electron micrographs of 0.3 μm thick PbO_2 films (a) as-deposited, (b) after immersion in 1 mM NH_2Cl at pH 7, (c) after immersion in 1 mM free chlorine at pH 7, and (d) after immersion in 1 mM NH_2Cl + 0.05 mM orthophosphate at pH 7.

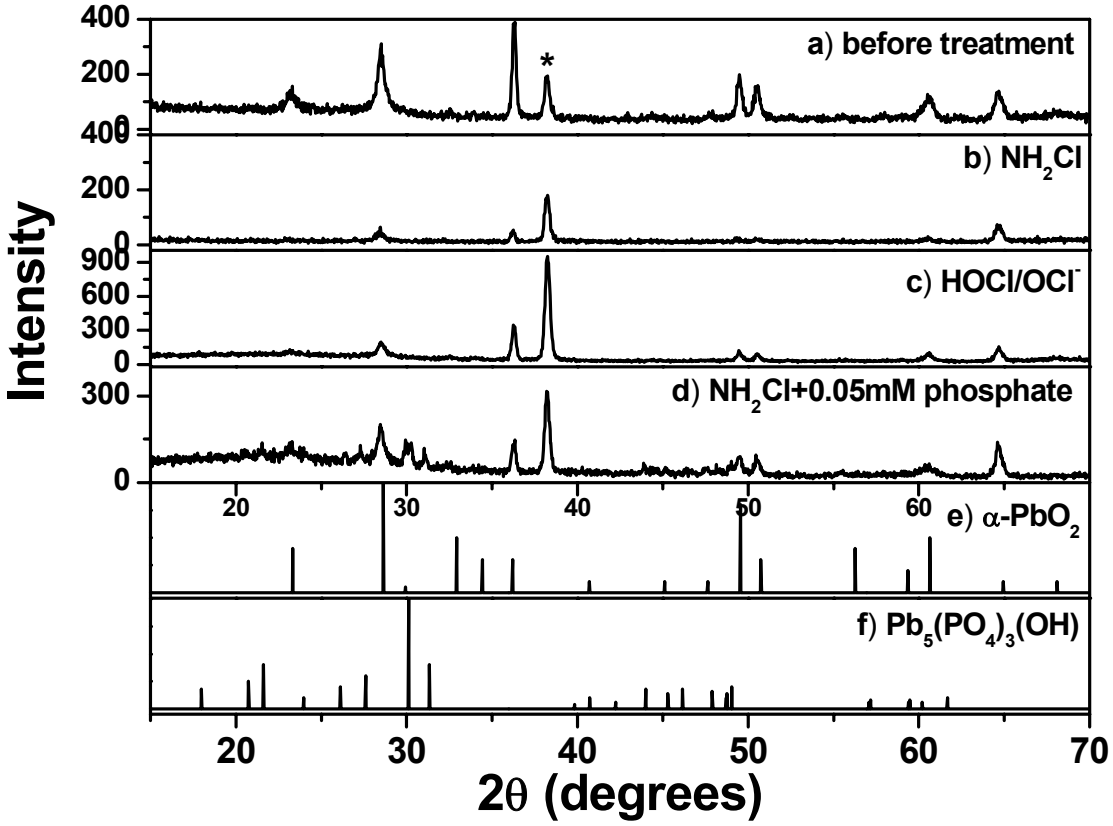

Figure 4: Glancing-angle X-ray diffraction patterns of 0.3 μm thick PbO_2 films (a) as-deposited, (b) after immersion of 1 mM NH_2Cl at pH 7, (c) after immersion of 1 mM free chlorine at pH 7, and (d) after immersion of 1 mM NH_2Cl+0.05 mM orthophosphate at pH 7. The standard powder patterns for (e) α-PbO_2 and (f) $Pb_5(PO_4)_3OH$ are also shown. The Au(111) peaks marked with an asterisk at 2θ = 38.18º are from the Au-coated EQCM electrode.

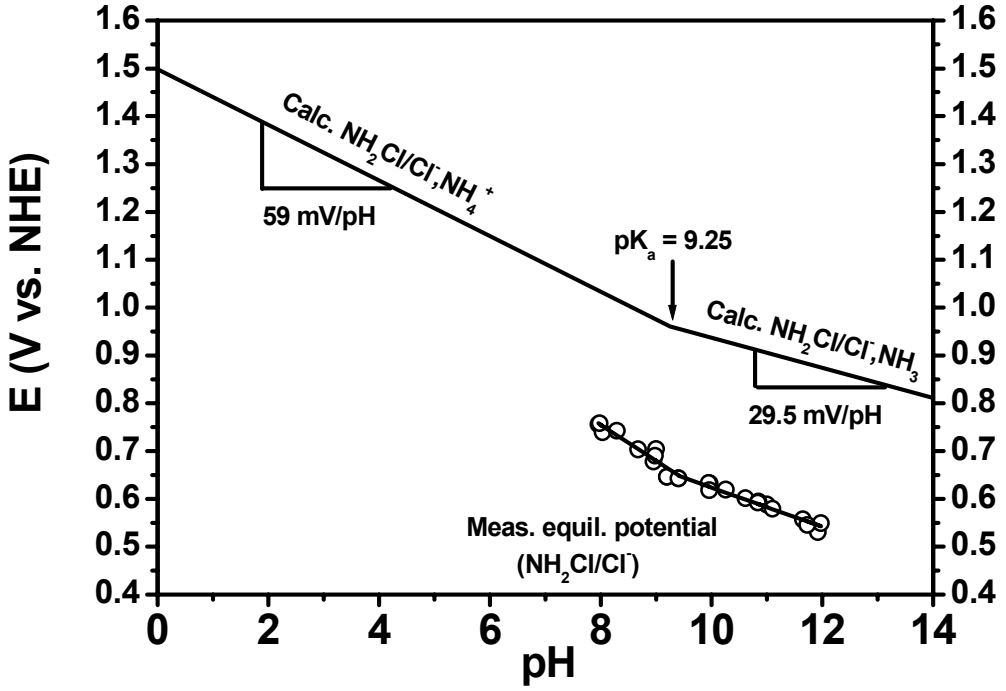

Figure 5: Measured equilibrium potentials (shown as open circles) for the NH_2Cl/Cl^- couple as a function of pH. A linear fit to the measured equilibrium potentials gives two linear regions. Calculated formal potentials from the Nernst equation are also shown as solid lines, which change slope at a pH of 9.25, corresponding to the pK_a of NH_4^+.

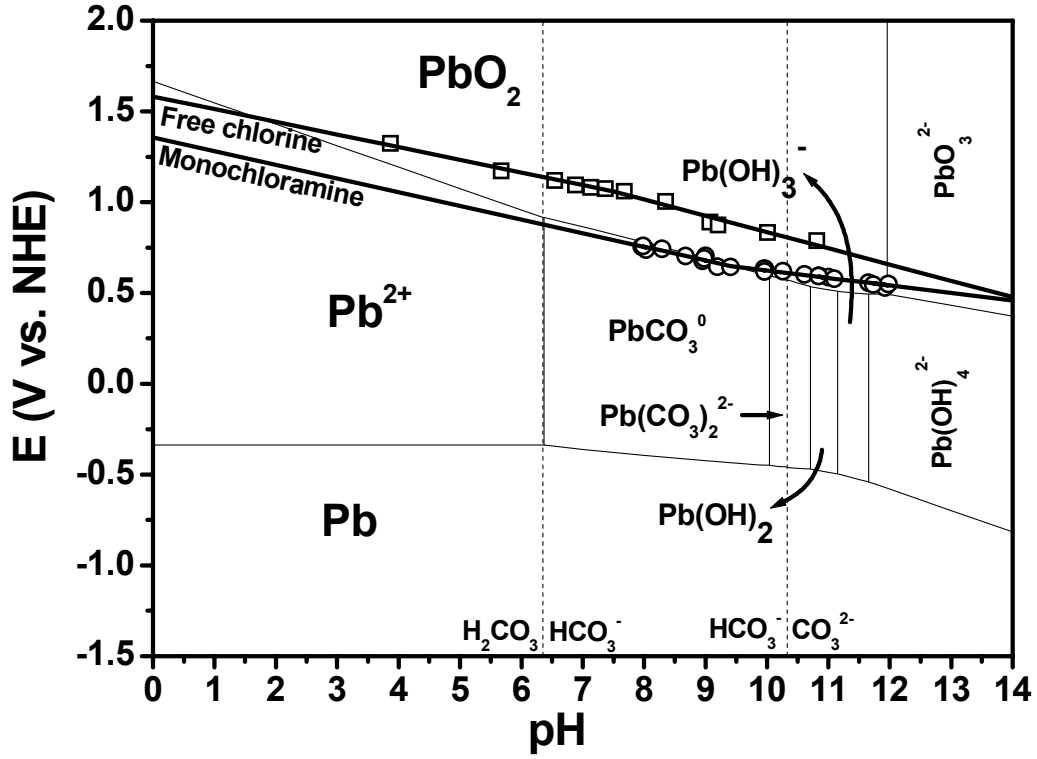

Figure 6: Pourbaix diagram for Pb-H_2O-CO_2 system with the concentration of dissolved Pb species equal to 7.25×10^{-8} M (15 ppb) and the concentration of dissolved inorganic carbon equal to 1.5×10^{-3} M (18 ppm) at 25 ºC. Measured equilibrium potentials are shown as open squares for free chlorine, and as open circles for NH_2Cl. The change in slope for the linear fit to the measured equilibrium potentials for free chlorine corresponds to the pK_a = 7.5 of HOCl.

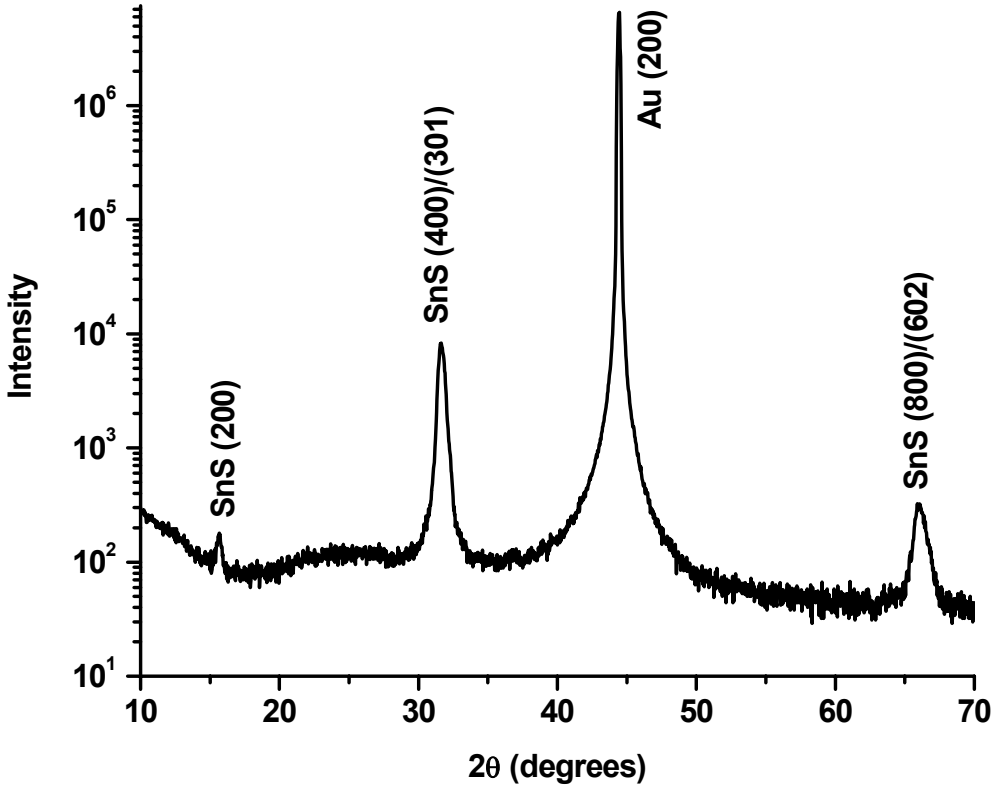

Figure 7: X-ray diffraction θ-2θ scan probing the out-of-plane orientation of a δ-SnS film electrodposited on Au(100).

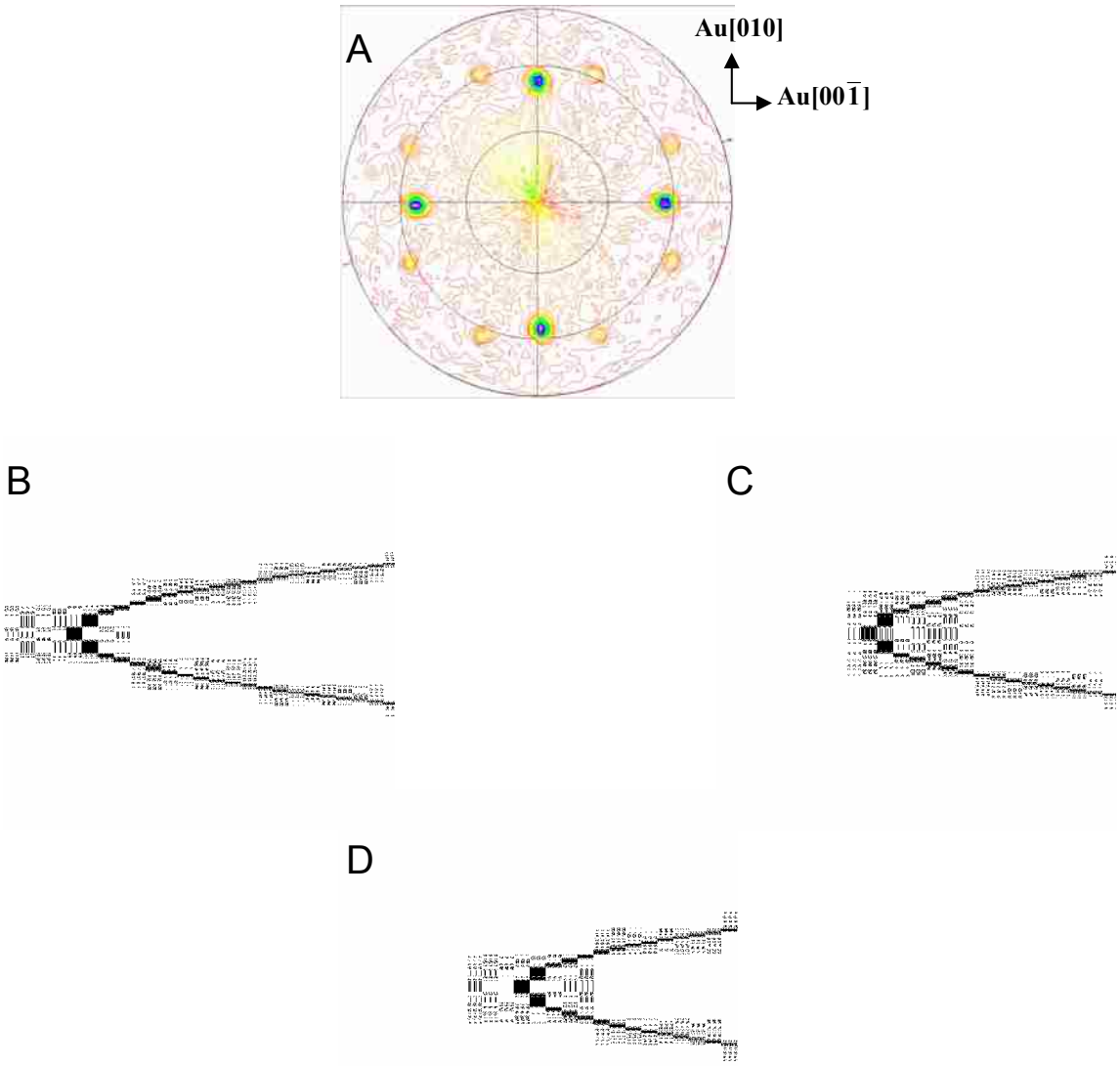

Figure 8: (a) (210) X-ray pole figure of SnS film. The four spots at $\chi = 54^{o}$ correspond to the angles between the (210) and (200) planes, and the eight spots at $\chi = 64^{o}$ correspond to the angles between the (210) and (301) planes. Stereographic projections for (b) SnS(100) and (c) SnS(301) orientations indicating the positions where (210)-type reflections should be observed in the pole figure. (d) Expected (210) stereographic projection for four domains.

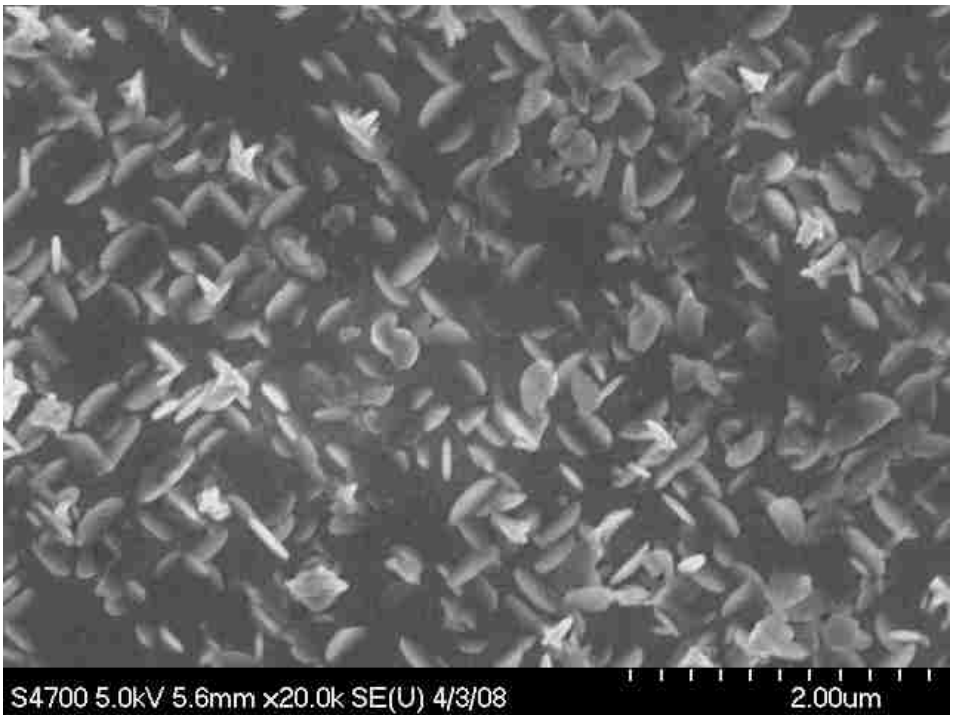

Figure 9: SEM micrograph of an epitaxial SnS on Au(100) showing a nanodisk-like morphology.

PAPER I

Evidence that Monochloramine Disinfectant Could Lead to Elevated Pb Levels in Drinking Water

Jay A. Switzer**, Vishnu V. Rajasekharan, Sansanee Boonsalee, Elizabeth A. Kulp,and Eric W. Bohannan

Department of Chemistry and Graduate Center for Materials Research
Missouri University of Science and Technology, Missouri, U.S.A 65409-1170
Email: jswitzer@mst.edu

Abstract

Many water districts have recently shifted from free chlorine (in the form of $HOCl/OCl^-$) to monochloramine (NH_2Cl) as a disinfectant for drinking water in order to lower the concentration of chlorinated hydrocarbon by-products in the water. There is concern that the use of NH_2Cl disinfectant may lead to higher Pb levels in drinking water. In this study, the electrochemical quartz crystal microbalance is used to compare the effects of these two disinfectants on the dissolution of Pb films. A 0.5 μm thick Pb film nearly completely dissolves in a NH_2Cl solution, but it is passivated in a $HOCl/OCl^-$ solution. X-ray diffraction analysis shows that the NH_2Cl oxidizes Pb to Pb(II) species such as $Pb_3(OH)_2(CO_3)_2$, whereas the stronger oxidant $HOCl/OCl^-$ oxidizes Pb to Pb(IV) as an insoluble PbO_2 conversion coating. Although NH_2Cl may produce less halogenated organic byproducts than $HOCl/OCl^-$ when used as a disinfectant, it may lead to increased Pb levels in drinking water.

Introduction

Free chlorine has traditionally been used as a disinfectant in drinking water because of its ability to inactivate most pathogenic micro-organisms quickly. *(1)* However, chlorine reacts with organic compounds present in the water to produce halogenated organic byproducts such as trihalomethanes (THMs), which are suspected to be carcinogens. *(2)* In 1998, the U.S. Environmental Protection Agency (EPA) established a maximum contaminant limit of 80 ppb for total trihalomethanes in drinking water. *(3)* In an attempt to meet this low level of trihalomethanes, several water utilities have switched from free chlorine (in the form of $HOCl/OCl^-$) to chloramines such as monochloramine (NH_2Cl) because of their lower tendency to produce halogenated organic byproducts. Coincident with the shift from free chlorine to NH_2Cl, some water districts have reported Pb levels in drinking water that exceed the action limit of 15 ppb set by the EPA. Lead levels of up to 48,000 ppb were observed in Washington, DC in the fall of 2003, following their shift from free chorine to NH_2Cl in the year 2000. *(4,5)* Elevated Pb levels were also reported in Greenville, N.C. drinking water after switching from free chlorine to NH_2Cl. *(6)* The monochloramine may lead to high Pb levels by oxidizing Pb in service lines, solder, and brass to soluble Pb(II). *(5,7)* Edwards and Dudi have shown evidence that monochloramine can lead to increased Pb leaching rates from Pb-containing brass fixtures. *(5)* Schock and co-workers have suggested that free chlorine is a powerful enough oxidant that the Pb is passivated by being oxidized to insoluble PbO_2. *(8)* They have shown by X-ray diffraction (XRD) that the Pb service lines in Cincinnati, Ohio are lined with a layer of PbO_2. *(8)* Cincinnati has a history of using free chlorine in their disinfectant program.

In this paper, we use the electrochemical quartz crystal microbalance (EQCM) to compare the effects of NH_2Cl and $HOCl/OCl^-$ on the dissolution of Pb films. The EQCM can measure nanogram changes in mass on the electrode surface while the electrode is immersed in solution by monitoring the changes in resonant frequency of a quartz oscillator. *(9)* We have previously used the EQCM to follow the electrodeposition of layered Cu/Cu_2O nanostructures in real time. *(10)* The EQCM has been used by other groups to study corrosion processes, including anodic corrosion layers on Pb in sulfuric acid. *(11,12)* We also examine the Pb films by scanning electron microscopy (SEM) and glancing-angle XRD after exposure to the two disinfectants.

Experimental

Disinfectant Solutions

All experiments were conducted using HPLC-grade water from Aldrich. A sodium hypochlorite solution with 10-13 vol% available chlorine was used as a source for $HOCl/OCl^-$. Monochloramine and $HOCl/OCl^-$ solutions were prepared fresh for each experiment. The NH_2Cl solutions were prepared by reacting OCl^- with a five-fold molar excess of aqueous NH_3. *(13,14)* The excess NH_3 minimizes the formation of dichloramine ($NHCl_2$). To prepare the NH_2Cl solutions, 5 mL of 100 mM NH_3 was added to a rapidly stirred 20 mL solution of 5 mM NaOCl. The pH was adjusted to 8 with 10 mM H_2SO_4. 1 mL of 100 mM KCl was added as an external Cl^- source, and the solution was diluted to a total volume of 100 mL. The final concentrations in the solution were approximately 1 mM OCl^-, 4 mM NH_4^+, and 1 mM Cl^-. At pH 8 the unreacted ammonia is predominately NH_4^+. The relatively high concentrations of disinfectants in this study were used so that the concentration of the disinfectants remained relatively

constant during the corrosion studies, and because the concentrations of the 1 mM solutions could be determined spectrophotometrically. The actual concentrations of OCl^- and NH_2Cl were determined spectrophotometrically at 292 nm ($\varepsilon = 350\ M^{-1}cm^{-1}$) and 243 nm ($\varepsilon = 461\ M^{-1}cm^{-1}$), respectively, using molar absorptivities from the literature. *(13)* The spectrophotometric measurements were made with a CARY 5 UV-Vis-NIR spectrophotometer.

Pb Electrodeposition and Dissolution

Films of Pb were electrodeposited with an EG&G model 273A potentiostat/galvanostat. The polycrystalline Pb films were electrodeposited at a constant current density of 15 mA/cm^2 from a solution of 0.1 M $Pb(ClO_4)_2$ in 1 M $HClO_4$. The films were deposited onto Au-coated, commercially-available 9 MHz AT-cut quartz crystals (Seiko model QA-AM9-Au) that were used for the EQCM experiments. The Pb films were used immediately after deposition for the EQCM studies. XRD analysis showed that the films were Pb, with no evidence of PbO. The EQCM electrodes were installed in a Teflon holder so that only one electrode face with an area of 0.2 cm^2 was exposed to the solution. The total mass of Pb deposited was 112 μg. The electrodeposited Pb films were then exposed to separate 35 mL unstirred 1 mM solutions of NH_2Cl and $HOCl/OCl^-$. Each solution was adjusted to a pH of 8, and contained 1 mM Cl^-. No effort was made to exclude dissolved CO_2 from the $HOCl/OCl^-$ and NH_2Cl solutions. The mass of Pb was determined as a function of time after treatment with the two disinfectants by monitoring the frequency change of the EQCM electrode using a quartz crystal analyzer (Seiko model QCA917). A gate time of 1 s and an output range of ±20 kHz/10 V were used with the analyzer. The concentration of Pb in the solutions after

the treatment with the two disinfectants was determined by flame atomic absorption spectroscopy using a Varian model SpectrAA 50 atomic absorption spectrometer with a Pb lamp of 217 nm wavelength. The detection limit of the instrument is approximately 0.1 ppm. Solutions were not filtered prior to atomic absorption analysis.

XRD and SEM Instrumentation

Grazing incidence x-ray diffraction (XRD) patterns were obtained with a Philips X'Pert diffractometer using Cu Kα source radiation with an x-ray mirror (PW3088/60) as the incident beam module and a 0.18° parallel plate collimator as the diffracted beam module. A fixed incident angle of 1° was maintained and the instrument was operated in the continuous mode with a step size of 0.03° and a counting time of 10 seconds. SEM micrographs were obtained with a Hitachi model S4700 cold field-emission scanning electron microscope.

Results and Discussion

Figure 1 shows the mass of the Pb electrode as a function of time in the NH_2Cl and $HOCl/OCl^-$ solutions. The Pb dissolves to a much greater extent in the NH_2Cl solution than it does in the $HOCl/OCl^-$ solution. The decrease in mass of the 112 μg Pb film in the $HOCl/OCl^-$ is about 5 μg, while the decrease in mass in the NH_2Cl solution is 107 μg. The Pb film turned red after treatment with $HOCl/OCl^-$, and it turned white after treatment with NH_2Cl. The red color after treatment with $HOCl/OCl^-$ is consistent with the formation of PbO_2 on the electrode surface. We have shown in unpublished experiments that reddish-brown PbO_2 powder (verified by x-ray diffraction) is formed when $HOCl/OCl^-$ is added to a pH 8 aqueous solution of Pb(II). Figure 2 shows SEM

micrographs of electrodeposited Pb films after treatment with the two disinfectants. The Pb film is covered with nanometer scale crystallites after the $HOCl/OCl^-$ treatment (Figure 2a), while the surface contains platelets after the NH_2Cl treatment (Figure 2b). Glancing-angle XRD analysis of the films shows that the film treated with $HOCl/OCl^-$ contains primarily α-PbO_2 and unreacted Pb, with a small amount of β-PbO_2 (Figure 3a). The minor peaks due to β-PbO_2 are marked with an asterisk in Figure 3a. Based on the line broadening in the XRD pattern, the crystallite size of the α-PbO_2 is 11 nm. The crystallite size was calculated from the broadening of the (111) reflection of PbO_2 using the Scherrer equation. *(15)* The triangular facets in Figure 2a are [111]-oriented Pb covered with a conversion coating of nanocrystalline PbO_2 produced by the $HOCl/OCl^-$ oxidation. The film treated with NH_2Cl contains only divalent Pb in the form of hydrocerrusite, $Pb_3(OH)_2(CO_3)_2$, with no evidence of PbO_2 or unreacted Pb (Figure 3b). The EQCM, SEM, and XRD experiments show that exposing the Pb to NH_2Cl causes the Pb to dissolve and form $Pb_3(OH)_2(CO_3)_2$. Hydrocerrusite is commonly found as a coating on the inside of Pb service lines.*(16)*

After the Pb films were treated with the two disinfectants, the solutions were analyzed for Pb by atomic absorption spectroscopy (AA). The AA analysis showed 0.2 ppm (close to the 0.1 ppm detection limit) Pb for the solution containing $HOCl/OCl^-$ and 1.7 ppm Pb for the NH_2Cl containing solution. The greater dissolution of Pb in the NH_2Cl solution is consistent with the higher solubility of $Pb_3(OH)_2(CO_3)_2$ compared with PbO_2. The K_{sp} values for $Pb_3(OH)_2(CO_3)_2$ and PbO_2 are $10^{-18.8}$ and 10^{-66}, respectively.*(17,18)*

The standard reduction potential of the NH_2Cl/Cl^- couple in both acidic and alkaline solutions can be estimated using the equilibrium constant for Equation 1 that was

determined by Margerum and co-workers from kinetic measurements *(19)*, the standard reduction potentials for HOCl/Cl^- and OCl^-/Cl^-, and the pKa for NH_4^+/NH_3 (pKa = 9.25). *(20)* The calculated standard reduction potential for NH_2Cl in alkaline solution (Equation 2) is +0.69 V vs. NHE, and the calculated standard reduction potential for NH_2Cl in acidic solution (Equation 3) is +1.4 V vs. NHE. The standard reduction potentials for free chlorine and PbO_2 reduction in equations 4-7 are taken from the literature. *(20)*

$NH_3 + HOCl \leftrightarrows NH_2Cl + H_2O$	$K = 3.8 \times 10^{10}\ M^{-1}$	(1)
$NH_2Cl + H_2O + 2e^- \leftrightarrows Cl^- + OH^- + NH_3$	$E° = +0.69$ V vs. NHE	(2)
$NH_2Cl + 2H^+ + 2e^- \leftrightarrows Cl^- + NH_4^+$	$E° = +1.4$ V vs NHE	(3)
$OCl^- + H_2O + 2e^- \leftrightarrows Cl^- + 2OH^-$	$E° = +0.81$ V vs. NHE	(4)
$HOCl + H^+ + 2e^- \leftrightarrows Cl^- + H_2O$	$E° = +1.482$ V vs. NHE	(5)
$PbO_2 + H_2O + 2e^- \leftrightarrows PbO + 2OH^-$	$E° = +0.247$ V vs. NHE	(6)
$PbO_2 + 4H^+ + 2e^- \leftrightarrows Pb^{2+} + 2H_2O$	$E° = +1.455$ V vs. NHE	(7)

Free chlorine (HOCl/OCl^-) is a slightly stronger oxidizing agent than NH_2Cl in both acidic and alkaline media than, consistent with our results. Because the pKa of HOCl is 7.40 *(20)*, the free chlorine is predominately OCl^- at pH 8. At this pH the solution is 80 mol% OCl^- and 20 mol% HOCl. We cannot determine from our experiments whether OCl^- or HOCl is the active species in the oxidation reactions.

The standard reduction potentials shown for Equations 2 through 7 are for all of the reactants and products at unit activity. Formal reduction potentials for these reactions at pH 8 can also be estimated from the Nernst equation for the concentrations used in this study, and for Pb^{2+} concentrations at the action limit of 15 ppb (7.2×10^{-8} M). Formal reduction potentials for the NH_2Cl/Cl^-, HOCl/Cl^-, OCl^-/Cl^-, and PbO_2/Pb^{2+} couples are 1.0 V, 1.25 V, 1.17 V, and 0.72 V vs. NHE, respectively. Hence, both disinfectants are thermodynamically capable of oxidizing Pb(II) to PbO_2 according to these calculations.

The fact that NH_2Cl does not produce a passivating PbO_2 layer suggests that there is either an error in the calculated standard reduction potentials for Equations 2 and 3 due to uncertainty in the equilibrium constant for Equation 1 *(21,22)*, or that the kinetics of oxidation by NH_2Cl are not facile. We have performed measurements of the equilibrium potentials of monochloramine and free chlorine at pH 8 by measuring the open-circuit potential of a Pt electrode in solutions of the same concentrations that were used in this study. The potentials were measured versus a saturated calomel electrode (SCE), and then converted to the normal hydrogen electrode by adding 0.242 V. The equilibrium potentials that we measured for monochloramine and free chlorine at pH 8 were 0.65 V and 1.02 V vs. NHE, respectively. These measured equilibrium potentials are more consistent with our experimental results than the calculated formal potentials, because they predict that NH_2Cl will oxidize Pb to Pb(II), but it is not a powerful enough oxidant to produce PbO_2. These equilibrium potential measurements suggest that a modern electrochemical study (e.g., rotating disk voltammetry) of the thermodynamics and kinetics of the reduction of both free chlorine and NH_2Cl is warranted.

Free chlorine and monochloramine are not simple outer-sphere electron transfer agents. Margerum *et al.* have shown, for instance, that the oxidation of nitrite ion by NH_2Cl proceeds by acid-catalyzed transfer of Cl^+ from NH_2Cl to NO_2^- to produce NO_2Cl as an intermediate. *(19)* The mechanism of oxidation of Pb by NH_2Cl is probably more complicated than the simple electron transfer that is suggested in Equations 2 and 3. Our EQCM studies do show, however, that NH_2Cl is capable of dissolving Pb by producing Pb(II). Treatment of the Pb with $HOCl/OCl^-$ leads to lower Pb dissolution, due to the production of a conversion coating of PbO_2 on the Pb. Although NH_2Cl may produce less

halogenated organic byproducts than free chlorine when used as a disinfectant in drinking water, it may lead to increased Pb levels.

Acknowledgment

This work was supported by NSF grants CHE-0437346, CHE-0243424, and DMR-0504715.

References

(1) White, G. C. *Handbook of Chlorination and Alternative Disinfectants*; Van Nostrand Reinhold Company: New York, 1986; pp 256-393.

(2) *National interim primary drinking water regulations; control of trihalomethanes in drinking water;* U.S. Environmental Protection Agency: Washington, DC, Federal Register **1979**, *44*, pp 68624-68707.

(3) *National primary drinking water regulations: disinfectants and disinfectants byproducts;* U.S. Environmental Protection Agency: Washington, DC, Federal Register **1998**, *63*, pp 69390-69476.

(4) Johnson, J. Drinking water review planned. High lead levels in Washington, D.C., water trigger broad research study. *Chem. Eng. News*. **2004**, *82*, 9-10.

(5) Edwards, M.; Dudi, A. Role of chlorine and chloramines in corrosion of lead-bearing plumbing materials. *J. Am. Water Works Assoc.* **2004**, *96*, 69-81.

(6) Renner, R. Chloramines again linked to lead in drinking water. *Environ. Sci. Technol.* **2005**, *39*, 314A-315A.

(7) Renner, R. Plumbing the depths of D. C.'s drinking water crisis. *Environ. Sci. Technol.* **2004**, *38*, 224A-227A.

(8) Schock, M. R.; Harmon, S. M.; Swertfeger, J.; Lohmann, R. Tetravalent lead: a hitherto unrecognized control of tap water lead contamination. *Proceedings–Water Quality Technology Conference*, Nashville, TN; American Water Works Association: Denver, CO, **2001**, 2270-2291.

(9) Buttry, D. A.; Ward, M. D. Measurement of interfacial processes at electrode surfaces with the electrochemical quartz crystal microbalance. *Chem. Rev.* **1992**, *92*, 1355-1379.

(10) Bohannan, E. W.; Huang, L.-Y.; Miller, F. S.; Shumsky, M. G.; Switzer, J. A. In situ electrochemical quartz crystal microbalance study of potential oscillations during the electrodeposition of Cu/Cu_2O layered nanostructures. *Langmuir* **1999**, *15*, 813-818.

(11) Wang, K.; Pickering, H. W.; Weil, K. G. Corrosion inhibition of zinc by benzotriazole with an electrochemical quartz crystal microbalance. *J. Electrochem. Soc.* **2003**, *150*, B176-B180.

(12) Wei, C.; Rajeshwar, K. In situ characterization of lead corrosion layers by combined voltammetry, coulometry, and electrochemical quartz crystal microgravimetry. *J. Electrochem. Soc.* **1993**, *140*, L128-L130.

(13) Yiin, B. S.; Margerum, D. W. Non-metal redox kinetics: reactions of trichloramine with ammonia and with dichloramine. *Inorg. Chem.* **1990***, 29*, 2135-2141.

(14) Qiang, Z.; Adams, C. D. Determination of monochloramine formation rate constants with stopped-flow spectrophotometry. *Environ. Sci. Technol.* **2004***, 38*, 1435-1444.

(15) Cullity, B. D.; Stock, S. R. *Elements of X-ray Diffraction*, 3rd Edition, Prentice Hall: New Jersey, 2001.

(16) Schock, M. R. Understanding corrosion control strategies for lead. *J. Am. Water Works Assoc.* **1989**, *81*, 88-100.

(17) Graedel, T. E. Chemical mechanisms for the atmospheric corrosion of lead. *J. Electrochem. Soc.* **1994,** *141*, 922-927.

(18) Schock, M. R.; Gardels, M. C. Plumbosolvency reduction by high pH and low carbonate-solublity relationships. *J. Am. Water Works Assoc.* **1983***, 75*, 87-91.

(19) Margerum, D. W.; Schurter, L. M.; Hobson, J.; Moore, E. E. Water chlorination chemistry: nonmetal redox kinetics of chloramines and nitrite ion. *Environ. Sci. Technol.* **1994**, *28*, 331-337.

(20) *CRC Handbook of Chemistry and Physics*; Lide, D. R., editor; 86th Edition; Taylor and Francis Group: Florida, 2005.

(21) Anbar, M.; Yagil, G. The hydrolysis of chloramines in alkaline solution. *J. Am. Chem. Soc.* **1962**, *84*, 1790-1796.

(22) Gray, E. T.; Margerum, D. W.; Huffman, R. P. Chloramine equilibriums and the kinetics of disproportionation in aqueous solution. *ACS Symposium Series* **1978**, *82*, 264-277.

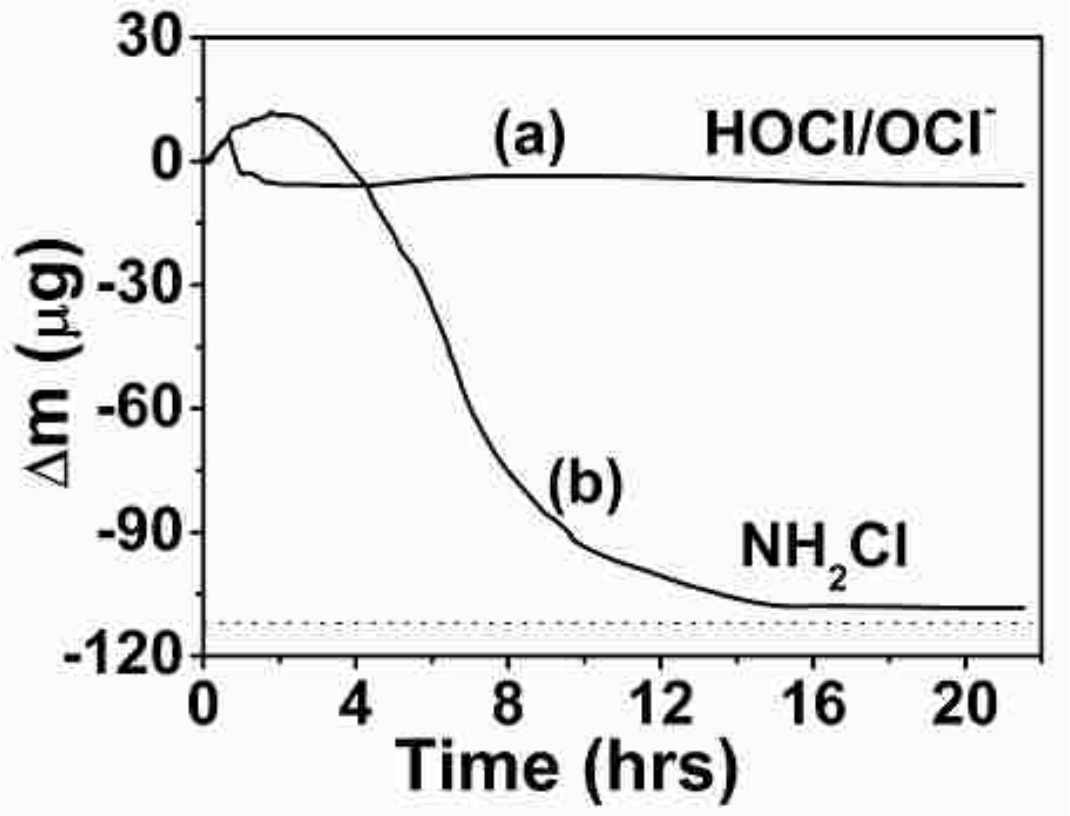

Figure 1: EQCM measurement of the change in mass of 0.5 μm thick Pb films immersed in 1 mM solutions of (a) $HOCl/OCl^-$ and (b) NH_2Cl at pH 8. Dissolution of Pb is greater in the NH_2Cl solution. The dashed line corresponds to total dissolution of the 112 μg Pb film.

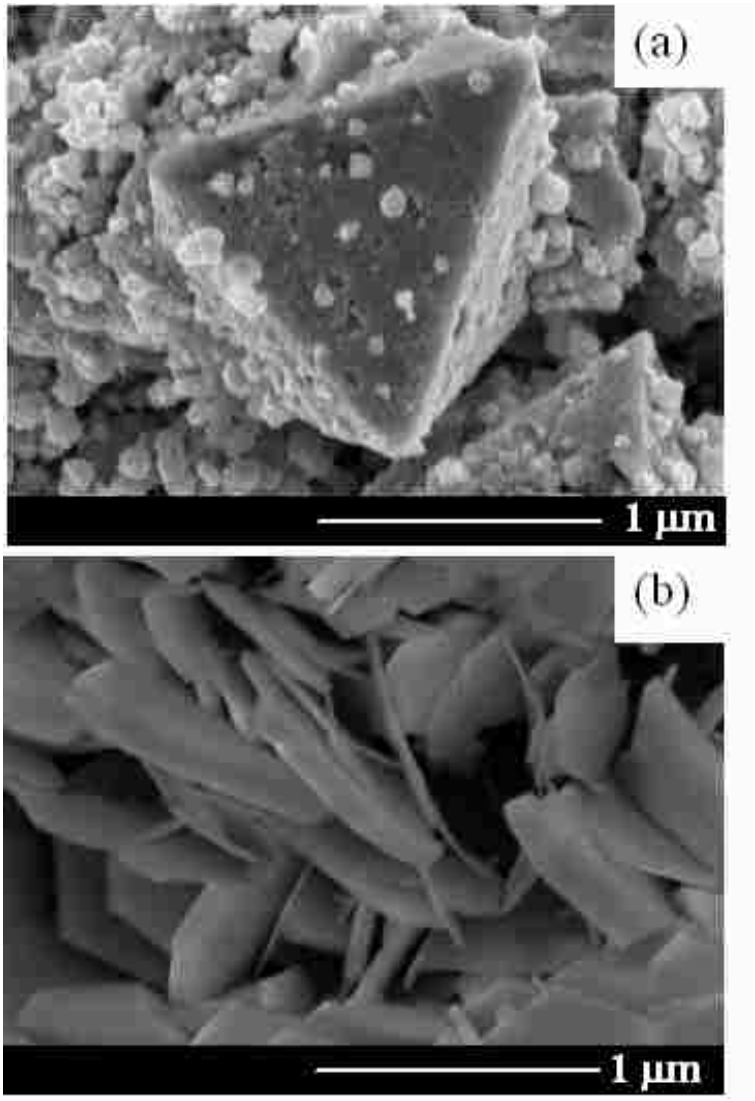

Figure 2: Scanning electron micrographs of 0.5 µm thick Pb films immersed in 1 mM solutions of (a) $HOCl/OCl^-$ and (b) NH_2Cl at pH 8.

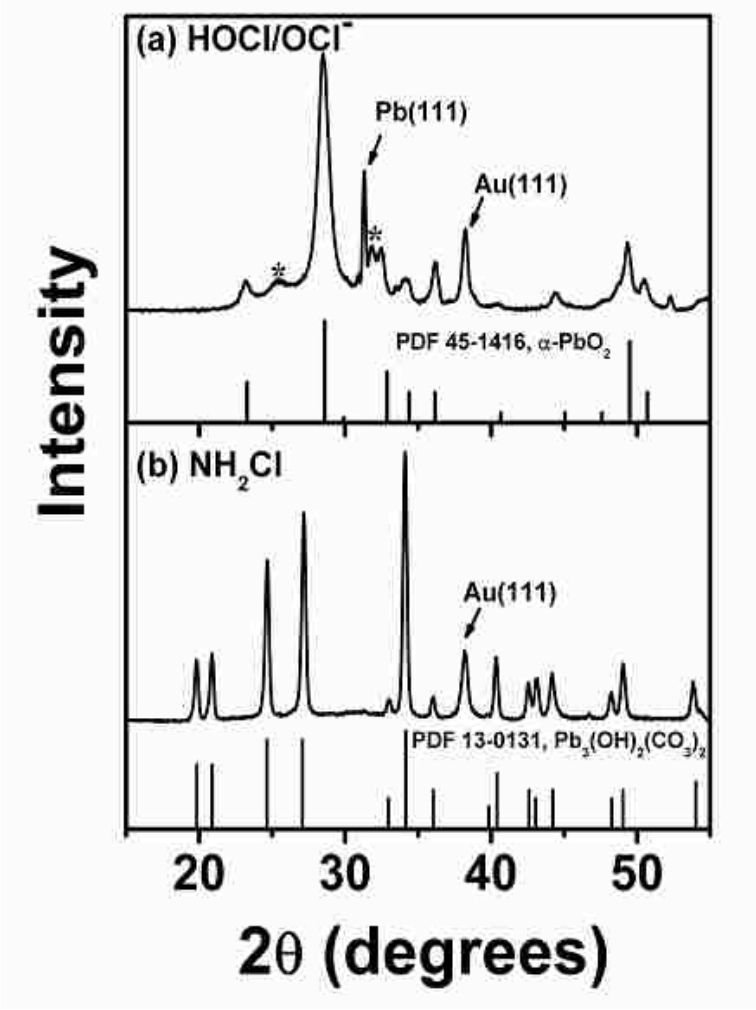

Figure 3: Glancing angle x-ray diffraction patterns of 0.5 μm thick Pb films after being immersed in 1 mM solutions of (a) $HOCl/OCl^-$ and (b) NH_2Cl at pH 8. The standard powder patterns for α-PbO_2 and $Pb_3(OH)_2(CO_3)_2$ are shown in (a) and (b), respectively. The Pb film exposed to $HOCl/OCl^-$ contains primarily α-PbO_2, unreacted Pb, and a small amount of β-PbO_2 (marked with an asterisk). The Pb film exposed to NH_2Cl contains only $Pb_3(OH)_2(CO_3)_2$, with no remaining Pb. The Au(111) peaks in both diffraction patterns are from the Au-coated EQCM electrode. The x-ray radiation is CuKα.

Paper II

Electrochemistry of Free Chlorine and Monochloramine and its Relevance to the Presence of Pb in Drinking Water

*Vishnu V. Rajasekharan, Brandi N. Clark, Sansanee Boonsalee, and Jay A. Switzer**

Department of Chemistry and Graduate Center for Materials Research
Missouri University of Science and Technology, Missouri, U.S.A 65409-1170
Email: jswitzer@mst.edu

Abstract

The commonly used disinfectants in drinking water are free chlorine (in the form of HOCl/OCl^-) and monochloramine (NH_2Cl). While free chlorine reacts with natural organic matter in water to produce chlorinated hydrocarbon byproducts, there is also concern that NH_2Cl may react with Pb to produce soluble Pb(II) products – leading to elevated Pb levels in drinking water. In this study, electrochemical methods are used to compare the thermodynamics and kinetics of the reduction of these two disinfectants. The standard reduction potential for NH_2Cl/Cl^- was estimated to be +1.45 V in acidic media and +0.74 V in alkaline media versus NHE using thermodynamic cycles. The kinetics of electroreduction of the two disinfectants was studied using an Au rotating disk electrode. The exchange current densities estimated from Koutecky–Levich plots were 8.2×10^{-5} A/cm^2 and 4.1×10^{-5} A/cm^2, and by low overpotential experiments were $7.5 \pm 0.3 \times 10^{-5}$ A/cm^2 and $3.7 \pm 0.4 \times 10^{-5}$ A/cm^2 for free chlorine and NH_2Cl, respectively. The rate constant for the electrochemical reduction of free chlorine at equilibrium is approximately twice as large as that for the reduction of NH_2Cl. Equilibrium potential

measurements show that free chlorine will oxidize Pb to PbO_2 above pH 1.7, whereas NH_2Cl will oxidize Pb to PbO_2 only above about pH 9.5, if the total dissolved inorganic carbon (DIC) is 18 ppm. Hence, NH_2Cl is not capable of producing a passivating PbO_2 layer on Pb, and could lead to elevated levels of dissolved Pb in drinking water.

Introduction

Free chlorine (in the form of hypochlorous acid (HOCl) & hypochlorite anion (OCl^-)) and monochloramine (NH_2Cl) have been used as disinfectants in drinking water *(1)*. They both, however, produce disinfection byproducts. Free chlorine reacts with organic compounds present in water to produce chlorinated hydrocarbons such as trihalomethanes, which are suspected to be carcinogens *(2)*. There is also evidence that NH_2Cl reacts with Pb present in lead service lines, solder, and brass to form soluble Pb(II) *(3-6)*. As a consequence, it is important to understand the difference in reactivity of these two disinfectants to ensure the safety of drinking water.

In our earlier work, we showed that NH_2Cl oxidized Pb to soluble Pb(II) species, whereas free chlorine produced a passivating layer of PbO_2 on the Pb *(3)*. Previous theoretical studies *(3,7-10)* showed that both NH_2Cl and free chlorine are capable of oxidizing Pb to PbO_2, based on the standard reduction potential. However, in real systems only free chlorine forms PbO_2, whereas NH_2Cl forms Pb(II) species *(3-6,11,12)*.

The chemical reactivity *(9,13-26)* and the electroactivity *(27-32)* of these disinfectants have been studied by other workers. For example, Valentine and co-workers have studied the mechanistic aspects of the reactions between NH_2Cl and Fe(II) in aqueous solutions *(15-17)*. They have presented evidence that the oxidation of Fe(II) to Fe(III) by monochloramine occurs through the formation of a reactive intermediate

(amidogen radical ($NH_2^{\bullet}$)) *via* two sequential one-electron steps *(15)*. Wrona and Piela studied the electroreduction of chloramines on rotating Pt and Au electrodes *(27)*. They also suggest that the electroreduction of monochloramine occurs *via* the formation of amidogen radical.

In the present work, we use electrochemical measurements to provide a direct comparison of the kinetics and thermodynamics of the electron transfer reactions of free chlorine and NH_2Cl. The thermodynamics of the reduction of the two disinfectants is compared by calculating the standard reduction potentials from thermodynamic cycles, and by performing equilibrium (i.e., open-circuit) potential measurements. The chemical reversibility and redox activity of the two disinfectants is probed in unstirred solution by cyclic voltammetry. The kinetics of reduction of the two disinfectants is studied using a Au rotating disk electrode (RDE). The RDE is used to control mass transport to the electrode, so that the kinetics can be separated from mass transport by using Koutecky-Levich analysis. Finally, the equilibrium potentials of free chlorine and NH_2Cl are plotted on a Pourbaix diagram for the Pb-H_2O-CO_2 system in order to understand the effects of the two disinfectants on the dissolution of Pb.

Experimental Section

All experiments were conducted using deionized 18 MΩ-cm water from a Barnstead NANOpure ultrapure water system. A sodium hypochlorite (NaOCl) solution with 10-13 vol% available chlorine was used as a source for free chlorine. NH_2Cl and free chlorine solutions were prepared fresh for each experiment. Free chlorine and NH_2Cl have characteristic UV absorption bands. The actual concentrations of OCl^- (at pH 9 the predominant species of free chlorine is OCl^- (97 %)) and NH_2Cl were determined

spectrophotometrically at 292 nm (ε = 350 $M^{-1}cm^{-1}$) *(21)* and 243 nm (ε = 461 $M^{-1}cm^{-1}$) *(21)*, respectively. The concentration of $NHCl_2$ was determined at 206 nm (ε = 2100 $M^{-1}cm^{-1}$) *(27)*.

The NH_2Cl solutions were prepared by reacting free chlorine with a five-fold molar excess of aqueous NH_3. The excess NH_3 minimizes the formation of dichloramine ($NHCl_2$) *(33)*. To prepare the NH_2Cl solutions, 5 mL of 100 mM NH_3 was added to a rapidly stirred 20 mL solution of 5 mM NaOCl. The solutions for kinetic studies were buffered at pH 9 with 60 mM $NaHCO_3$. The supporting electrolyte was 100 mM Na_2SO_4. For the equilibrium potential measurements, 60 mM NaH_2PO_4 was used as a buffer for pH 7-8, and 60 mM of $NaHCO_3$ or H_3BO_3 were used as buffers in the pH range of 9 to 12. It is important to note that these buffers can be used to study the electrochemistry of NH_2Cl and free chlorine on inert electrodes such as Au or Pt, but they would complicate studies involving Pb or PbO_2 electrodes because of the formation of insoluble Pb(II) carbonates and phosphates.

A Fisher Scientific Accumet Model 15 digital pH meter equipped with an Accumet combination electrode was used for the pH measurements. An Accumet chloride combination ion selective electrode was used to measure the chloride ion concentration. A Hach ammonia gas sensing combination electrode was used to measure the total excess ammonia present in the NH_2Cl containing solutions. Typically, approximately 4 mM total ammonia was present after the formation of NH_2Cl.

Electrochemical experiments were performed using a Brinkmann PGSTAT 100 potentiostat controlled by GPES software v. 4.9. The experiments were run at room temperature in a cell that was not thermostatted. A polycrystalline Au electrode (Pine

instruments, USA) of geometric area 0.196 cm^2 was used for stationary and rotating disk studies. A MSRX speed controller from Pine instrument company was used to vary the rotation rates. The counter electrode was a Pt wire. A saturated calomel electrode (SCE) was used as the reference electrode in all electrochemical experiments. All potentials, except equilibrium potentials, are reported versus the SCE. The equilibrium potentials are reported versus the normal hydrogen electrode (NHE) by adding 0.242 V to the potential measured versus SCE. The equilibrium potentials were measured on an Au electrode after equilibrating for 1000 s. Equilibrium potentials must be measured with a high impedance voltmeter or electrometer, so that the equilibrium is not shifted by current flow. In our studies the Brinkmann PGSTAT 100 potentiostat (input impedance greater than 100 Gohm) was used for these measurements. The working solutions were deoxygenated by bubbling with argon (99.998 %)(BOC gases).

Results and Discussion

Calculation of the standard reduction potential of NH_2Cl

The standard reduction potential of the NH_2Cl/Cl^- couple in both acidic and alkaline solutions can be estimated using the following parameters: the equilibrium constants for Equation 1 *(20)*, 2, 4 & 5 and the standard reduction potentials for $HOCl/Cl^-$ and OCl^-/Cl^-, (Equations 3 & 6) *(34)*. The relationship between the free energy, equilibrium constant and standard reduction potential ($\Delta G° = -RT \ln K = -nFE°$) was then used to calculate the $\Delta G°$ for the reactions below. By convention, the equilibrium constants are shown without units, although they are based on molar concentrations.

$NH_2Cl + H_2O \leftrightarrows NH_3 + HOCl$ $\quad K = 2.63 \times 10^{-11}$; $\quad \Delta G_1° = 60$ kJ/mol (1)

$NH_3 + H^+ \leftrightarrows NH_4^+$ $\quad K = 1.78 \times 10^{9}$; $\quad \Delta G_2° = -53$ kJ/mol (2)

$HOCl + H^+ + 2e^- \leftrightarrows Cl^- + H_2O$ $E° = +1.482$ V; $\Delta G_3° = -286$ kJ/mol (3)

$HOCl \leftrightarrows OCl^- + H^+$ $K = 2.9 \times 10^{-8}$; $\Delta G_4° = 43$ kJ/mol (4)

$H^+ + OH^- \leftrightarrows H_2O$ $K = 5.56 \times 10^{15}$; $\Delta G_5° = -90$ kJ/mol (5)

$OCl^- + H_2O + 2e^- \leftrightarrows Cl^- + 2OH^-$ $E° = +0.81$ V; $\Delta G_6° = -156$ kJ/mol (6)

The standard reduction potentials of NH_2Cl in acidic and alkaline solutions can be determined by standard thermodynamic cycles. To estimate $\Delta G_a°$ for the reduction reaction of NH_2Cl in acidic media (i.e., pH = 0), the $\Delta G°$s for the elementary reactions shown in Equations 1, 2 & 3 are summed, as shown in Equation 7.

$\Delta G_a° = \Delta G_1° + \Delta G_2° + \Delta G_3° = -279$ kJ/mol (7)

From Equation 7 the standard reduction potential for NH_2Cl can be determined, and is given below in Equation 8

$NH_2Cl + 2H^+ + 2e^- \leftrightarrows Cl^- + NH_4^+$ $E° = +1.45$ V vs. NHE (8)

To estimate $\Delta G_b°$ for the reduction reaction of NH_2Cl in alkaline media (i.e., pH = 14), the $\Delta G°$s for the elementary reactions shown in Equations 1, 4, 5 & 6 are summed, as shown in Equation 9.

$\Delta G_b° = \Delta G_1° + \Delta G_4° + \Delta G_5° + \Delta G_6° = -143$ kJ/mol (9)

From Equation 9 the standard reduction potential for NH_2Cl can be determined, and is given below in Equation 10

$NH_2Cl + H_2O + 2e^- \leftrightarrows Cl^- + OH^- + NH_3$ $E° = +0.74$ V vs. NHE (10)

Equilibrium potentials for NH_2Cl

Equilibrium (i.e., open-circuit) potential measurements for NH_2Cl were performed on a Au electrode in solutions containing equimolar quantities of the redox species in 60 mM buffered solutions. Equilibrium potentials are also referred to in the

literature as oxidation-reduction potentials (ORPs). James *et al.* have previously used ORP measurements to compare the relative impact of various disinfectants on metallic plumbing material solubility and speciation (*35*). Figure 1 shows a plot of the measured (open circles) equilibrium potentials for NH_2Cl as a function of pH. Figure 1 also compares the measured equilibrium potentials to calculated formal potentials. The standard reduction potentials for Equations 8 & 10 are for all of the reactants and products at unit activity. Formal potentials for these reactions at other concentrations and pHs can be calculated from the Nernst equation (Equation 11).

$$E = E^o - RT/nF \ lnQ \qquad (11)$$

where E is the formal potential (V), E^o is the standard reduction potential (V), R is the molar gas constant (8.314 $Jmol^{-1}K^{-1}$), T is the absolute temperature (K), n is the number of electrons transferred, F is Faraday's constant (96,485 C), and Q is the reaction quotient (dimensionless).

The formal reduction potentials (solid lines) calculated from Equation 11 are shown in Figure 1. The formal potentials were calculated from Equation 11 with $[NH_2Cl] = [Cl^-] = 1$ mM, and $[NH_3] + [NH_4^+] = 4$ mM. For the calculated formal potentials, a Nernstian slope of 59 mV/pH is predicted at low pH, and a slope of 29.5 mV/pH is predicted at high pH. The change in slope at pH 9.25 is due to the fact that NH_4^+ (pKa = 9.25) is formed below the pKa, and NH_3 is formed above the pKa. The slope of a linear fit for the values of measured equilibrium potentials is 75 mV/pH below pH 9.4 and 41 mV/pH above pH 9.4.

The measured equilibrium potential is approximately 300 mV more negative than the calculated formal potential at pH 9.25. This suggests that there is either an error in

the calculated standard reduction potentials for Equations 8 and 10 due to an error in the equilibrium constant for Equation 1 *(9,36)*, or that the reduction of NH_2Cl does not proceed by the reactions shown in Equations 8 and 10. One explanation is that there are competing reactions involving reactive amidogen ($NH_2^{\bullet}$) radical intermediates. The radicals could either couple to produce hydrazine or react with bicarbonate in solution. In either case, the measured equilibrium potential would be different from the calculated formal potential. Valentine and co-workers have shown evidence for the formation of the amidogen radical during oxidation of Fe(II) *(15)*. They have also proposed that these radicals can be scavenged by bicarbonate or that radical-radical coupling can occur to produce hydrazine. Piela and Wrona have also suggested that the amidogen radical is produced in the rate determining, one-electron step during the electroreduction of NH_2Cl *(27)*.

Cyclic voltammetry of OCl^- and NH_2Cl

Figures 2a and b show cyclic voltammograms (CVs) of (a) OCl^- and (b) NH_2Cl in Ar-purged solutions containing 60 mM $NaHCO_3$ and 0.1 M Na_2SO_4 at pH 9 for various concentrations of the two disinfectants. The CVs were run in an unstirred solution at a scan rate of 50 mV/s on a Au stationary electrode. In the CVs, OCl^- and NH_2Cl both show single cathodic peaks at approximately 0.32 V and 0.03 V, respectively. There are no significant anodic peaks corresponding to these cathodic peaks, showing that the reactions are electrochemically irreversible reductions. In oxygen-saturated solutions (not shown), both solutions show an additional cathodic peak at -0.25 V due to the reduction of dissolved oxygen. The cathodic peak currents for the

reduction of both OCl^- and NH_2Cl increase linearly as the concentrations of the two disinfectants are increased.

Rotating disk studies of the reduction of OCl^- and NH_2Cl

The standard heterogeneous rate constant (k_o) for the reduction of OCl^- and NH_2Cl can be determined at the equilibrium potential (i.e., zero driving force) using the rotating disk electrode by both Koutecky–Levich analysis, and by using a linear approximation to the Butler-Volmer equation at very low overpotential *(37)*. Figures 3a and b show linear sweep voltammograms of 1.7 mM OCl^- and NH_2Cl, respectively, in an Ar-purged solution containing 60 mM $NaHCO_3$ and 0.1 M Na_2SO_4 at pH 9 at a scan rate of 50 mV/s on a Au rotating disk electrode at various rotation rates. Both disinfectants show mixed kinetic-diffusion regimes at intermediate potentials and mass-transport-limited currents at high overpotentials. Koutecky-Levich analysis was done in the mixed kinetic-diffusion regimes. The Koutecky–Levich equation is shown in Equation 12.

$$1/i = 1/i_k + 1/i_l = 1/i_k + 1/(0.62nFAD^{2/3}\omega^{1/2}\upsilon^{-1/6}C) \quad (12)$$

where i is the measured current (A), i_k is the current in the absence of any mass-transport effects (A), i_l is the limiting current at high overpotential (A), n is the number of electrons transferred, F is Faraday's constant (96,485 C), A is the electrode area (cm^2), D is the diffusion coefficient (cm^2s^{-1}), ω is the angular frequency of rotation (s^{-1}), υ is the kinematic viscosity (cm^2s^{-1}) and C is the concentration (mol/cm^3).

Figure 4 shows Koutecky–Levich plots of 1/i versus $1/\omega^{1/2}$ for (a) OCl and (b) NH_2Cl at a series of overpotentials (η). The overpotentials were approximated by taking the difference between the applied electrode potential and the open circuit potentials of 0.67 V for OCl^- and 0.47 V for NH_2Cl. Straight lines are observed for both disinfectants

with intercepts corresponding to their kinetic currents (i_k) for a wide range of overpotentials (0.375 to 0.575 V). The kinetic currents (i_k) can be converted to rate constants (k_f) using equation 13.

$$i_k = nFAk_fC \quad (13)$$

where n is the number of electrons transferred, F is Faraday's constant (C), A is the electrode area (cm^2), k_f is the forward rate constant (cm/s), and C is the concentration (mol/cm^3). We assumed n = 2 for these calculations.

Figure 5 shows a plot of ln $k_f(E)$ versus overpotential (η). This plot should have a slope of $-\alpha F/RT$ and an intercept equal to ln (k^o) *(37)*. The α value determined from the slope for OCl^- was 0.3, and for NH_2Cl was 0.2. The k^o value obtained for OCl^- was 2.5×10^{-4} cm/s and, for NH_2Cl was 1.2×10^{-4} cm/s. The exchange current densities (j_o) determined from these k^o values using Equation 13 and normalizing for the electrode area were 8.2×10^{-5} A/cm^2 and 4.1×10^{-5} A/cm^2 for OCl^- and NH_2Cl, respectively. These values show that at equilibrium, the rate constant for the reduction of OCl^- is approximately twice that of NH_2Cl.

The standard heterogeneous rate constant k_o can also be estimated from linear sweep voltammograms at low overpotential, where mass-transport effects are minimal. For small values of overpotential, η, the Butler–Volmer equation is approximated by Equation 14 *(37,38)*.

$$j = -j_oF\eta/(RT) \quad (14)$$

where j is the measured current density (A/cm^2), j_o is the exchange current density (A/cm^2), F is Faraday's constant (C), η is the applied overpotential (V), R is the molar gas constant ($Jmol^{-1}K^{-1}$), and T is the absolute temperature ($F/RT = 38.92$ V^{-1} at 298 K).

Figure 6 shows plots of j versus η for 1.7 mM OCl^- and NH_2Cl in an Ar-purged solution containing 60 mM $NaHCO_3$ and 0.1 M Na_2SO_4 at pH 9. The voltammograms were run at a scan rate of 1 mV/s on a Au electrode at 900 rpm. The slopes of the j versus η plots for the disinfectants were not dependent on the rotation rate. The slopes of five different rotation rates (700 rpm, 900, 1100, 1300, and 1500) were obtained to estimate the error involved in the measurements. The exchange current densities, j_o, determined from these slopes are $7.5 \pm 0.3 \times 10^{-5}$ A/cm^2 for OCl^- and $3.7 \pm 0.4 \times 10^{-5}$ A/cm^2 for NH_2Cl. The k^o values determined from the j_o values are $2.3 \pm 0.1 \times 10^{-4}$ and $1.1 \pm 0.1 \times 10^{-4}$ cm/s for OCl^- and NH_2Cl, respectively.

The exchange current densities and standard heterogeneous rate constant for OCl^- and NH_2Cl are summarized in Table 1 for measurement by both Koutecky–Levich analysis and by the linear approximation of the Butler-Volmer equation at low overpotential. Both methods show that at equilibrium (zero driving force), the rate constant for the reduction of OCl^- is approximately twice that of NH_2Cl.

Measured equilibrium potential as a diagnostic tool to determine the stability of Pb

Figure 7 shows the Pourbaix diagram for the Pb-H_2O-CO_2 system along with the measured formal potentials of NH_2Cl and free chlorine. This diagram is constructed to determine the stability of Pb in the presence of these disinfectants. Figure 7 is similar to the one constructed by Schock and co-workers *(39-41)*. The concentration of the dissolved Pb(II) species in Figure 7 is fixed at the action level of Pb in drinking water (7.2×10^{-8} M) (15 ppb). The concentration of total dissolved inorganic carbon (DIC) is chosen as 1.5 mM (18 ppm), which is the value previously used by Schock *et al. (40)*. The Gibbs free energies of formation of the different Pb species at 298 K and 1 atm are

used to calculate the equilibrium constants and standard reduction potentials for the chemical and electrochemical reactions of different Pb species *(41)*. The lead carbonate species are included in Figure 7, due to the importance of carbonate compounds of the Pb(II) species *(41-44)*. In our previous study we observed a lead carbonate phase (hydrocerrusite ($Pb_3(CO_3)_2(OH)_2$)), when a Pb film was exposed to a solution containing NH_2Cl *(3)*.

In Figure 7, the measured equilibrium potentials for NH_2Cl/Cl^- are more negative than those of the free chlorine species for pH values that are relevant to drinking water. This is a direct indication that NH_2Cl is a thermodynamically weaker oxidizing agent than free chlorine. Figure 7 shows that free chlorine is thermodynamically capable of oxidizing Pb to PbO_2 above pH 1.7, whereas NH_2Cl is thermodynamically capable of oxidizing Pb to PbO_2 only above about pH 9.5 at the DIC level of 18 ppm. Even above pH 9.5, the driving force for the production of PbO_2 by NH_2Cl is small. It is also dependent on the concentration of Pb(II) used to calculate the Pourbaix diagram, and on the concentration of dissolved inorganic carbon. The relationship of the measured equilibrium potentials with the $Pb(II)/PbO_2$ boundary in the Pourbaix diagram is consistent with our previous *in-situ* Pb dissolution studies at pH 8, in which NH_2Cl oxidizes Pb to Pb(II) species such as $Pb_3(CO_3)_2(OH)_2$, whereas free chlorine oxidizes Pb to insoluble, tetravalent PbO_2 *(3)*. The measurement of equilibrium potentials in drinking water may prove to be a useful diagnostic tool to determine the stability of Pb in the presence of these disinfectants.

Acknowledgement: This work was supported by NSF grants CHE-0437346, and DMR-0504715.

References

(1) White, G. C. *Handbook of Chlorination and Alternative Disinfectants*; 2nd ed.; Van Nostrand Reinhold Company: New York, 1986.

(2) U. S. Environmental Protection Agency. National interim primary drinking water regulations; control of trihalomethanes in drinking water. *Fed. Regist.* **1979,** 44, 68624-68707.

(3) Switzer, J. A.; Rajasekharan, V. V.; Boonsalee, S.; Kulp, E. A.; Bohannan, E. W. Evidence that Monochloramine Disinfectant Could Lead to Elevated Pb Levels in Drinking Water. *Environ. Sci. Technol.* **2006**, *40*, 3384-3387.

(4) Edwards, M.; Dudi, A. Role of chlorine and chloramine in corrosion of lead-bearing plumbing materials. *J. Am. Water Works Assoc.* **2004**, *96*, 69-81.

(5) Renner, R. Plumbing the depths of D.C.'s drinking water crisis. *Environ. Sci. Technol.* **2004**, *38*, 224A-227A.

(6) Renner, R. Chloramines again linked to lead in drinking water. *Environ. Sci. Technol.* **2005**, *39*, 314A.

(7) Jolly, W. L. The thermodynamic properties of chloramine, dichloramine, and nitrogen trichloride. *J. Phys. Chem.* **1956**, *60*, 507-508.

(8) Soulard, M.; Bloc, F.; Hatterer, A. Diagrams of existence of chloroamines and bromoamines in aqueous solution. *J. Chem. Soc., Dalton Trans.* **1981**, 2300-2310.

(9) Gray, E. T., Jr.; Margerum, D. W.; Huffman, R. P. Chloramine equilibriums and the kinetics of disproportionation in aqueous solution. *ACS Symp. Ser.* **1978**, *82*, 264-277.

(10) Wrona, P. K. Electrode processes of chloramines in aqueous solutions. *Journal of Electroanalytical Chemistry* **1998**, *453*, 197-204.

(11) Renner, R. More chloramine complications. *Environ. Sci. Technol.* **2004**, *38*, 342A-343A.

(12) Renner, R. Chloramine's effect on lead in drinking water. *Environ. Sci. Technol.* **2006**, *40*, 3129-3130.

(13) Yiin, B. S.; Margerum, D. W. Non-metal redox kinetics: reactions of trichloramine with ammonia and with dichloramine. *Inorg. Chem.* **1990**, *29*, 2135-2141.

(14) Yiin, B. S.; Walker, D. M.; Margerum, D. W. Nonmetal redox kinetics: general-acid-assisted reactions of chloramine with sulfite and hydrogen sulfite. *Inorg. Chem.* **1987**, *26*, 3435-3441.

(15) Vikesland, P. J.; Valentine, R. L. Reaction Pathways Involved in the Reduction of Monochloramine by Ferrous Iron. *Environ. Sci. Technol.* **2000**, *34*, 83-90.

(16) Vikesland, P. J.; Valentine, R. L. Iron Oxide Surface-Catalyzed Oxidation of Ferrous Iron by Monochloramine: Implications of Oxide Type and Carbonate on Reactivity. *Environ. Sci. Technol.* **2002**, *36*, 512-519.

(17) Vikesland, P. J.; Valentine, R. L. Modeling the kinetics of ferrous iron oxidation by monochloramine. *Environ. Sci. Technol.* **2002**, *36*, 662-668.

(18) Snyder, M. P.; Margerum, D. W. Kinetics of chlorine transfer from chloramine to amines, amino acids, and peptides. *Inorg. Chem.* **1982**, *21*, 2545-2550.

(19) Margerum, D. W.; Gray, E. T., Jr.; Huffman, R. P. Chlorination and the formation of N-chloro compounds in water treatment. *ACS Symp. Ser.* **1978**, *82*, 278-291.

(20) Margerum, D. W.; Schurter, L. M.; Hobson, J.; Moore, E. E. Water chlorination chemistry: nonmetal redox kinetics of chloramine and nitrite ion. *Environ. Sci. Technol.* **1994**, *28*, 331-337.

(21) Kumar, K.; Day, R. A.; Margerum, D. W. Atom-transfer redox kinetics: general-acid-assisted oxidation of iodide by chloramines and hypochlorite. *Inorg. Chem.* **1986**, *25*, 4344-4350.

(22) Kumar, K.; Margerum, D. W. Kinetics and mechanism of general-acid-assisted oxidation of bromide by hypochlorite and hypochlorous acid. *Inorg. Chem.* **1987**, *26*, 2706-2711.

(23) Gerritsen, C. M.; Margerum, D. W. Non-metal redox kinetics: hypochlorite and hypochlorous acid reactions with cyanide. *Inorg. Chem.* **1990**, *29*, 2757-2762.

(24) Fogelman, K. D.; Walker, D. M.; Margerum, D. W. Nonmetal redox kinetics: hypochlorite and hypochlorous acid reactions with sulfite. *Inorg. Chem.* **1989**, *28*, 986-993.

(25) Dodd, M. C.; Vu, N. D.; Ammann, A.; Le, V. C.; Kissner, R.; Pham, H. V.; Cao, T. H.; Berg, M.; von Gunten, U. Kinetics and Mechanistic Aspects of As(III) Oxidation by Aqueous Chlorine, Chloramines, and Ozone: Relevance to Drinking Water Treatment. *Environ. Sci. Technol.* **2006**, *40*, 3285-3292.

(26) Conocchioli, T. J.; Hamilton, E. J., Jr.; Sutin, N. Formation of iron(IV) in the oxidation of iron(II). *J. Am. Chem. Soc.* **1965**, *87*, 926-927.

(27) Piela, B.; Wrona, P. K. Electrochemical Behavior of Chloramines on the Rotating Platinum and Gold Electrodes. *J. Electrochem. Soc.* **2003**, *150*, E255-E265.

(28) Shin-ya Kishioka, T. K., Akifumi Yamada,. Electrochemical Determination of a Free Chlorine Residual Using Cathodic Potential-Step Chronocoulometry. *Electroanalysis* **2005**, *17*, 724-726.

(29) Marks, H. C.; Bannister, G. L.; Glass, J. R.; Herrigel, E. Amperometric methods in the control of water chlorination. *Anal. Chem.* **1947**, *19*, 200-204.

(30) Jenkins, E. N. Reactions of hypochlorous acid and sodium hypochlorite at the dropping-mercury electrode. *J. Chem. Soc.* **1951**, 2627-2630.

(31) Heller, K.; Jenkins, E. N. Behavior of hypochlorite and of N-chloroamines at the dropping-mercury electrode. *Nature (London, United Kingdom)* **1946**, *158*, 706.

(32) Evans, O. M. Voltammetric determination of the decomposition rates of combined chlorine in aqueous solution. *Anal. Chem.* **1982**, *54*, 1579-1582.

(33) Brodtmann, N. V., Jr.; Russo, P. J. The use of chloramine for reduction of trihalomethanes and disinfection of drinking water. *J. Am. Water Works Assoc.* **1979**, *71*, 40-42.

(34) Lide, D. R., Ed. *CRC Handbook of Chemistry and Physics*; 86th ed.; Taylor & Francis Group: New York, 2005-2006.

(35) James, C. N.; Copeland, R. C.; Lytle, D. A. Relationships between oxidation-reduction potential, oxidant, and pH in drinking water. *Proc. AWWA Water Quality Technology Conference*, San Antonio, Texas, November 14-18, 2004; pp 1-13.

(36) Anbar, M.; Yagil, G. The hydrolysis of chloramine in alkaline solution. *J. Am. Chem. Soc.* **1962**, *84*, 1790-1796.

(37) Bard, A. J.; Faulkner, L. R. *Electrochemical Methods: Fundamentals and Applications*; 2nd ed.; John Wiley & Sons: New York, 2001.

(38) Switzer, J. A.; Kothari, H. M.; Bohannan, E. W. Thermodynamic to Kinetic Transition in Epitaxial Electrodeposition. *J. Phys. Chem. B* **2002**, *106*, 4027-4031.

(39) Lytle, D. A.; Schock, M. R. The formation of Pb(IV) oxides in chlorinated water. *J. Am. Water Works Assoc.* **2005**, *97*, 102-114.

(40) Schock, M. R.; Harmon, S. M.; Swertfeger, J.; Lohmann, R. Tetravalent lead: a hitherto unrecognized control of tap water lead contamination. *Proceedings - Water Quality Technology Conference* **2001**, 2270-2291.

(41) Schock, M. R.; Wagner, I.; Oliphant, R. J. In *Internal Corrosion of Water Distribution Systems*; 2 ed.; AWWA, Ed.; AWWA: Denver, 1996; pp 131-230.

(42) Schock, M. R. Response of lead solubility to dissolved carbonate in drinking water. *J. Am. Water Works Assoc.* **1980**, *72*, 695-704.

(43) Schock, M. R. Understanding corrosion control strategies for lead. *J. Am. Water Works Assoc.* **1989**, *81*, 88-100.

(44) Schock, M. R.; Gardels, M. C. Plumbosolvency reduction by high pH and low carbonate-solubility relationships. *J. Am. Water Works Assoc.* **1983**, *75*, 87-91.

Table I: Comparison of the kinetic parameters determined by the Koutecky-Levich and low overpotential methods for the electrochemical reduction of NH_2Cl and OCl^-.

	Method				
	Koutecky–Levich plot			**Low overpotential plot**	
	j_o (A/cm^2)	**k^o (cm/s)**	**α**	**j_o (A/cm^2)**	**k^o (cm/s)**
NH_2Cl	**4.1×10^{-5}**	**1.2×10^{-4}**	**0.2**	**$3.7 \pm 0.4 \times 10^{-5}$**	**$1.1 \pm 0.1 \times 10^{-4}$**
OCl^-	**8.2×10^{-5}**	**2.5×10^{-4}**	**0.3**	**$7.5 \pm 0.3 \times 10^{-5}$**	**$2.3 \pm 0.1 \times 10^{-4}$**

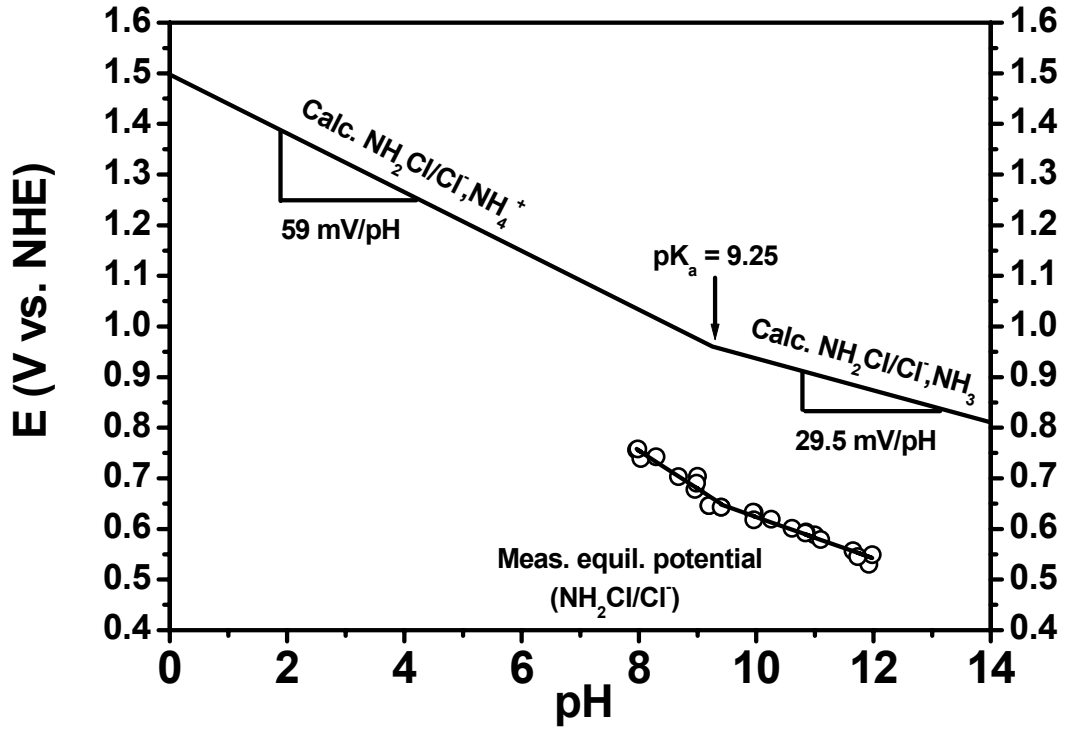

Figure 1: Measured equilibrium potentials (shown as open circles) for the NH_2Cl/Cl^- couple as a function of pH. A linear fit to the measured equilibrium potentials gives two linear regions. Below pH 9.4 the slope is 75 mV/pH, and above pH 9.4 the slope is 41 mV/pH. Calculated formal potentials from the Nernst equation are also shown as solid lines, which change slope at a pH of 9.25, corresponding to the pKa of NH_4^+.

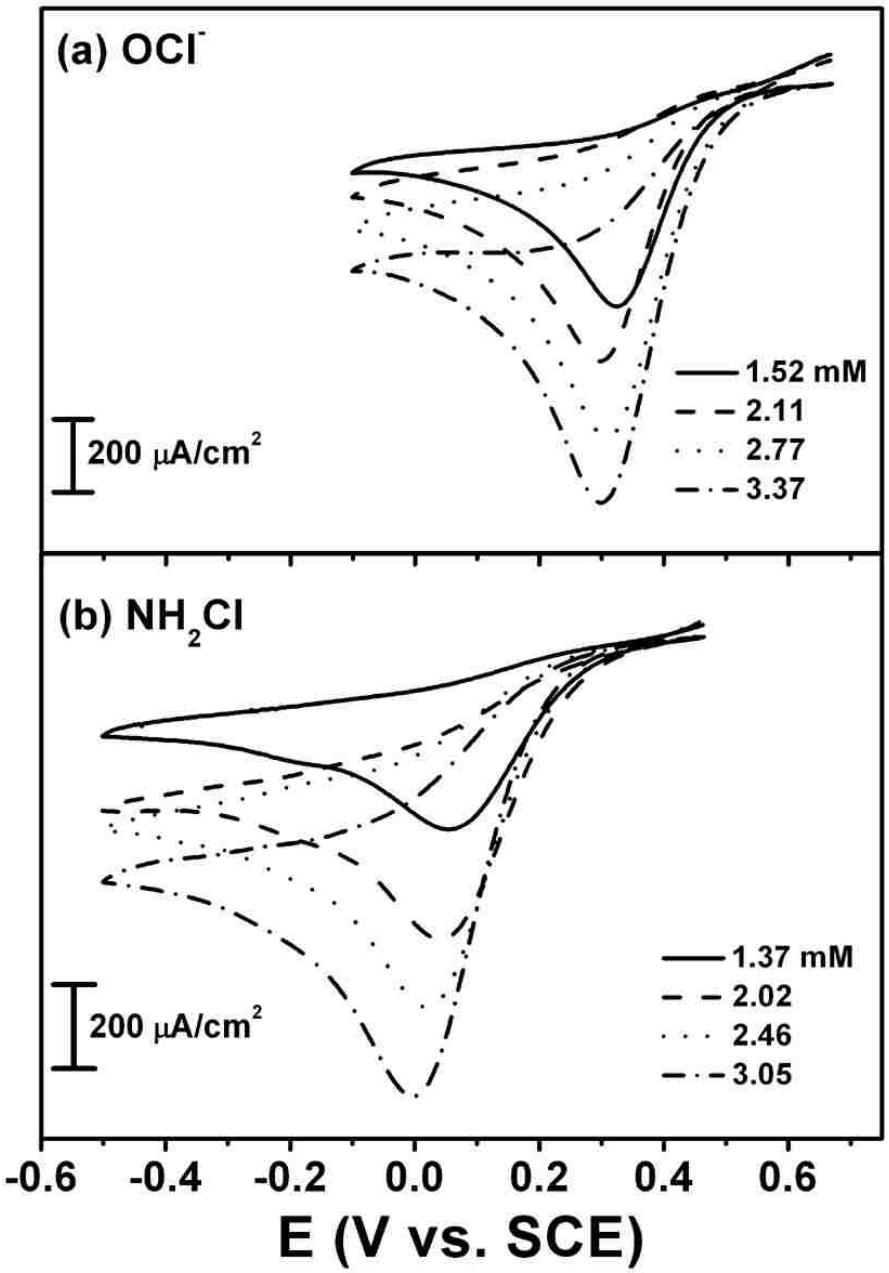

Figure 2: Cyclic voltammograms for the reduction (a) OCl^- and (b) NH_2Cl on a stationary Au electrode at a scan rate of 50 mV/s. The CVs were run in unstirred solutions of OCl^- and NH_2Cl of various concentrations. The pH 9 solutions were Ar purged, and contained 0.1 M Na_2SO_4 and 60 mM $NaHCO_3$.

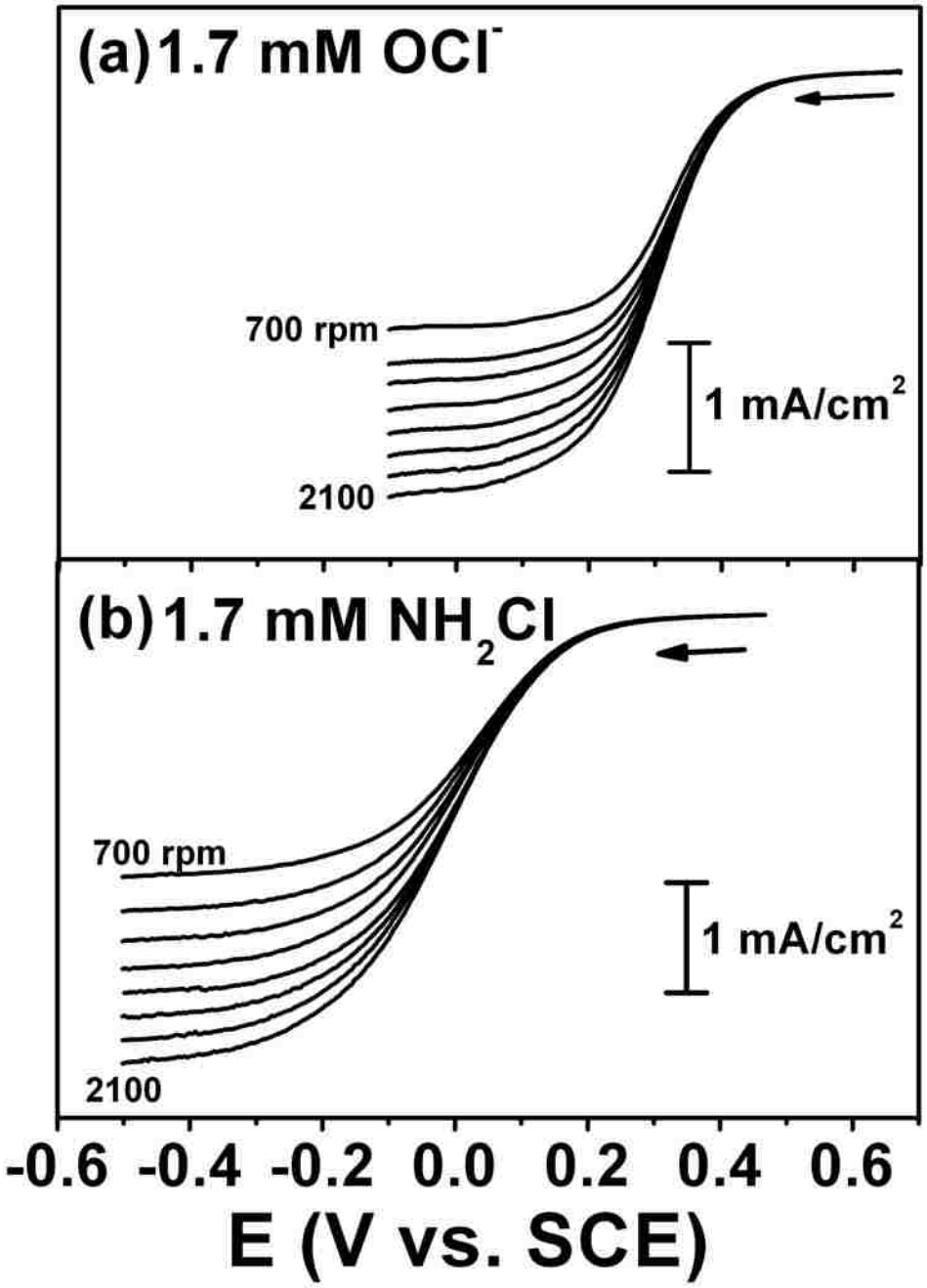

Figure 3: Linear sweep voltammograms of 1.7 mM (a) OCl^- (b) NH_2Cl on a Au rotating disk electrode at rotation rates from 700 to 2100 rpm. The voltammograms were run at a sweep rate of 50 mV/s in Ar-purged solutions containing 0.1 M Na_2SO_4, 60 mM $NaHCO_3$ at pH 9.

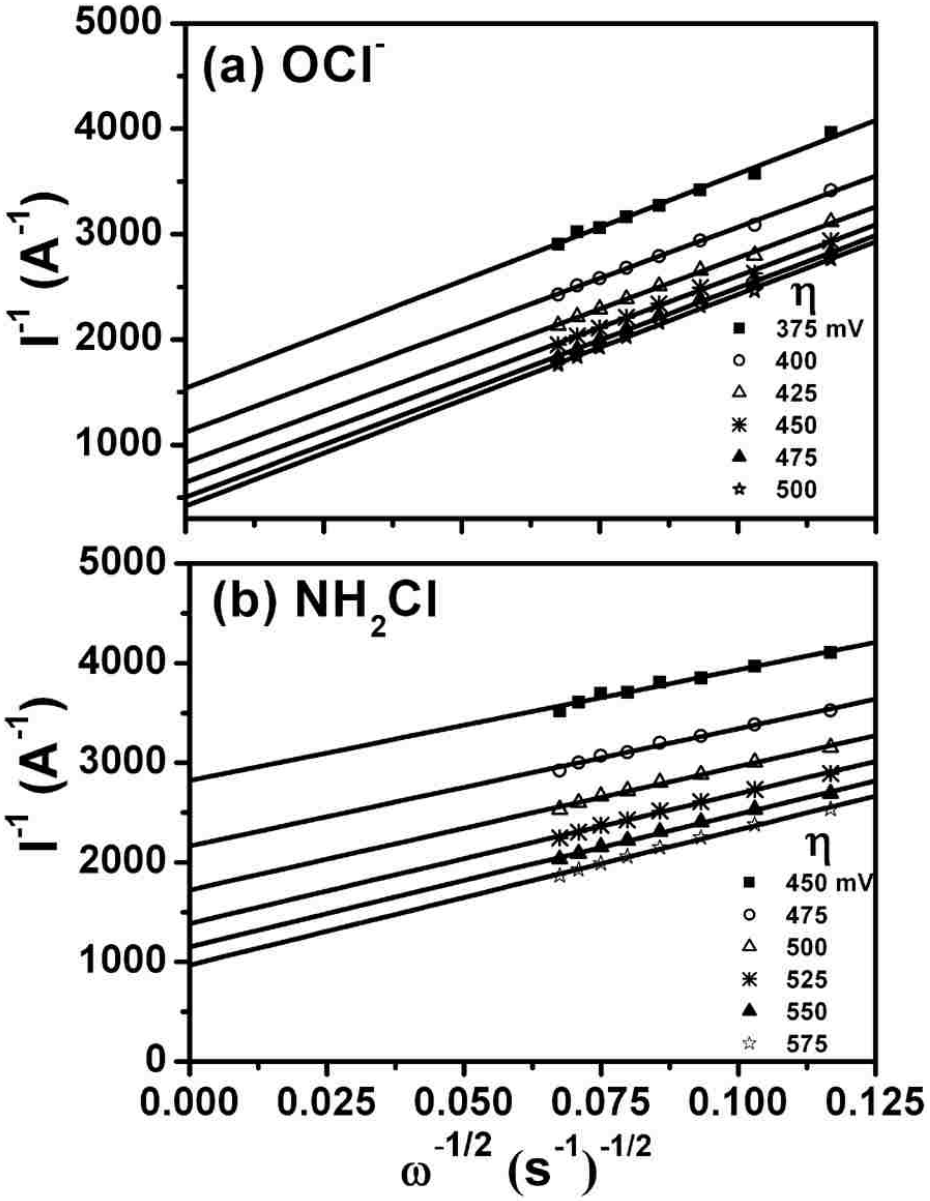

Figure 4: Koutecky–Levich plots for 1.7 mM (a) OCl^- (b) NH_2Cl at a series of different overpotentials (η). Open circuit values of 0.67 V for OCl^- and 0.47 V for NH_2Cl were used to approximate the overpotentials for determining the kinetic currents (i_k).

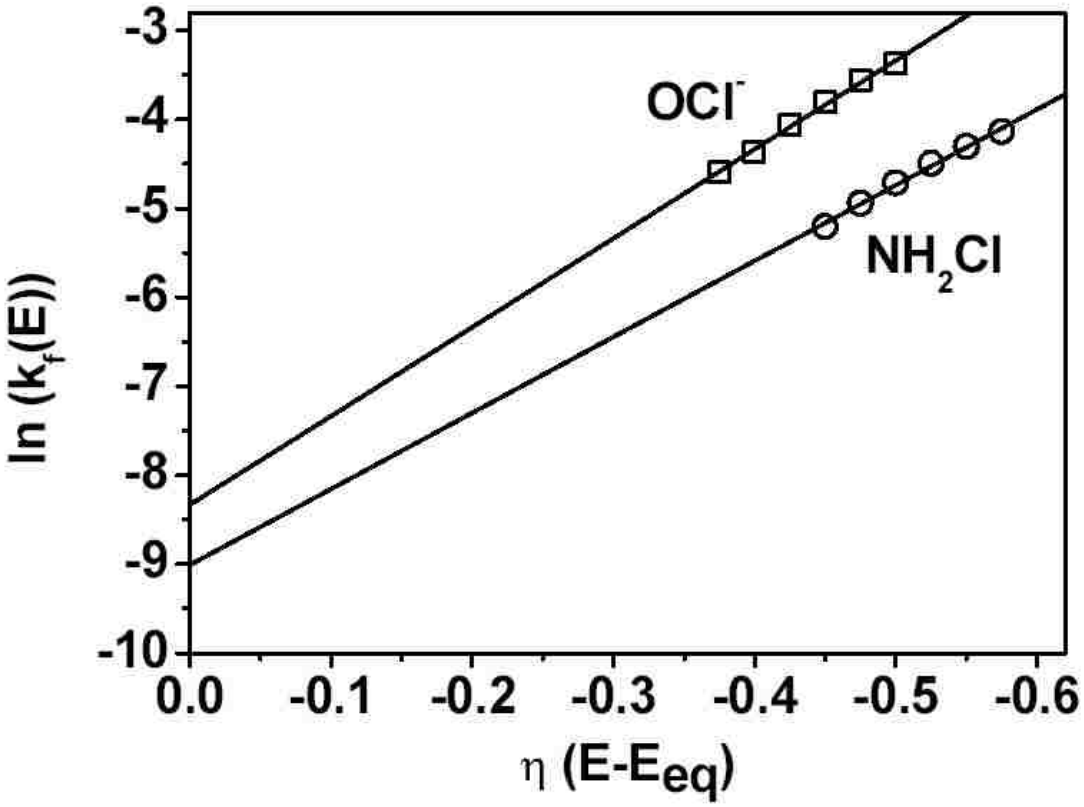

Figure 5: Plots of ln $k_f(E)$ versus overpotential (η) for the data obtained from the Koutecky–Levich plots shown in Figure 4. The intercept of the linear fits is ln (k°), and the slope is proportional to the transfer coefficient (α).

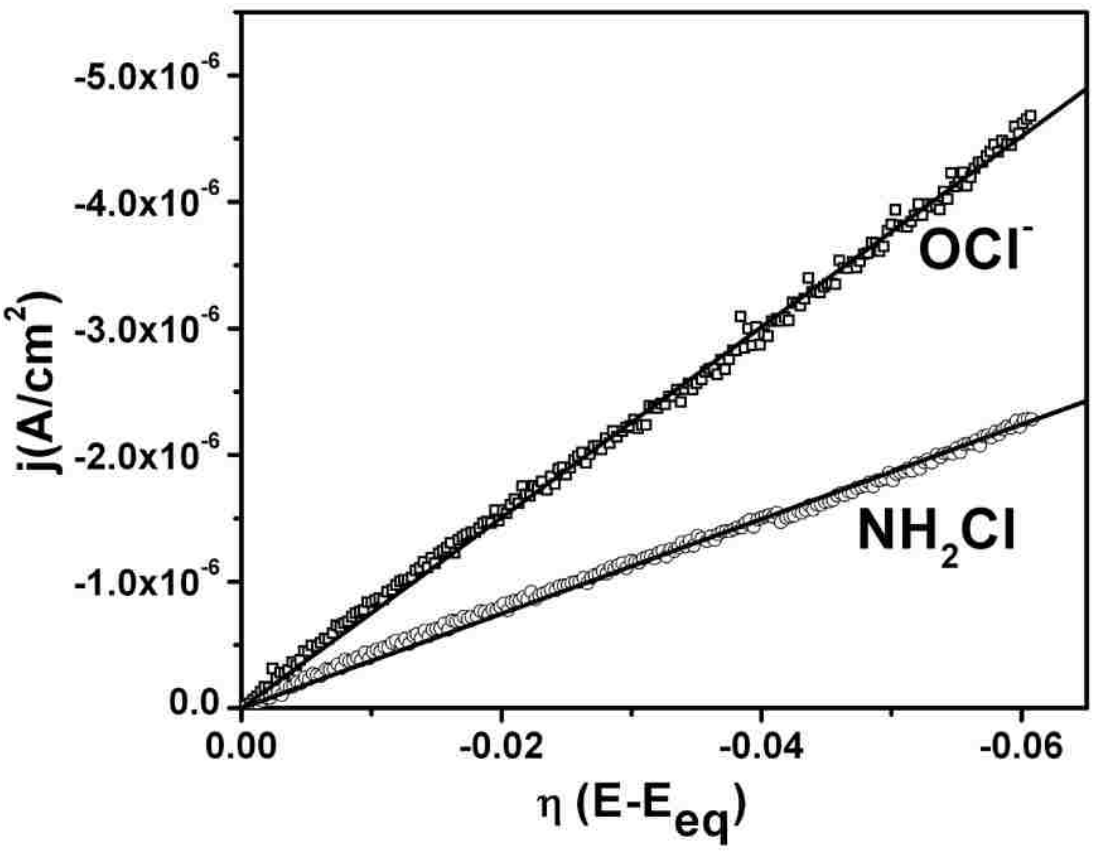

Figure 6: Plots of current density (j) versus overpotential (η) in the small overpotential range (0 to 60 mV) for OCl^- and NH_2Cl at a rotation rate of 900 rpm in an Ar-purged solution containing 0.1 M Na_2SO_4, 60 mM $NaHCO_3$ at pH 9. The scan rate was 1 mV/s.

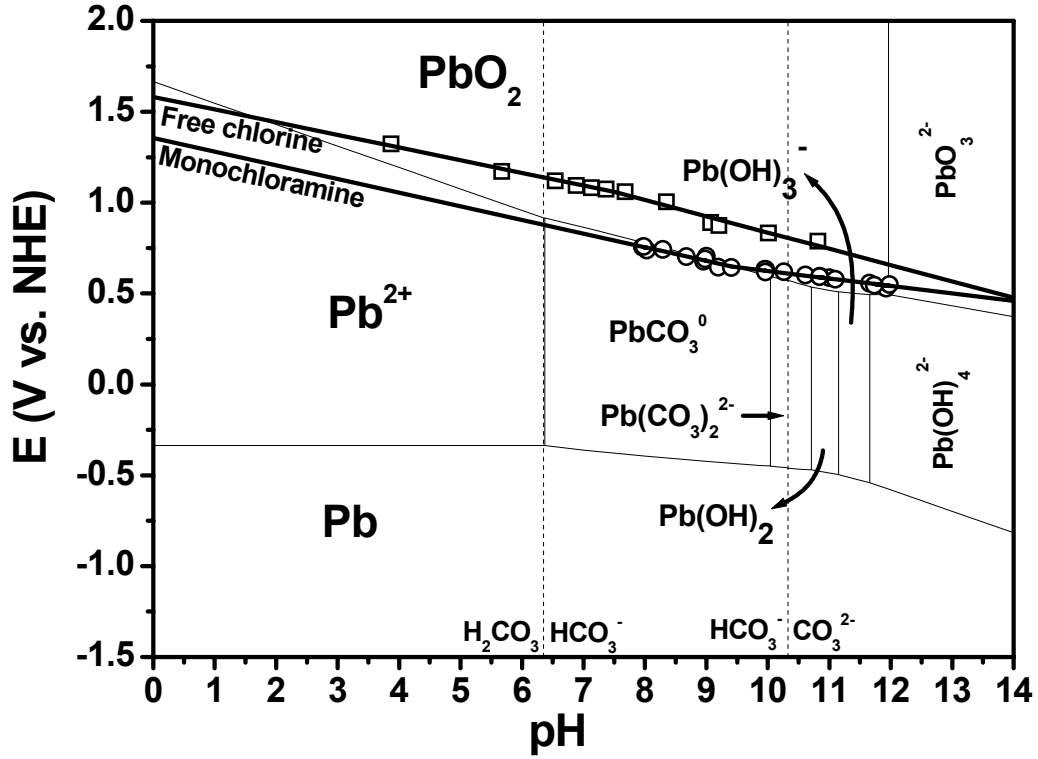

Figure 7: Pourbaix diagram for Pb-H_2O-CO_2 system with the concentration of dissolved Pb species equal to 7.25×10^{-8} M (15 ppb) and the concentration of dissolved inorganic carbon equal to 1.5×10^{-3} M (18 ppm) at 25 °C. Measured equilibrium potentials are shown as open squares for free chlorine, and as open circles for NH_2Cl. A linear fit to the measured equilibrium potentials for free chlorine gives two linear regions. Below pH 7.5 (corresponding to the pKa = 7.5 of HOCl) the slope is 70 mV/pH, and above pH 7.5 the slope is 90 mV/pH.

PAPER III

Electrochemical quartz crystal microbalance study of PbO_2 dissolution in monochloramine

Sansanee Boonsalee, Eric W. Bohannan, Brandi N. Clark, and Jay A. Switzer[*]

Department of Chemistry and Graduate Center for Materials Research
Missouri University of Science and Tehnology, Missouri, U.S.A 65409-1170
Email: jswitzer@mst.edu

Abstract

Lead dioxide (PbO_2) is known to be a stable and insoluble oxide of lead. In water utility systems, PbO_2 is often found in lead service lines if the water has a high oxidation-reduction potential (ORP). The PbO_2 is believed to passivate the lead pipes and help control the plumbosolvency problem. This paper utilizes the electrochemical quartz crystal microbalance to compare the dissolution of electrodeposited PbO_2 films in two disinfectants: free chlorine (in the form of $HOCl/OCl^-$) and monochloramine (NH_2Cl). The PbO_2 film has a mass gain of 0.50 μg when immersed in the stronger oxidant, $HOCl/OCl^-$ at concentrations of of 1 mM. Surprisingly, although NH_2Cl is also an oxidizing agent, it reduces the PbO_2 films to soluble Pb^{2+}. The solubility of PbO_2 in NH_2Cl decreases as the pH is increased. The 55 μg as-deposited PbO_2 film has a mass loss of 17, 2.5, 0.12, and 0.21 μg when immersed in 1 mM NH_2Cl solution for 22 hours at pH 7, 8, 9, and 10, respectively. However, if 0.05 mM orthophosphate is added to NH_2Cl solution at pH 7, then the PbO_2 film is passivated with $Pb_5(PO_4)_3(OH)$ and has a mass

increase of 3.5 μg. The PbO_2 dissolution rate in NH_2Cl solution increases as a function of the NH_2Cl concentration. The PbO_2 dissolution rate is $(3.2\pm1.7)x10^{-3}$, $(3.4\pm1.8)x10^{-3}$, $(9.1\pm9.3)x10^{-3}$, $(9.0\pm7.1)x10^{-3}$, $(16\pm7.2)x10^{-3}$, and $(25\pm6.9)x10^{-3}$ μg/min in solutions containing 0, 3, 10, 20, 35, and 50 ppm NH_2Cl, respectively. Experiments with actual Pb service lines also confirm that free chlorine oxidizes Pb(II) compounds to PbO_2, but NH_2Cl reduces it back to Pb(II) species. Hence, a PbO_2 layer is not stable in NH_2Cl, but dissolves as soluble Pb^{2+}. These results suggest that the use of NH_2Cl disinfectant could lead to elevated Pb levels in drinking water by reducing PbO_2 to soluble Pb(II), and that orthophosphate addition could help mitigate the Pb dissolution.

Introduction

Controlling lead dissolution from lead service lines, brass fixtures, and solders is a goal for all water utility systems. In 1991, the U.S. Environmental Protection Agency's (EPA) Lead and Copper Rule established an action limit of 15 ppb for Pb in drinking water (1-3). Lead solubility models have been constructed for aqueous Pb complexes and solid Pb species dependent on pH, dissolved inorganic carbon (DIC), and orthophosphate concentration (4-6). These models predict that soluble Pb^{2+} reacts with carbonate and phosphate to form solid Pb(II) compounds such as $PbCO_3$ (cerussite), $Pb_3(CO_3)_2(OH)_2$ (hydrocerussite), and $Pb_5(PO_4)_3OH$, which serve as passivation layers and thus control the Pb solubility.

Recently, elevated Pb levels were observed in many water districts including Washington, D.C. and Greenville, NC (7-9). One hypothesis is that changing the disinfection program from free chlorine to monochloramine could cause lead leaching (8, 10-12). In our previous work, we showed by utilizing electrochemical quartz crystal

microbalance (EQCM) (10) and equilibrium potential measurements (11) that free chlorine (in the form of HOCl/OCl^-) oxidizes Pb to insoluble PbO_2 above pH 1.7. However, monochloramine (NH_2Cl) oxidizes Pb to more soluble Pb(II) species such as $Pb_3(CO_3)_2(OH)_2$. Based on the standard reduction potential, NH_2Cl is thermodynamically capable of oxidizing Pb to PbO_2; but experimental results show that if the dissolved inorganic carbon, DIC, is 18 ppm, NH_2Cl can only oxidize Pb to PbO_2 above pH 9.5. Schock et al. have also suggested that insoluble PbO_2 layers are formed in chlorinated water if the oxidation-reduction potential (ORP) is maintained at high enough levels (13-15). These PbO_2 layers are insoluble and stable, which may cause them to serve as passivation layers for Pb-bearing materials. If a weaker oxidant such as NH_2Cl is used, then PbO_2 can be reduced to soluble Pb(II) species, which can cause the Pb levels to increase.

In this study, the EQCM is used to compare the rate of dissolution of PbO_2 films in solutions of different NH_2Cl concentrations. It is also used to study the effects of NH_2Cl, HOCl/OCl^-, and orthophosphate additives on the dissolution of electrodeposited PbO_2 films. The methodology is similar to our previous work (10). However, in this study we are using the EQCM to follow the dissolution of PbO_2 films rather than Pb films in the disinfection solutions. The EQCM is an extremely sensitive device capable of measuring nanogram mass changes in the solution by monitoring the changes in resonant frequency of the quartz oscillator (16). The EQCM has been used by our group and by others to study the corrosion of Pb in real time (10, 17-18). We characterize the PbO_2 films by scanning electron microscopy (SEM) and glancing-angle X-ray diffraction

(XRD). Additionally, we report on the effect of free chlorine and NH_2Cl treatment on actual Pb service lines by using glancing-angle XRD and optical microscopy.

Experimental Section

Disinfectant Solutions

All experiments were conducted using HPLC-grade water from Aldrich. A sodium hypochlorite (NaOCl) solution with 10-13% available chlorine was used as a source for $HOCl/OCl^-$. Fresh NH_2Cl and $HOCl/OCl^-$ solutions were prepared for each experiment. The actual concentrations of HOCl, OCl^-, and NH_2Cl were determined spectrophotometrically at 235 mM ($\varepsilon = 100\ M^{-1}cm^{-1}$), 292 nm ($\varepsilon = 350\ M^{-1}cm^{-1}$) and 243 nm ($\varepsilon = 461\ M^{-1}cm^{-1}$), respectively, using molar absorptivities from the literature (19). The spectrophotometric measurements were made with a CARY 5 UV-Vis-NIR spectrophotometer.

The NH_2Cl solutions were prepared by reacting free chlorine with a five-fold molar excess of aqueous NH_3. The excess NH_3 minimizes the formation of dichloramine ($NHCl_2$) (19, 20). To prepare the NH_2Cl solutions, 5 mL of 100 mM NH_3 was added to a rapidly stirred 5 mL of 20 mM NaOCl. For the phosphate studies, 100 μL of 0.1 M NaH_2PO_4 was added to the NH_2Cl solutions. Then, 10 mM H_2SO_4 was used to obtain the desired pH. The solution was diluted to a total volume of 100 mL. The final concentrations in the solution were approximately 1 mM NH_2Cl, 4 mM NH_4^+, 1 mM Cl^-, and 0.052 mM PO_4^{3-}. The concentrations of HOCl and OCl^- in free chlorine solutions at pH 7 were approximately 1 mM and 0.7 mM, respectively. These high concentrations of disinfectants were used so that the concentration of the disinfectants remained approximately constant during the dissolution studies, and so that the data acquisition

could be achieved in a reasonable time to prevent drifting of the EQCM instrument. These disinfectant concentrations were used consistently throughout the paper, except for in the study of the PbO_2 dissolution rate as a function of the concentration of NH_2Cl, in which concentrations of 0, 3, 10, 20, 35, and 50 ppm were used.

PbO_2 Electrodeposition and Dissolution

Films of PbO_2 were electrodeposited with an EG&G model 273A potentiostat/galvanostat from a solution of 0.1 M $Pb(NO_3)_2$ in 5 M NaOH at room temperature (21). The polycrystalline PbO_2 films were electrodeposited at a constant current density of 1 mA/cm^2 onto Au-coated, commercially available 9 MHz AT-cut quartz crystals (Seiko EG&G model QA-AM9-Au) for the EQCM experiments. The PbO_2 films were used immediately after deposition for the EQCM studies. XRD analysis showed that the films were orthorhombic α-PbO_2 with a space group *Pbcn* (a = 0.4971, b = 0.5956, and c = 0.5438). There was no evidence of PbO in the XRD pattern. The EQCM electrodes were installed in a Teflon holder so that only one electrode face with an area of 0.2 cm^2 was exposed to the solution. The total mass of PbO_2 deposited was 55 μg, and its thickness was approximately 0.3 μm. The electrodeposited PbO_2 films were then exposed to separate 100 mL slowly stirred solutions of NH_2Cl and $HOCl/OCl^-$. Dissolved CO_2 was not excluded from the solutions. After treatment in disinfectant solutions, the mass of PbO_2 was determined as a function of time by monitoring the frequency change of the EQCM electrode using a Seiko model QCA917 quartz crystal analyzer in conjunction with a Nicolet Pro10 oscilloscope. A gate time of 1 s and an output range of ±20 kHz/10V were used with the analyzer.

Lead service line experiments

Lead service lines that had been removed from service were received from the City of Grand Rapids Water System, Lake Michigan Filtration Plant, MI. These lead service lines were 30 cm in length with a 1.2 cm inner diameter and a 2.8 cm outer diameter. One of the pipes was cut into ring segments approximately 2.5 cm thick with a pipe cutter. Each segment was then cut open with aviation snips to yield 4 samples. Each sample was wrapped in Kimwipes® and flattened with a vise. A flat specimen is necessary for the XRD measurements. The surface inside the lead service line was covered with yellow and white particles. Several layers of transparent nail polish were applied to the back, sides, and around the surface so that only the surface films were exposed with an area of approximately 0.8 cm^2. Each sample was immersed in 1 mM free chlorine and in 1 mM NH_2Cl at pH 8 for 24 hrs.

XRD and SEM instrumentation

Grazing incidence XRD patterns were obtained with a Philips X'Pert diffractometer using Cu Kα source radiation with an X-ray mirror (PW3088/60) as the incident beam module and a 0.18º parallel plate collimator as the diffracted beam module. A fixed incident angle of 1º was maintained, and the instrument was operated in the continuous mode with a step size of 0.03º and a counting time of 5 s. SEM micrographs were obtained with a Hitachi model S-4700 cold field-emission scanning electron microscope.

Results and Discussion

Dissolution rate of PbO_2 in NH_2Cl as a function of concentration

The changes in mass and dissolution rate of PbO_2 films in NH_2Cl solution at different concentrations at pH 7 are shown in Figure 1. The dissolution rate studies were repeated 3 times for each concentration and the error bars indicate one standard deviation. The rates of PbO_2 dissolution are determined for 0, 3, 10, 20, 35, and 50 ppm NH_2Cl. Each line in Figure 1a shows the PbO_2 mass decrease for each NH_2Cl concentration when the electrode is treated for 2.5 hours. Taking the slopes from the lines in Figure 1a, the PbO_2 film dissolution rate can be determined for each concentration and plotted in Figure 1b. The film dissolves more quickly as the NH_2Cl concentration increases. The dissolution rates in 0, 3, 10, 20, 35, and 50 ppm NH_2Cl are $(3.2 \pm 1.7) \times 10^{-3}$, $(3.4 \pm 1.8) \times 10^{-3}$, $(9.1 \pm 9.3) \times 10^{-3}$, $(9.0 \pm 7.1) \times 10^{-3}$, $(16 \pm 7.2) \times 10^{-3}$, and $(25 \pm 6.9) \times 10^{-3}$ μg/min, respectively.

Dissolution of PbO_2 in NH_2Cl at different pHs

Figure 2 shows the mass of electrodeposited α-PbO_2 films as a function of time in 1 mM NH_2Cl solution at different pHs. The PbO_2 dissolution rate increases as the pH decreases. During a 22 hour period, the decrease in mass of the 55 μg as-deposited PbO_2 film is 17, 2.5, 0.12, and 0.21 μg for pH 7, 8, 9, and 10, respectively. After treatment, all sample surfaces contain red films, which are consistent with the red color of PbO_2. XRD analysis confirms that all samples contain only α-PbO_2.

Dissolution of PbO_2 in NH_2Cl, $HOCl/OCl^-$, and NH_2Cl+phosphate at pH 7

Figure 3 shows the change in mass of electrodeposited PbO_2 films in NH_2Cl, $HOCl/OCl^-$, and NH_2Cl + 0.05 mM phosphate at pH 7. The mass vs. time plots show that

the PbO_2 film treated in NH_2Cl solution has a mass decrease of 17 μg (Figure 3a), as compared with the film treated in $HOCl/OCl^-$ solution, which has a mass increase of 0.5 μg (Figure 3b). However, when 0.05 mM phosphate is added to the NH_2Cl solution at the same pH, the film is passivated and a mass of 3.5 μg is gained (Figure 3c). Glancing-angle XRD patterns of the films are shown in Figure 4(a-d). Figures 4e and 4f also show powder diffraction pattern files for α-PbO_2 and $Pb_5(PO_4)_3OH$, respectively. The XRD pattern of the as-deposited 0.3 μm thick PbO_2 film without any treatment shows that the film is PbO_2. After treatment in NH_2Cl solution (Figure 4b) and $HOCl/OCl^-$ solution (Figure 4c) at pH 7, the PbO_2 film shows the same XRD pattern as it did before treatment. However, the XRD peak intensity of the PbO_2 film in NH_2Cl is greatly reduced, which suggests that less material is on the electrode surface. The XRD pattern of the PbO_2 film treatment in NH_2Cl+phosphate (Figure 4d) shows that the electrode surface consists of PbO_2 and lead phosphate hydroxide ($Pb_5(PO_4)_3OH$). The Au substrate peaks are marked with an asterisk. The Pb is divalent in this compound.

Figure 5 (a-d) shows the SEM micrographs that correspond to the films in Figure 4 (a-d). The morphology of the PbO_2 film without any treatment is uniform and shows PbO_2 particles with a particle size of approximately 400-600 nm. After the film has been treated in NH_2Cl, the surface morphology is completely changed (Figure 5b). The film dissolves and PbO_2 particles are etched, which is consistent with the EQCM experiment and XRD pattern. The morphology of the PbO_2 film after treatment in $HOCl/OCl^-$ is similar to that of the film before treatment (Figure 5c). The SEM image along with the EQCM experiment and XRD suggest that PbO_2 is quite stable in free chlorine solution. Figure 5d shows the PbO_2 film after treatment in 1 mM NH_2Cl+0.05 mM phosphate. The

image reveals a formation of fibers that cover the surface of PbO_2. Spot-mode EDS performed on these fibers indicated that they contain 2.2 atom % of phosphorous. Glancing-angle XRD also confirmed that the film had $Pb_5(PO_4)_3OH$ (hydropyromorphite). The low coverage of $Pb_5(PO_4)_3OH$ suggests a slow rate of film formation, as mentioned by Schock (5). The SEM image in Figure 5d is in agreement with the EQCM experiment in Figure 3c, showing that the mass of PbO_2 continued to increase because of the $Pb_5(PO_4)_3OH$ film formation, which can serve as passivation layers for PbO_2.

Measured equilibrium potentials for free chlorine and NH_2Cl are consistent with the EQCM results. Figure 6 shows the E-pH diagram for lead in water along with the measured equilibrium potentials (also referred to as oxidation-reduction potentials, or ORPs) of NH_2Cl and free chlorine. Details of the procedure used to prepare these solutions and the instrumentation used for ORP measurements can be found elsewhere (11). The concentration of DIC is set to 1.5 mM (18 ppm), which is the value previously used by Schock et al. (13). Dissolved Pb (II) species concentrations are set to 7.2×10^{-8} M (15 ppb), which is the EPA action level for Pb in drinking water. The Gibbs free energies of formation of the Pb species at 298 K and 1 atm used to calculate the equilibrium constants and standard reduction potentials for the chemical and electrochemical reactions of different Pb species are given by Schock et al. (6). James et al. previously reported the effect of oxidant type and concentration on the ORP in carbonate buffered solution as a function of pH (22). Figure 5 is similar to the Pourbaix diagram shown by Rajasekharan et al. (11). However, more equilibrium potential measurements of NH_2Cl were added to the plot from pH 7-8, which is relevant to the pH

range used in this study. The oxygen reduction reaction (i.e., $O_2 \rightarrow H_2O$) is also included in the figure as a dashed line. The thick solid lines are the calculated formal potential for the Pb^{2+} and DIC concentrations given above. The thin solid blue and red lines are linear fits for the free chlorine and NH_2Cl measured equilibrium potentials, respectively. All measurements for NH_2Cl and free chlorine were performed on a Au electrode in solutions containing equimolar quantities of the redox species in 60 mM buffered solution.

As shown in Figure 6, the measured equilibrium potentials for free chlorine are more positive than those of NH_2Cl for pH values relevant to drinking water, which shows that NH_2Cl is a less powerful oxidant than free chlorine. These results are in agreement with the EQCM results in Figure 3, in which there is no mass loss for the PbO_2 film in free chlorine solution. Figure 6 also indicates that PbO_2 is thermodynamically stable in free chlorine, but is dissolved as Pb^{2+} or forms other soluble Pb(II) species such as $Pb(CO_3)^0$ in a solution of NH_2Cl at a pH lower than approximately 9.5. As the pH decreases from 9 to 7, the measured equilibrium potentials for NH_2Cl are more negative than the formal potential for Pb^{2+}/PbO_2. Again, this is in agreement with the EQCM results in Figure 2 which show that PbO_2 film dissolves more rapidly as the pH decreases.

Our results have shown that the dissolution of PbO_2 does occur in NH_2Cl. Another point that we would like to address in the paper is the mechanism of dissolution of PbO_2. That is, does the material dissolve as Pb(IV), or is the Pb(IV) first reduced to Pb(II) which then dissolves. Solubility products provide some guidance to address this question. To confirm that PbO_2 film does not dissolve in the solution as Pb(IV), but rather is reduced to Pb(II), the amount of dissolved species in equilibrium with its solid

form can be calculated from the solubility products (K_{sp}). The K_{sp} values for β-PbO_2 (23) and PbO (6) are given in eq 1-2.

$$PbO_2 + 2H_2O \leftrightarrows Pb^{4+} + 4OH^- \qquad K_{sp} = 10^{-65.49} \quad (1)$$

$$PbO + H_2O \leftrightarrows Pb^{2+} + 2OH^- \qquad K_{sp} = 10^{-14.92} \quad (2)$$

Using the solubility-product expression ($K_{sp} = [A]^a[B]^b$), the calculated mass decrease in solution for PbO_2 dissolved as Pb^{4+} would be 5.45×10^{-6} μg. If, however, PbO_2 is allowed to reduce to PbO, the solid will dissolve as Pb^{2+} and a mass of 1387 μg will be lost. The calculated mass decrease for PbO_2 dissolved as Pb^{4+} is too small compared with the measured EQCM results in Figure 1a with 0 ppm NH_2Cl. Therefore, it is more probable that PbO_2 is reduced and dissolved as Pb^{2+} ions in the solution. Finally, the XRD in Figure 4d also confirms the presence of Pb(II) species as $Pb_5(PO_4)_3OH$ when phosphate is added in the NH_2Cl solution, indicating that PbO_2 is reduced to Pb(II). Hence, the phosphate experiments provide additional evidence that the Pb(IV) is reduced to Pb(II) by NH_2Cl.

In this study, we show through EQCM results and measured equilibrium potentials that PbO_2 dissolves in NH_2Cl disinfectant solution. However, the reducing agent that causes the dissolution of PbO_2 to Pb^{2+} has not been identified. Therefore, we performed two control experiments. In our first hypothesis, we consider the reduction of PbO_2 by Cl^- according to the half and net redox reactions in acidic solution given in eq 3-5.

$$NH_2Cl + 2H^+ + 2e^- \leftrightarrows Cl^- + NH_4^+ \qquad E^0 = 1.4 \text{ V vs NHE} \quad (3)$$

$$PbO_2 + 4H^+ + 2e^- \leftrightarrows Pb^{2+} + 2H_2O \qquad E^0 = 1.455 \text{ V vs NHE} \quad (4)$$

$$PbO_2 + Cl^- + NH_4^+ + 2H^+ \leftrightarrows Pb^{2+} + NH_2Cl + 2H_2O \qquad E^0 = 0.055 \text{ V vs NHE} \quad (5)$$

A PbO_2 film was immersed in a solution containing 1 mM Cl^- and 4 mM NH_4^+ at pH 7. The plot of mass vs. time reveals that the PbO_2 loses mass by only 2.40 μg after the experiment. Spectrophotometry does not show any evidence for NH_2Cl, suggesting that oxidation of Cl^- to NH_2Cl (reaction 5) is not occurring. In addition, this control experiment suggests that the PbO_2 does not dissolve by complexing the Pb(IV) with ammonia.

A second hypothesis for PbO_2 dissolution is the reduction of PbO_2 to Pb^{2+} by water. In this case, the water would be oxidized to molecular oxygen. The calculated formal reduction potential for O_2/H_2O at pH 7 is 0.816 V vs NHE, which is more negative than the formal reduction potential for PbO_2 at pH 7, suggesting that water can reduce PbO_2 to Pb^{2+} at this pH. A control experiment of PbO_2 immersed in pure water at pH 7 without NH_2Cl was also carried out. The plot of mass vs. time indicates a PbO_2 mass decrease of only 0.92 μg.

These control experiments suggest that neither species mentioned above is the active reducing agent for PbO_2. The reduction of PbO_2 to Pb^{2+} in NH_2Cl solution may be caused by a decomposition product of NH_2Cl. Margerum et al. have shown that NH_2Cl oxidizes nitrite ion by means of an acid-catalyzed transfer of Cl^+ from NH_2Cl to NO_2^-, producing NO_2Cl as an intermediate (24). Other unidentified intermediate species, such as the amidogen radical (NH_2•), may also be involved in NH_2Cl reduction. Piela and Wrona have described the reduction mechanism of monochloramine that leads to the production of the amidogen radical (NH_2•) in the rate-determining step (25). According to Vikesland and Valentine, this radical can combine with itself to form hydrazine, N_2H_4 (26). Hydrazine is a reducing agent that could reduce PbO_2 to Pb^{2+}.

Experiments with lead service lines

Figure 7 shows glancing-angle XRD patterns and the corresponding optical micrographs of a lead service line from Grand Rapids, MI before and after treatment in 1 mM free chlorine and 1 mM NH_2Cl at pH 8 for 24 hours. The surface of all the samples before treatment was covered with yellow and white powder. The glancing-angle XRD in Figure 7a shows that the powder mostly consists of $Pb_3(CO_3)_2(OH)_2$ and PbO (litharge) with a small amount of β-PbO_2. After the sample was treated in free chlorine, the surface changed color from white and yellow to reddish brown; and additional peaks of α-PbO_2 and PbClOH are present in the XRD pattern (Figure 7b). The same pipe sample was then immersed in NH_2Cl. The XRD pattern in Figure 7c shows that the β-PbO_2 peak at $2\theta = 25.39^o$ almost disappears and the α-PbO_2 peak at $2\theta = 23.31^o$ completely disappears (shown by arrows), confirming that the NH_2Cl reduces α-PbO_2 to Pb(II) species. The PbClOH peak also disappears from the pattern. The surface of the lead pipe also changes from reddish brown to white. It should be noted from the XRD pattern that, after treatment in NH_2Cl, the PbO changes its polymorph from litharge to massicot. The same Pb pipe sample was used in Figure 7 (a-c). These experiments were performed on 4 separate samples, which all showed similar results.

We have shown in our previous work that NH_2Cl can increase the Pb levels in water by oxidizing a pure Pb film to Pb^{2+} (10). However, in real water systems, pure Pb pipes are not exposed to NH_2Cl. The pipes are already covered with passivation layers, such as $PbCO_3$, $Pb_3(CO_3)_2(OH)_2$, $Pb_5(PO_4)_3OH$, PbO, and PbO_2. Other studies have suggested that PbO_2 could be a good passivation material to control the plumbosolvency problem (13,14). This paper shows direct evidence that NH_2Cl can also affect the

dissolution of PbO_2. Although the mechanism of the reduction of PbO_2 to Pb^{2+} in NH_2Cl is not fully understood, the EQCM results show that PbO_2 films are unstable in NH_2Cl solution, especially at neutral pH. The addition of orthophosphate to a water system with an NH_2Cl disinfection program should minimize the reduction of the PbO_2 films by producing a $Pb_5(PO_4)_3OH$ passivation film.

Acknowledgement: This work was supported by NSF grants CHE-0437346 and DMR-0504715. The authors are grateful to John. T. Wierenga of the City of Grand Rapids Water System, Lake Michigan Filtration Plant, MI for providing lead service line samples.

References

(1) U.S. Environmental Protection Agency. Drinking water regulations: Maximum contaminant level goals and national primary drinking water regulations for lead and copper, final rule; correction. *Fed. Regis*. **1991a**, *56*, 32112.

(2) U.S. Environmental Protection Agency. Maximum contaminant level goals and national primary drinking water regulations for lead and copper, final rule. *Fed. Regis*. **1991b**, *56*, 26460-26564.

(3) U.S. Environmental Protection Agency. Drinking water regulations: Maximum contaminant level goals and national primary drinking water regulations for lead and copper, final rule; correcting amendments. *Fed. Regis*. **1992**, *57*, 28785-28789.

(4) Schock, M. R.; Gardels, M. C. Plumbosolvency reduction by high pH and low carbonate-solubility relationships. *J. Am. Water Works Assoc*. **1983**, *75*, 87-91.

(5) Schock, M. R. Understanding corrosion control strategies for lead. *J. Am. Water Works Assoc*. **1989**, *81*, 88-100.

(6) Schock, M. R.; Wagner, I.; Oliphant, R. J. In *Internal corrosion of water distribution systems*, 2nd ed.; AWWA: Denver, CO, 1996; pp 131-230.

(7) Johnson, J. Drinking water review planned. High lead levels in Washington, D.C.; water trigger broad research study. *Chem. Eng. News*. **2004**, *82*, 9.

(8) Edwards, M.; Dudi, A. Role of chlorine and chloramines in corrosion of lead-bearing plumbing materials. *J. Am. Water Works Assoc*. **2004**, *96*, 69-81.

(9) Renner, R. Chloramines again linked to lead in drinking water. *Environ. Sci. Technol.* **2005**, *39*, 314A-315A.

(10) Switzer, J. A.; Rajasekharan, V. V.; Boonsalee, S.; Kulp, E. A.; Bohannan, E. W. Evidence that monochloramine disinfectant could lead to elevated Pb levels in drinking water. *Environ. Sci. Technol.* **2006**, *40*, 3384-3387.

(11) Rajasekharan, V. V.; Clark, B. N.; Boonsalee, S.; Switzer, J. A. Electrochemistry of free chlorine and monochloramine and its relevance to the presence of Pb in drinking water. *Environ. Sci. Technol.* **2007**, *41*, 4252-4257.

(12) Renner, R. Plumbing the depths of D.C.'s drinking water crisis. *Environ. Sci. Technol.* **2004**, *38*, 224A-227A.

(13) Schock, M.R.; Harmon, S. M.; Swertfeger, J.; Lohmann R. Tetravalent lead: a hitherto unrecognized control of tap water lead contamination. *Proc.-Water Quality Technol. Conf.* **2001**, 2270-2291.

(14) Lytle, D. A.; Schock, M. R. Formation of Pb(IV) oxides in chlorinated water. *J. Am. Water Works Assoc.* **2005**, *97*, 102-114.

(15) Renner, R. Chloramine's effect on lead in drinking water. *Environ. Sci. Technol.* **2006**, *40*, 3129-3130.

(16) Buttry, D. A.; Ward, M. D. Measurement of interfacial processes at electrode surfaces with the electrochemical quartz crystal microbalance. *Chem. Rev.* **1992**, *92*, 1355-1379.

(17) Wei, C.; Rajeshwar, K. In situ characterization of lead corrosion layers by combined voltammetry, coulometry, and electrochemical quartz crystal microgravimetry. *J. Electrochem. Soc.* **1993**, *140*, L128-L130.

(18) Wang, K.; Pickering, H. W.; Weil, K. G. Corrosion inhibition of zinc by benzotriazole with an electrochemical quartz crystal microbalance. *J. Electochem. Soc.* **2003**, *150*, B176-B180.

(19) Yiin, B. S.; Margerum, D. W. Non-metal redox kinetics: Reactions of trichloramine with ammonia and with dichloramine. *Inorg. Chem.* **1990**, *29*, 2135-2141.

(20) Qiang, Z.; Adams, C. D. Determination of monochloramine formation rate constants with stopped-flow spectrophotometry. *Environ. Sci. Technol*. **2004**, *38*, 1435-1444.

(21) Vertegel, A. A.; Bohannan, E. W.; Shumsky, M. G.; Switzer, J. A. Epitaxial electrodeposition of orthorhombic α-PbO2 on (100)-oriented single crystal Au. *J. Electrochem. Soc.* **2001**, *148*, C253-C256.

(22) James, C. N.; Copeland, R. C.; Lytle, D. A. Relationships between oxidation-reduction potential, oxidant, and pH in drinking water. In *Proceedings of the AWWA Water Quality Technology Conference*, San Antonio, Texas, November 14-18, 2004; pp 1-13.

(23) Glasstone, S. Physical chemistry of the oxides of lead. Part V. The electromotive behaviour of lead dioxide. *J. Chem. Soc, Trans*. **1992**, *121*, 1469-1480.

(24) Margerum, D. W.; Schurter, L. M.; Hobson, J.; Moore, E. E. Water chlorination chemistry: Nonmetal redox kinetics of chloramines and nitrite ions. *Environ. Sci. Technol.* **1994**, *28*, 331-337.

(25) Piela, B.; Wrona, P. K. Electrochemical behavior of chloramines on the rotating platinum and gold electrodes. *J. Electrochem. Soc.* **2003**, *150*, E255-E265.

(26) Vikesland, P. J.; Valentine, R. L. Reaction pathways involved in the reduction of monochloramine by ferrous iron. *Environ. Sci. Technol.* **2000**, *34*, 83-90.

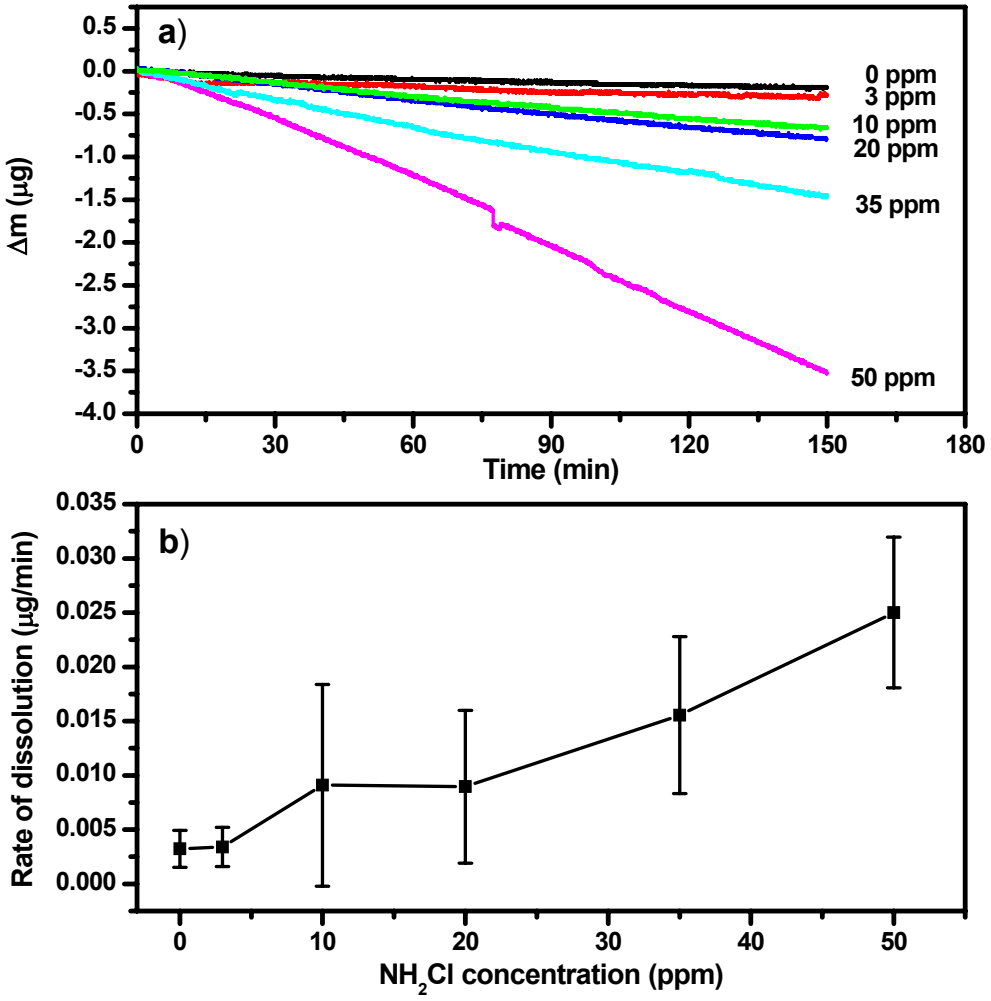

Figure 1: (a) EQCM measurements of the change in mass of 0.3 μm thick PbO_2 films immersed in 0, 3,10, 20, 35, and 50 ppm NH_2Cl solution at pH 7. (b) Rate of PbO_2 dissolution as a function of the NH_2Cl concentration.

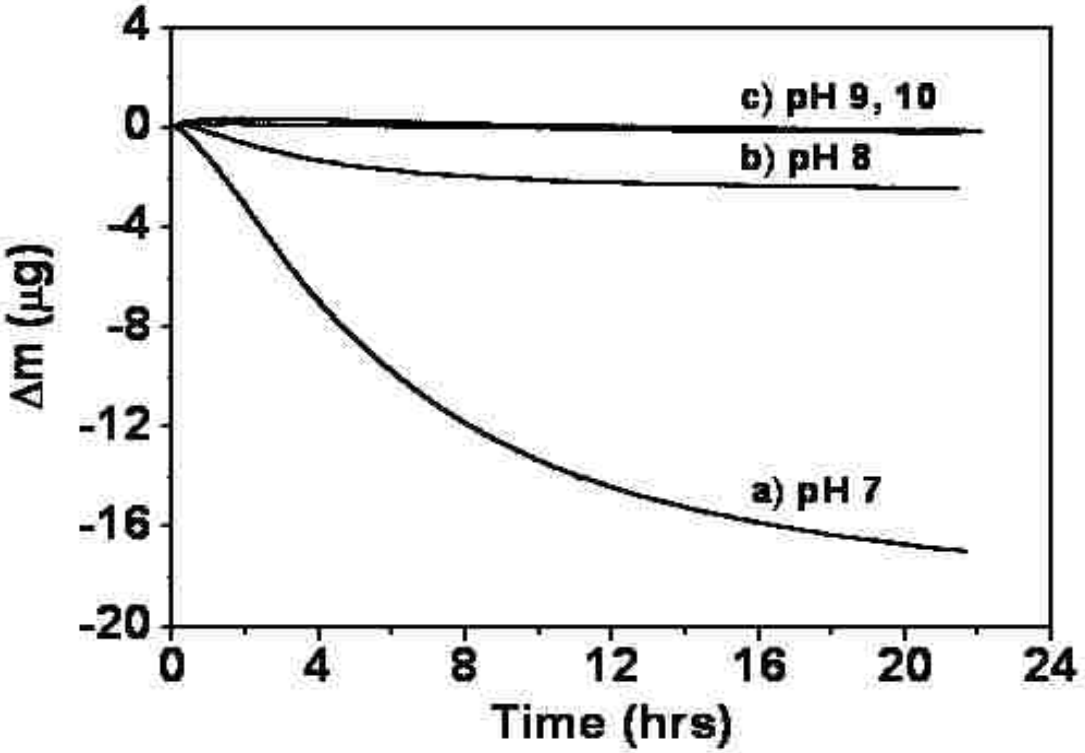

Figure 2: EQCM measurements of the change in mass of 0.3 μm thick PbO_2 fims immersed in 1 mM NH_2Cl solution at (a) pH 7, (b) pH 8, and (c) pH 9 and 10. The total PbO_2 mass deposited was 55 μg.

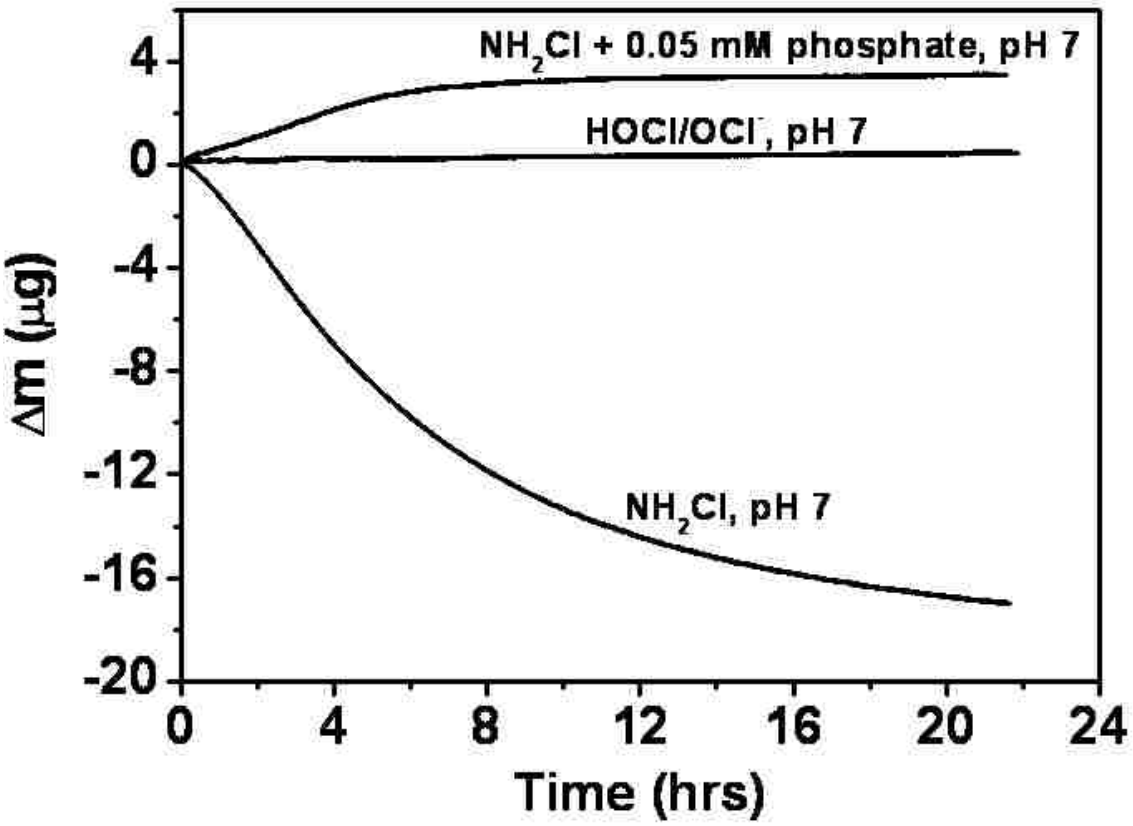

Figure 3: EQCM measurement of the change in mass of 0.3 μm thick PbO_2 films immersed in solution at pH 7 of (a) 1 mM NH_2Cl, (b) 1 mM free chlorine, and (c) 1 mM NH_2Cl + 0.05 mM orthophosphate.

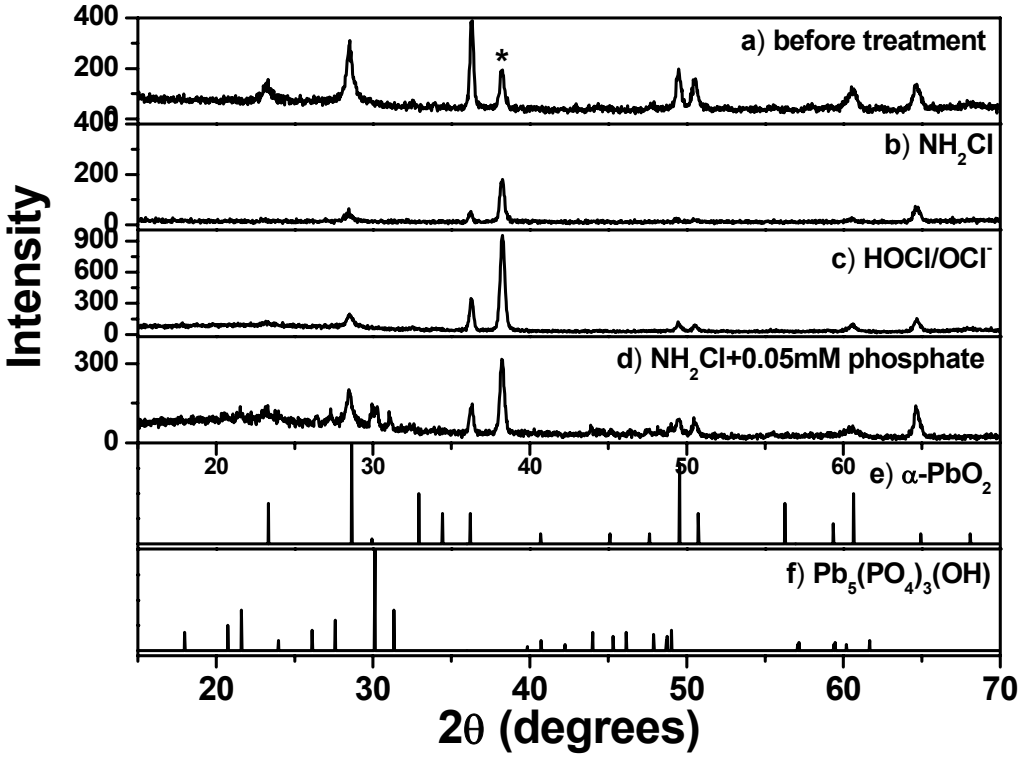

Figure 4: Glancing-angle X-ray diffraction patterns of 0.3 μm thick PbO_2 films (a) as-deposited, (b) after immersion of 1 mM NH_2Cl at pH 7, (c) after immersion of 1 mM free chlorine at pH 7, and (d) after immersion of 1 mM NH_2Cl+0.05 mM orthophosphate at pH 7. The standard powder patterns for (e) α-PbO_2 and (f) $Pb_5(PO_4)_3OH$ are also shown. The Au(111) peaks marked with an asterisk at 2θ = 38.18º are from the Au-coated EQCM electrode.

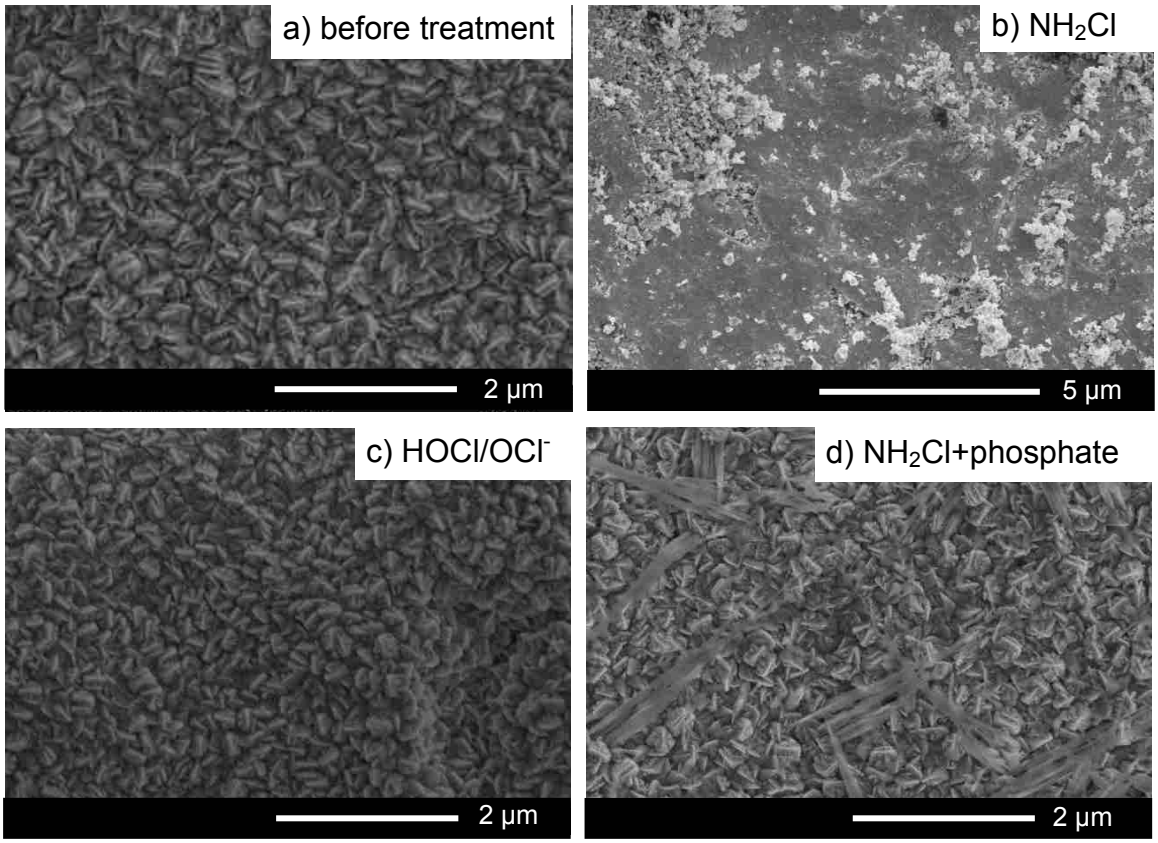

Figure 5: Scanning electron micrographs of 0.3 µm thick PbO_2 films (a) as-deposited, (b) after immersion in 1 mM NH_2Cl at pH 7, (c) after immersion in 1 mM free chlorine at pH 7, and (d) after immersion in 1 mM NH_2Cl+0.05 mM orthophosphate at pH 7.

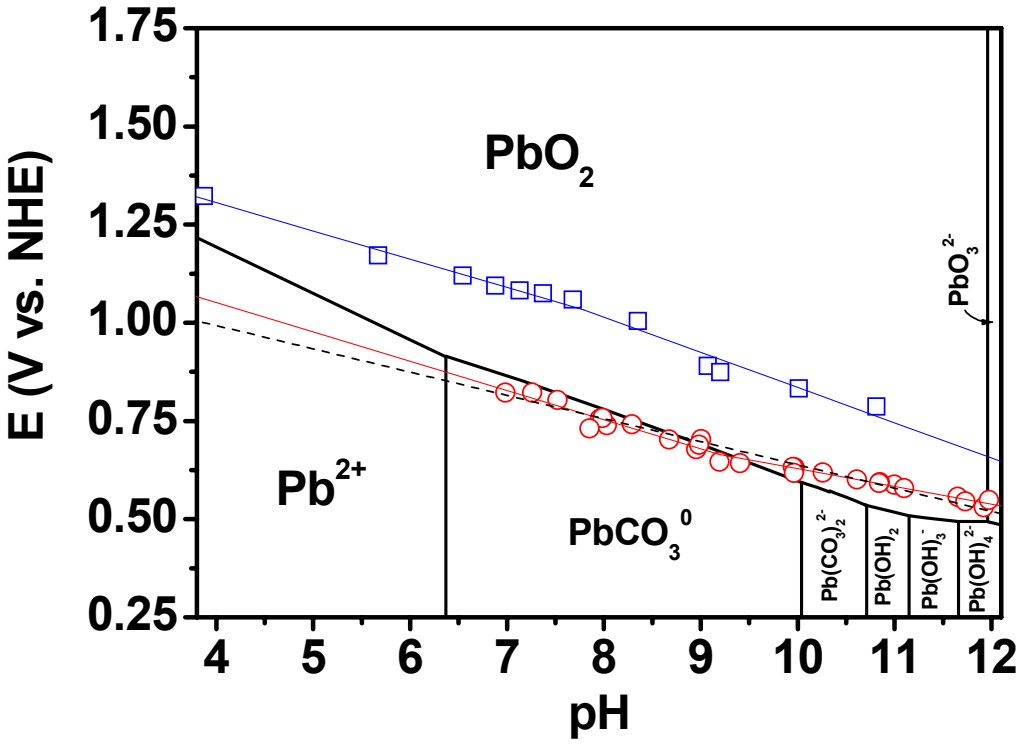

Figure 6: E-pH (Pourbaix) diagram for lead with the concentration of dissolved Pb species equal to 7.25 x 10^{-8} M (15 ppb) and the dissolved inorganic carbon (DIC) concentration equal to 1.5 x 10^{-3} M (18 ppm) at 25 ºC. Measured equilibrium potentials are shown as blue open squares for free chlorine and as red open circles for NH_2Cl. A linear fit to the measured equilibrium potentials for free chlorine or NH_2Cl gives two linear regions. Below pH 7.5 (pK_a HOCl = 7.5) the slope is 72 mV/pH, and above pH 7.5 the slope is 90 mV/pH. A linear fit to measured equilibrium potentials for NH_2Cl below pH 9.5 (pK_a NH_2Cl = 9.5) has a slope of 75 mV/pH, and above pH 9.5 has a slope of 45 mV/pH. The linear fit for NH_2Cl crosses the $PbCO_3^0/PbO_2$ boundary at pH 9.4.

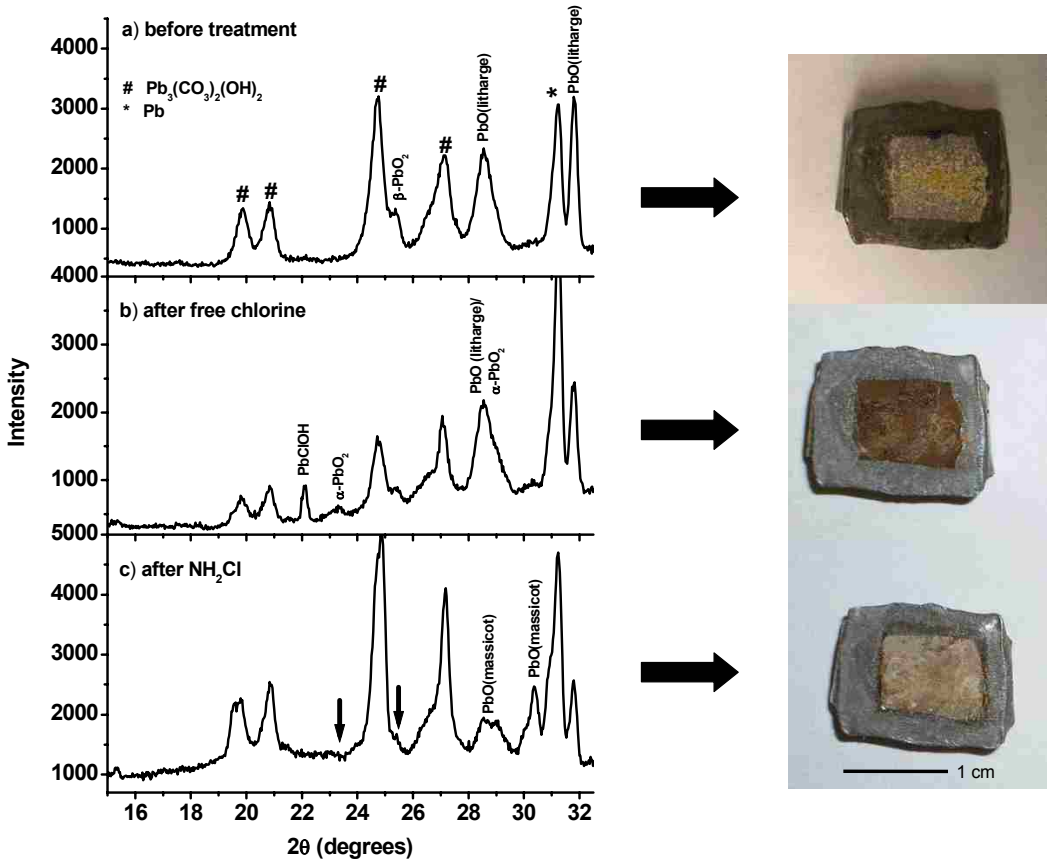

Figure 7: Glancing-angle X-ray diffraction patterns and optical micrographs of an actual Pb service line sample (a) before treatment, (b) after immersion in 1 mM free chlorine at pH 8, and (c) after immersion in 1 mM NH_2Cl at pH 8 (black arrows indicate the disappearance of PbO_2). The reflections from $Pb_3(CO_3)_2(OH)_2$ and Pb are marked with sharps (#) and an asterisk (*), respectively.

PAPER IV

Epitaxial Electrodeposition of SnS Nanodisks on Single-Crystal Au(100)

Sansanee Boonsalee, Rakesh V. Gudavarthy, Eric W. Bohannan, and Jay A. Switzer[*]

Department of Chemistry and Graduate Center for Materials Research
Missouri University of Science and Tehnology, Missouri, U.S.A 65409-1170
Email: jswitzer@mst.edu

ABSTRACT. Epitaxial nanodisks of tin sulfide (δ-SnS) are deposited electrochemically on a [100]-oriented single crystal Au substrate from an acidic solution at 70 ºC. The δ-SnS grows with two different out-of-plane orientations of [100] and [301] and four equivalent in-plane orientations. X-ray pole figures reveal the following epitaxial relationships: SnS(100)[010]//Au(100)[010], SnS(100)$[0\bar{1}0]$//Au(100)[010], SnS(100)[001]//Au(100)[010], SnS(100)$[00\bar{1}]$//Au(100)[010], SnS(301)[010]//Au(100)[010], SnS(301)$[0\bar{1}0]$//Au(100)[010], SnS(301)$[10\bar{3}]$//Au(100)[010], and SnS(301)$[\bar{1}03]$//Au(100)[010]. For the SnS(100) orientation, the in-plane mismatch is 2.4% in the [010] direction and 6.1% in the [001] direction. For the (301) orientation, the in-plane mismatch is 2.4% in the [010] direction and 3.4% in the $[10\bar{3}]$ direction. The δ-SnS deposits with a disk-like morphology with a diameter of 300 nm and a thickness of 50 nm.

Key words: electrodeposition, epitaxy, tin sulfide

INTRODUCTION

Epitaxial films are typically deposited onto single crystal substrates using vapor deposition. Recently, many research groups have utilized the electrochemical deposition method to produce epitaxial films.[1-6] The advantages of this method over other deposition methods are its versatility, high level of control, simplicity and economy. The deposition is usually carried out at or near room temperature, which helps minimize solid state diffusion between the film and substrate. The thickness of the film is easily controlled by the charge passed through the electrode. The electrochemical deposition method can be used to deposit materials on substrates of any shape or size. In addition, the departure from equilibrium is controlled through the applied overpotential, and the morphology of the deposits is often dependent on solution additives and pH. Our group has previously employed electrodeposition in aqueous solution to grow epitaxial films of δ-Bi_2O_3[7], Cu_2O[6,8], CuO[9], ZnO[10,11], Fe_3O_4[12], PbO_2[13], Tl_2O_3[14], and PbS[15] on single-crystal Au. We have also electrodeposited epitaxial Cu_2O films and nanostructures with tunable morphologies onto Si and InP single crystals.[16-18]

Tin sulfide is a p-type layered semiconductor with a band gap ranging from 1.05 to 1.48 eV[19-22] depending on the preparation method, which is near the optimum energy bandgap of 1.5 eV required for efficient light absorption for solar energy applications.[23] According to the recent study by Reddy and co-workers on the optical properties of SnS films, the optical bandgap of SnS depends strongly on the lattice parameters.[24] Reddy et al. have fabricated p-SnS/n-CdS polycrystalline thin films with a solar conversion efficiency of 1.3%.[25] Based on the bandgap of the material, a conversion efficiency of more than 25% is possible.[25,26] Additionally, Sn and S are inexpensive, environmentally

benign, and ubiquitous in nature.[19,20,22] These properties make SnS suitable for use in making photovoltaic and photoelectrochemical cells. SnS have been synthesized using many techniques including, for example, electrodeposition[19-22,27,28], pulse deposition[29,30], spray pyrolysis[31,32], chemical vapor deposition[33], and molecular beam epitaxy.[34]

Here, we show that epitaxial nanostructures of δ-SnS can be electrodeposited onto single-crystal Au(100). The SnS was electrodeposited by the method developed by Brownson et al.[19] from a solution of $SnCl_2$, thiosulfate, and L-tartaric acid at pH 2.5. Our motivation for depositing epitaxial δ-SnS on Au is twofold. First, we are interested in depositing high-aspect-ratio epitaxial deposits of the material for possible photoelectrochemical and photovoltaic applications. Electron-hole recombination should be minimized in the epitaxial structures because of the lack of grain boundaries in the direction perpendicular to the substrate. Also, the high aspect ratio should maximize collection of charge carriers. Recently, fabrication of high-aspect-ratio (length/diameter) semiconductors (Si, CdSe, CdTe) for photoelectrochemical and photovoltaic devices has attracted much attention compared with the conventional planar geometry.[35-38] The Lewis group has theoretically and experimentally shown that nanorod arrays of Cd(Se,Te) arranged perpendicular to the substrate enhance the overall efficiency. The design increases the charge carrier collection to the ultra-thin p-n junction that is parallel to the substrate but orthogonal to the light absorption.[35,39]. Our second motivation for studying this epitaxial system is that it provides fundamental information on the epitaxial growth of high-mismatch systems. δ-SnS has an orthorhombic structure (a = 11.380 Å, b = 4.029 Å, c = 4.837 Å),[20] whereas Au (a = 4.079 Å) has a face-centered cubic structure. We show in this work that mismatch is minimized when the δ-SnS deposits with the a

axis of δ-SnS oriented perpendicular to the surface of the Au(100) substrate. The δ-SnS nanostructures were characterized by X-ray diffraction, X-ray pole figures, and rocking curves. The film morphology was examined via scanning electron microscopy (SEM).

EXPERIMENTAL SECTION

SnS was deposited using the method developed by Brownson et al.[19] The deposition solution contained 50 mM $SnCl_2$, 150 mM $Na_2S_2O_3$ (sodium thiosulfate), 0.2 M L-tartaric acid, and 0.1 M HCl. The final pH of the solution was adjusted to 2.5 with 6 M NaOH. The bath temperature was maintained at 70 ºC. When sodium thiosulfate was added to the solution, colloidal sulfur formed due to thiosulfate disproportionation. The cell consisted of a platinum counter electrode and a Ag/AgCl reference electrode. The working electrode was an Au(100) single-crystal purchased from Monocrystal Company (diameter 10 mm, thickness 2 mm). A gold wire was wrapped around the single crystal to serve as an electrical contact. The Au(100) working electrode was placed in the solution using the meniscus method. Prior to deposition, the Au(100) single-crystal was electropolished and annealed in a hydrogen flame. Electropolishing was performed at a constant anodic current density of 1.5 A/cm^2 in a solution containing 50 vol % ethanol, 25 vol % ethylene glycol, and 25 vol % concentrated HCl at 55 ºC with a graphite counter electrode. The deposition solution was deaerated with Ar for 30 min prior to deposition to prevent the oxidation of Sn^{2+}. Argon gas was passed continually over the surface of the solution during deposition. The deposition was carried out in a fume hood. SnS films were deposited at a constant cathodic current density of 3 mA/cm^2 for 30 min with an EG&G Princeton Applied Research model 273A potentiostat/galvanostat.

X-ray diffraction (XRD) measurements were taken with a high–resolution Philips X'Pert diffractometer. The film XRD scan was obtained using Cu $K\alpha_1$ source radiation with a combination X-ray mirror and two-crystal Ge(220) two-bounce hybrid monochrometer. The secondary optics module was a 0.18º parallel plate collimator. Rocking curves were run using a triple axis/rocking curve assembly as the secondary optics. The instrumental broadening is 25 arcseconds. Pole figures were run on the same instrument in point-focus mode using a crossed slit collimator as the primary optics and a flat graphite monochrometer as the secondary optics. Stereographic projections were generated using Carine Crystallography Software (version 3.1). Scanning electron microscopy (SEM) images were taken with a Hitachi S-4700 cold field emission SEM at an accelerating voltage of 5 keV.

RESULTS AND DISCUSSION

The epitaxial deposition of SnS nanodisks are achieved by electrochemical reduction of $SnCl_2$ in the presence of $Na_2S_2O_3$ as a source of sulfur. The chemistry of tin monosulfide electrodeposition is described elsewhere.[20] The deposition current of 3 mA/cm^2 used in this study corresponds to the potential of approximately -0.45 V vs Ag/AgCl. This potential is 390 mV more positive than the potential of -0.86 V vs SCE reported by Brownson et al.[19] at the same current density, which is likely due to the higher electrical conductivity and catalytic activity of Au compared to the ITO. When a film is grown on a polycrystalline substrate such as stainless steel, the measured potential is -0.75 V vs Ag/AgCl.

The XRD θ-2θ diffraction pattern of the SnS deposit on Au(100) is shown in Figure 1. Only three peaks are observed for SnS, which correspond well to the (200),

(400), and (800) reflections of SnS. No other reflections are observed in the 2θ scan, indicating preferential [100] orientation of the film. Because only the {h00} type is observed in the diffraction pattern, only one lattice parameter can be determined (a = 11.31 Å). This value is similar to the a lattice parameter of δ-SnS polymorph reported by Brownson et al. (a = 11.380 Å, b = 4.029 Å, c = 4.837 Å).[20] However, when a polycrystalline SnS is deposited on stainless steel using the same bath condition, the lattice parameters are a = 11.22 Å, b = 3.989 Å, c = 4.328 Å. The lattice parameters obtained from the polycrystalline deposit are quite similar to the literature values of α-SnS (a = 11.18 Å, b = 3.982 Å, c = 4.329 Å, JCPDS no. 73-1859).[40] When the SnS(210) pole figure was run to determine the in-plane orientation of the film relative to the substrate, two different reflections that correspond to the [100] and [301] orientations can be seen. Pole figures are obtained by choosing a specific plane to probe while measuring the diffracted intensity as a function of tilt (χ) and rotation (φ). The (210) pole figure of the SnS is shown in Figure 2a, and the (111) pole figure of Au(100) is shown in Figure 2b. The radial grid lines in the pole figures correspond to 30º increments in χ. The SnS pole figure exhibits four equally-spaced ($\Delta\varphi$ = 90º) peaks at χ = 54º, which is in agreement with the calculated χ = 54.5º that corresponds to the angle between the (210) and (100) planes in SnS. The other eight peaks at χ = 64º agree well with the calculated χ = 63.9º, corresponding to the angle between the (210) and (301) planes. The average peak height in Figure 2a is 360 counts/s for the (100) reflections and 76 counts/s for the (301) reflections, which indicates that the SnS deposit has a majority [100] orientation. The XRD diffraction pattern only shows 3 peaks because the (400) and (301) reflections overlap ($2\theta_{400}$ = 31.995º and $2\theta_{301}$ = 31.655º).

To help verify the assignment of in-plane orientations from the pole figure, stereographic projections were generated (Figure 3). The stereographic projections in Figure 3 are constructed using the orthorhombic α-SnS structure, because the atomic positions for α-SnS structure are well known and because δ-SnS is a slightly distorted structure of α-SnS.[20] Figure 3a and 3b show the (100) and (301) stereographic projections, respectively, of orthorhombic α-SnS while probing the (210)-type reflections. In Figure 3a, the spots at $\chi = 54.5^{\circ}$ are assigned to the {210} reflections due to the [100] orientation. Similarly, the spots at $\chi = 63.9^{\circ}$ correspond to the {210} reflections in Figure 3b due to the [301] orientation. Figure 3a and 3b are the resulting stereographic projections, assuming that only one domain of each orientation is deposited. However, the Au(100) substrate has four-fold symmetry, so it is reasonable to expect four domains of each orientation being deposited on the surface. Overlaying Figure 3a and 3b on top of each other, then rotating the image by 90º, 180º, and 270º results in the stereographic projection shown in Figure 3c. The stereographic projection matches the experimentally observed pole figure shown in Figure 2a. The Au(111) pole figure in Figure 2b has four equally spaced peaks at $\chi = 55^{\circ}$, which is consistent with the angle between (111) and (100) planes in the cubic system. By comparing the two pole figures with the calculated stereographic projections, the in-plane orientation of SnS on Au is determined. The epitaxial relationships can be expressed as SnS(100)[010]//Au(100)[010], SnS(100)$[0\bar{1}0]$//Au(100)[010], SnS(100)[001]//Au(100)[010], SnS(100)$[00\bar{1}]$//Au(100)[010], SnS(301)[010]//Au(100)[010], SnS(301)$[0\bar{1}0]$//Au(100)[010], SnS(301)$[10\bar{3}]$//Au(100)[010], and SnS(301)$[\bar{1}03]$//Au(100)[010]. The SnS structure is

characterized as layers of double planes.[19,20,41] Each plane consists of Sn-S bonds arranged in zigzag chains that are parallel to the substrate (perpendicular to the *a*-axis)[19]. For the SnS(100) plane, the spacing between two adjacent sulfur atoms is 3.982 Å along the *b*-axis and 4.329 Å along the *c*-axis. By comparing the spacings between sulfur atoms and Au atoms (4.079 Å), the lattice mismatch is calculated to be 2.4% in the [010] in-plane direction and 6.1% in the [001] in-plane direction. Hence, the system minimizes the lattice mismatch by placing the larger *a* lattice parameter (11.380 Å) perpendicular to the substrate. The *b* (4.029 Å) and *c* (4.837 Å) lattice parameters are similar to each other, and they are closer in value to the lattice parameter (4.079Å) of the Au substrate. For the SnS[301] orientation, the (301) plane is also aligned with the Au. The distance between two sulfur atoms in the [010] direction is 3.982 Å and the $[10\bar{3}]$ direction is 8.437Å. The mismatches in the [010] and $[10\bar{3}]$ in-plane directions are 2.4% and 3.4%, respectively.

The quality of the epitaxial δ-SnS nanostructure can be obtained by x-ray azimuthal scans and x-ray rocking curves. An azimuthal scan is a cross section of a pole figure at a tilt angle, χ, which corresponds to the maximum intensity of the reflections in the pole figure. Figure 4 shows azimuthal scans for the (210) reflections of δ-SnS at a tilt angle of 54.5º. The expected four-fold symmetry is observed for the δ-SnS deposit and the substrate. The average full width at half-maximum (fwhm) of δ-SnS is 3.16º. The average peak intensity of δ-SnS relative to the background is 16 to 1, indicating that δ-SnS has a [100] orientation with little or no fiber texture. If the deposit had a fiber texture, the ratio between the average peak intensity relative to the background would be 1:1. Figure 5a and 5b show the x-ray rocking curves of SnS(400)/(301) and Au(200).

The fwhm of SnS(400)/(301) and Au(200) are 2.9º and 0.23º, respectively. These results indicate that δ-SnS has a [100] out-of-plane orientation with a 2.9º mosaic spread.

Scanning electron micrographs of δ-SnS electrodeposited with a cathodic current density of 3 mA/cm^2 are shown in Figure 6a and 6b at two different magnifications. The thickness of the δ-SnS deposit is approximately 800 nm, as determined by cross-section analysis on Au sputtered on glass. The morphology of the δ-SnS deposit has a disk-like structure. The disks are approximately 300 nm in diameter and 50 nm in thickness. The ratio of Sn:S is 1:1.08 when measured by energy-dispersive spectroscopy (EDS).

CONCLUSION

Epitaxial δ-SnS nanodisks are electrodeposited on Au(100) single crystal using the cathodic deposition approach. The deposition solution was originally developed by Brownson et al.[19] The δ-SnS deposit grows with two different in-plane orientations of (100) and (301), which are aligned with the Au substrate. The two orientations can only be distinguished by x-ray pole figures. The quality of the δ-SnS is analyzed by azimuthal and rocking curve scans. The rocking curve shows that the film has a 2.9º mosaic spread. EDS also confirms a 1:1 Sn to S ratio. For photovoltatic and photoelectrochemical applications, it will be interesting in future work to deposit δ-SnS on less expensive Au-sputtered glass which has a [111] orientation. It will also be interesting to deposit epitaxial SnS/Si and SnS/InP heterojunctions.

ACKNOWLEDGMENT. This work was supported by NSF grant DMR-0504715.

REFERENCES

(1) Pauporte, Th.; Cortes, R.; Froment, M.; Beaumont, B.; Lincot, D. *Chem. Mater*. **2002**, *14*, 4702.

(2) Froment, M.; Bernard, M. C.; Cortes, R.; Mokili, B.; Lincot, D. *J. Electrochem. Soc*. **1995**, *142*, 2642.

(3) Colletti, L. P.; Flowers, B. H. Jr.; Stickney, J. L. *J. Electrochem. Soc*. **1998**, *145*, 1442.

(4) Yang, F. Y.; Liu, K.; Hong, K.; Reich, D. H.; Searson, P. C.; Chien, C. L. *Science* **1999**, *284*. 1335.

(5) Mallett, J. J.; Svedberg, E. B.; Vaudin, M. D.; Bendersky, L. A.; Shapiro, A. J.; Egelhoff, W. F. Jr.; Moffat, T. P. *Phys. Rev. B*. **2007**, *75*, 085304.

(6) Bohannan, E. W.; Shumsky, M. G.; Switzer, J. A. *Chem. Mater*. **1999**, *11*, 2289.

(7) Switzer, J. A.; Shumsky, M. G.; Bohannan, E. W. *Science* **1999**, *284*, 293.

(8) Switzer, J. A.; Kothari, H. M.; Bohannan, E. W. *J. Phys. Chem. B*. **2002**, *106*, 4027.

(9) Switzer, J. A.; Kothari, H. M.; Poizot, P.; Nakanishi, S.; Bohannan, E. W. *Nature* **2003**, *425*, 490.

(10) Liu, R.; Vertegel, A. A.; Bohannan, E. W.; Sorenson, T. A.; Switzer, J. A. *Chem. Mater*. **2001**, *13*, 508.

(11) Limmer, S. J.; Kulp, E. A.; Switzer, J. A. *Langmuir* **2006**, *22*, 10535.

(12) Sorenson, T. A.; Morton, S. A.; Waddill, G. D.; Switzer, J. A. *J. Am. Chem. Soc*. **2002**, *124*, 7604.

(13) Vertegel, A. A.; Bohannan, E. W.; Shumsky, M. G.; Switzer, J. A. *J. Electrochem. Soc*. **2001**, *148*, C253.

(14) Vertegel, A. A.; Shumsky, M. G.; Switzer, J. A. *Electrochim. Acta* **2000**, *45*, 3233.

(15) Vertegel, A. A.; Shumsky, M. G.; Switzer, J. A. *Angew. Chem., Int. Ed*. **1999**, *38*, 3169.

(16) Switzer, J. A.; Liu, R.; Bohannan, E. W.; Ernst, F. *J. Phys. Chem. B*. **2002**, *106*, 12369.

(17) Liu, R.; Bohannan, E. W.; Switzer, J. A.; Oba, F.; Ernst, F. *Appl. Phys. Lett.* **2003**, *83*, 1944.

(18) Liu, R.; Oba, F.; Bohannan, E. W.; Ernst, F.; Switzer, J. A. *Chem. Mater*. **2003**, *15*, 4882.

(19) Brownson, J. R. S.; Georges, C.; Lévy-Clément, C. *Chem. Mater*. **2006**, *18*, 6397; Brownson, J. R. S.; Georges, C.; Lévy-Clément, C. *Chem. Mater*. **2007**, *19*, 3080.

(20) Brownson, J. R. S.; Georges, C.; Larramona, G.; Jacob, A.; Delatouche, B.; Lévy-Clément, C. *J. Electrochem. Soc.* **2008**, *155*, D40.

(21) Cheng, S.; Chen, G.; Chen, Y.; Huang, C. *Optical Materials* **2006**, *29*, 439.

(22) Cheng, S.; Chen, Y.; Huang, C.; Chen, G. *Thin Solid Films* **2006**, *500*, 96.

(23) Partain, L. D. *Solar Cells and Their Applications*; John Wiley & Sons: New York, 1995.

(24) Reddy, N. Koteeswara; Hahn, Y. B.; Devika, M.; Sumana, H. R.; Gunasekhar, K. R. *J. Appl. Phys*. **2007**, *101*, 093522.

(25) Ramakrishna Reddy, K. T.; Koteswara Reddy, N.; Miles, R. W. *Sol. Energy Mater. Sol. Cells* **2006**, *90*, 3041.

(26) Singh, J. P.; Bedi, R. K. *Thin Solid Films* **1991**, *199*, 9.

(27) Mishra, K.; Rajeshwar, K.; Weiss, A.; Murley, M.; Engelken, R. D.; Slayton, M.; McCloud, H. E. *J. Electrochem. Soc*. **1989**, *136*, 1915.

(28) Zainal, Z.; Hussein, M. Z.; Ghazali, A. *Sol. Energy Mater. Sol. Cells* **1996**, *40*, 347.

(29) Omoto, K.; Fathy, N.; Ichimura, M. *Jpn. J. Appl. Phys*. **2006**, *45*, 1500.

(30) Sato, N.; Ichimura, M.; Arai, E.; Yamazaki, Y. *Sol. Energy Mater. Sol. Cells* **2005**, *85*, 153.

(31) Lopez, S.; Ortiz, A. *Semicond. Sci. Technol*. **1994**, *9*, 2130.

(32) Reddy, N. Koteeswara; Reddy, K. T. Ramakrishna *Solid-State Electronics* **2005**, *49*, 902.

(33) Price, L. S; Parkin, I. P.; Hardy, A. M. E.; Clark, R. J. H.; Hibbert, T. G.; Molloy, K. C. *Chem. Mater*. **1999**, *11*, 1792.

(34) Nozaki, H.; Onoda, M.; Sekita, M.; Kosuda, K.; Wada, T. *J. Solid State Chemistry* **2005**, *178*, 245.

(35) Kayes, B. M.; Atwater, H. A.; Lewis, N. S. *J. Appl. Phys*. **2005**, *97*, 114302.

(36) Green, M. A.; Wenham, S. R. *Appl. Phys. Lett*. **1994**, *65*, 2907.

(37) Tian, B.; Zheng, X.; Kempa, T. J.; Fang, Y.; Yu, N.; Yu, G.; Huang, J.; Lieber, C. M. *Nature*, **2007**, *449*, 885.

(38) Tsakalakos, L.; Balch, J.; Fronheiser, J.; Korevaar, B. A.; Sulima, O.; Rand, J. *Appl. Phys. Lett*. **2007**, *91*, 233117/1.

(39) Spurgeon, J. M.; Atwater, H. A.; Lewis, N. S. *J. Phys. Chem. C* **2008**, *112*, 6186.

(40) del Bucchia, S.; Jumas J. C.; Maurin, M. *Acta Crytallogr*. **1981**, *37B*, 1903.

(41) Lefebvre, I.; Szymanski, M. A.; Olivier-Fourcade, J.; Jumas, J. C. *Phys. Rev. B*. **1998**, *58*, 1896.

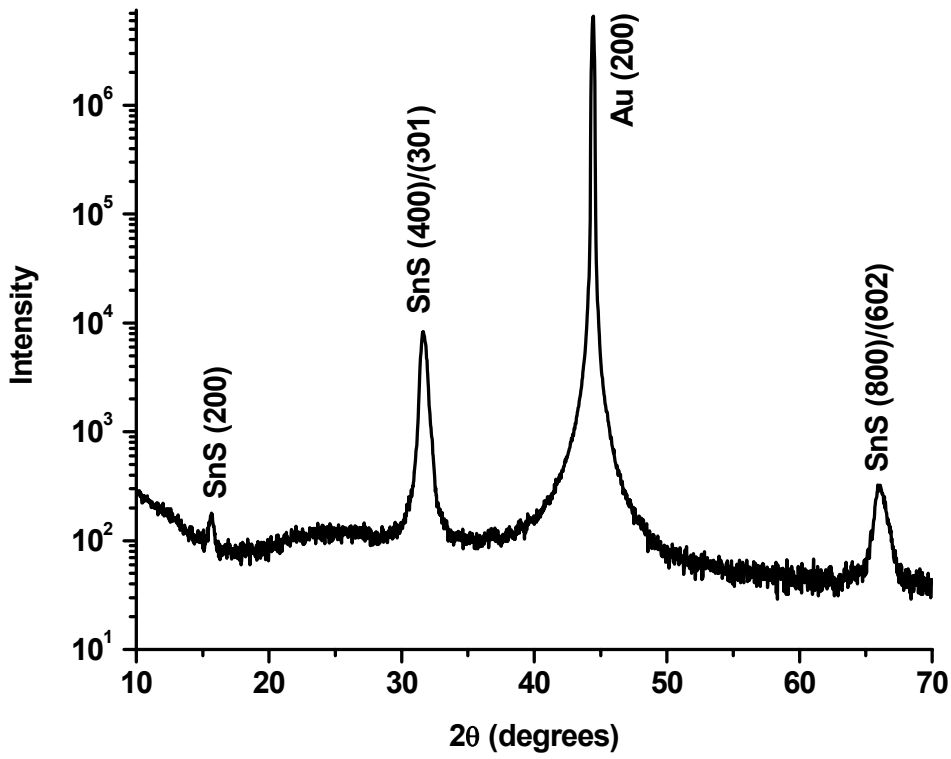

Figure 1: X-ray diffraction θ-2θ scan probing the out-of-plane orientation of an SnS film electrodeposited on Au(100).

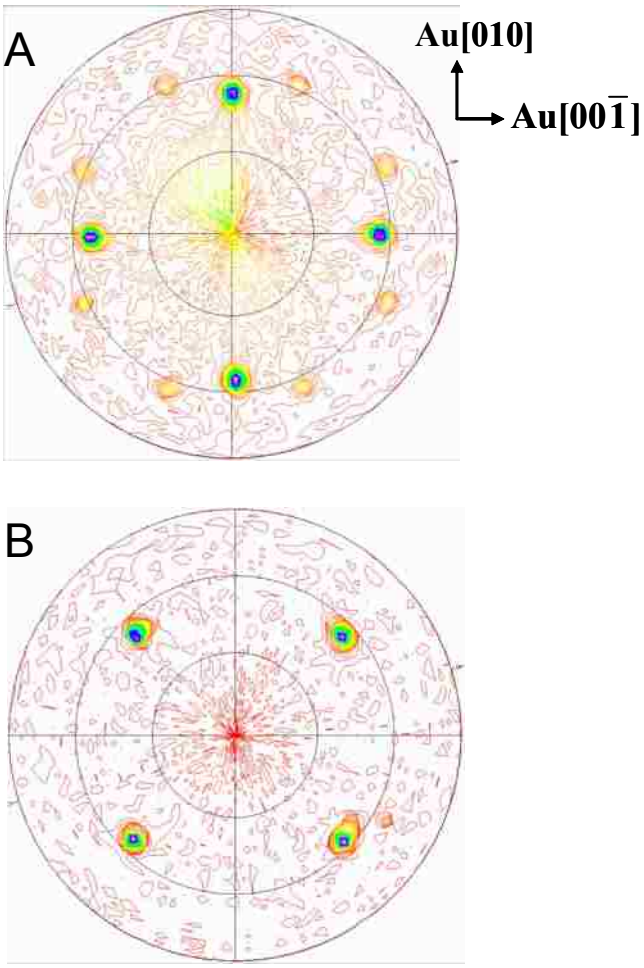

Figure 2: X-ray pole figures of (**A**) SnS film. The four spots at $\chi = 54^{\circ}$ correspond to the angles between the (210) and (200) planes, and the eight spots at $\chi = 64^{\circ}$ correspond to the angles between the (210) and (301) planes. (**B**) Au(100). The four spots at $\chi = 54^{\circ}$correspond to the angle between (111) and (100) planes of Au. The radial grid lines in the pole figures correspond to 30º increments in χ.

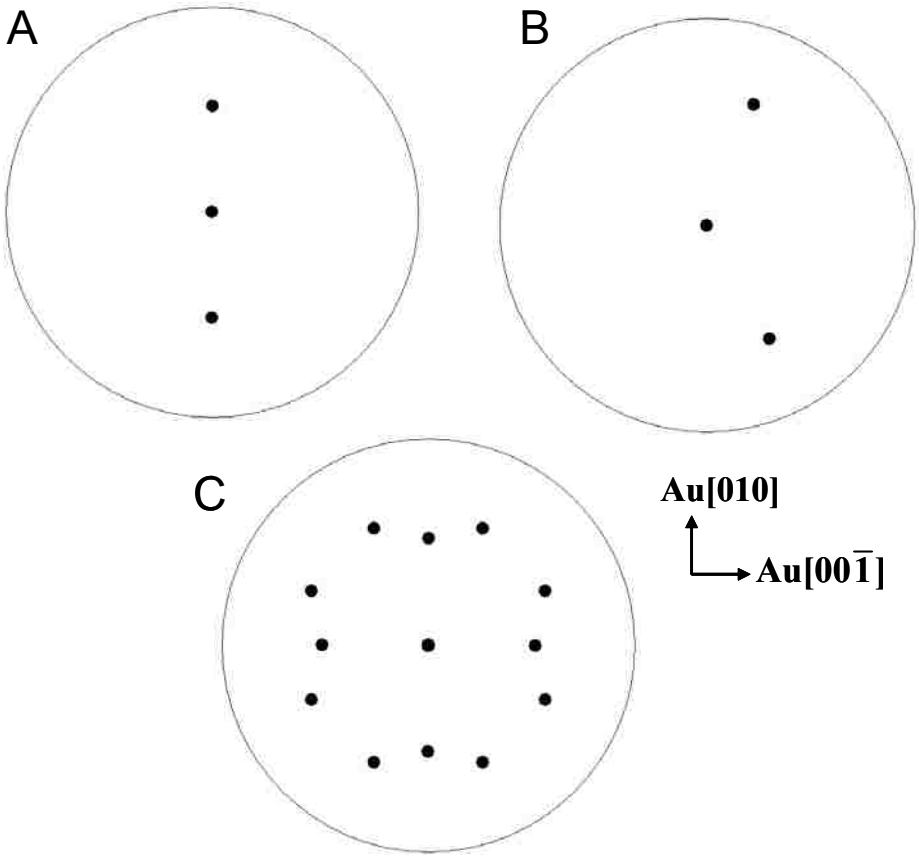

Figure 3: Stereographic projections for (**A**) SnS(100) and (**B**) SnS(301) orientations indicating the positions where the (210)-type reflections should be observed in the pole figure. (**C**) Expected (210) stereographic projection for four domains obtained by overlaying the stereographic projections for the two orientations in (**A**) and (**B**) and rotating by 90º, 180º, 270º.

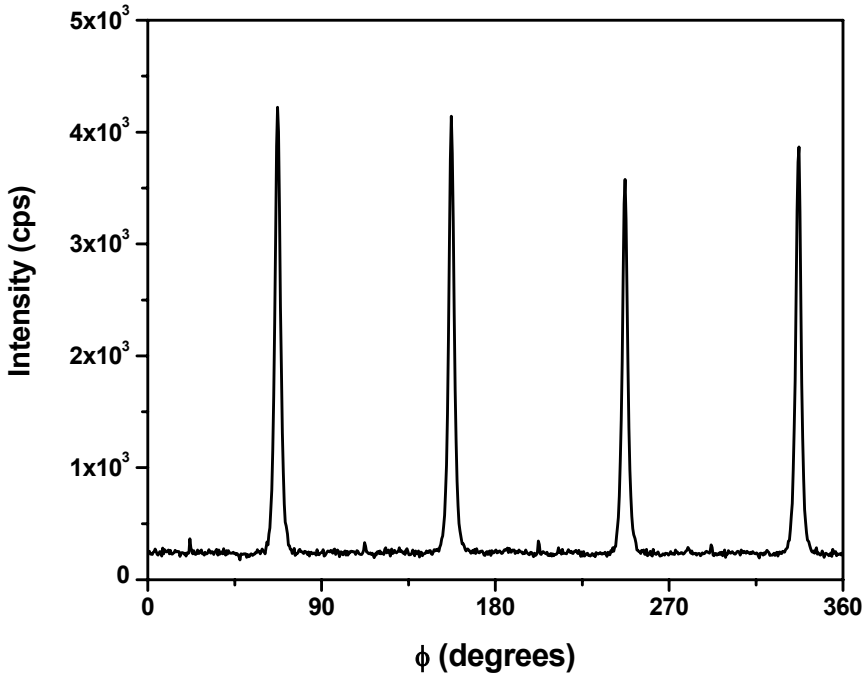

Figure 4: Azimuthal scan for (210) reflection of SnS. The azimuthal scans were obtained by setting 2θ equal to the angle of maximum diffracted intensity for the reflection of interest (2θ = 27.48º) and tilting the sample to the angle, χ, corresponding to the angle between the plane of interest and (100) planes (χ = 54.5º for SnS). The general 4-fold symmetry is observed for SnS. The average fwhm is 3.16º.

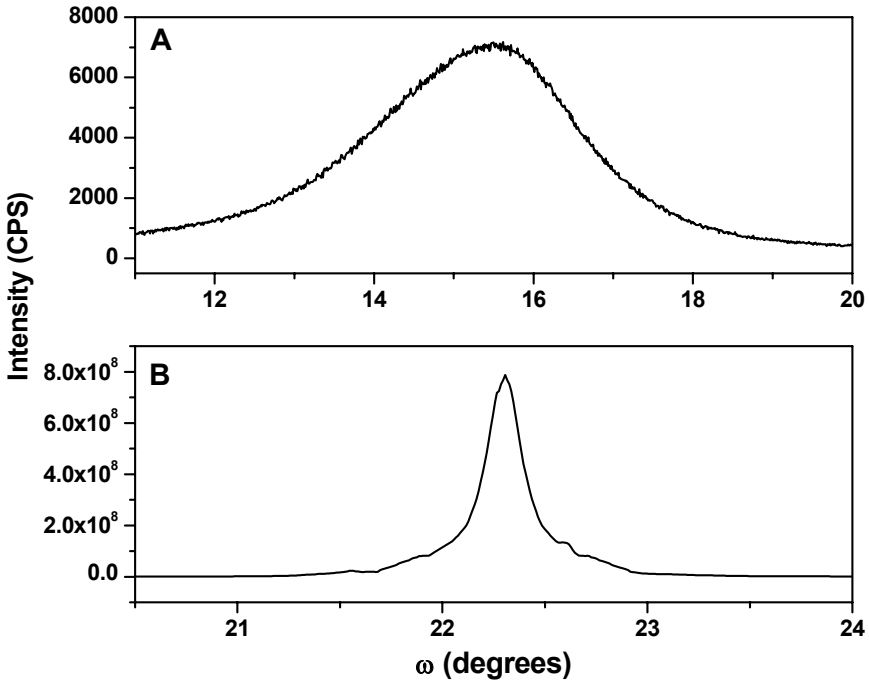

Figure 5: X-ray rocking curves for (A) SnS(400)/(301), and (B) Au(200). Full width at half-maximum (fwhm) is 2.9º for SnS(400)/(301) and 0.23º for Au(200).

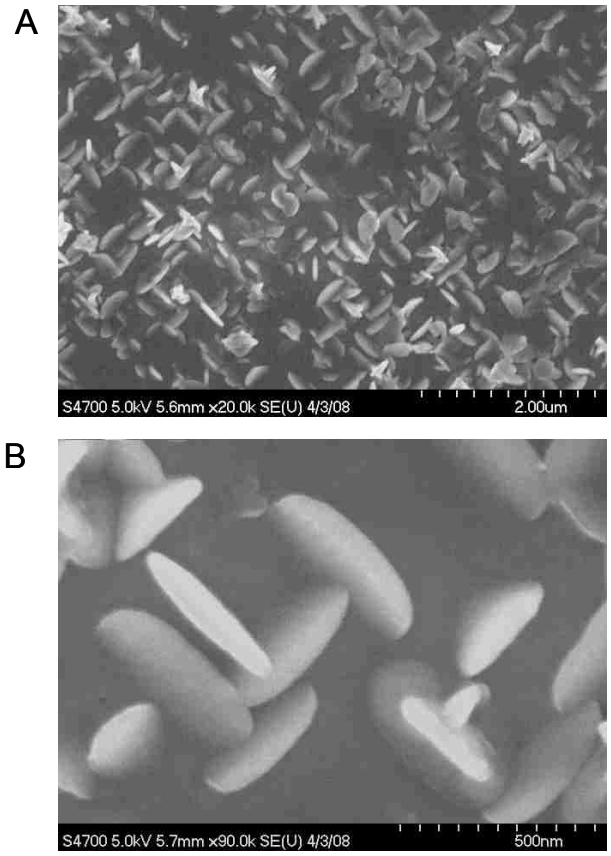

Figure 6: SEM micrographs of an epitaxial film of SnS on Au(100). Micrograph (**B**) is a higher-magnification image of the SnS film shown in (**A**).

APPENDIX

THE EFFECT OF DIFFERENT CATIONS ON LEAD DIOXIDE ELECTRODEPOSITION

Lead dioxide is a highly conductive oxide that is in lead acid batteries and as an anode material for the manufacture of chlorate and perchlorate. Lead dioxide exists in three polymorphs: tetragonal (β-PbO_2), orthorhombic (α-PbO_2), and cubic. The cubic PbO_2 phase is prepared at high pressure.[1] The pure phase of tetragonal or orthorhombic PbO_2 can be obtained via electrodeposition. The deposition of β-PbO_2 occurs from acidic media at high current densities, whereas α-PbO_2 can be obtained from both basic and acidic solutions at low current densities.[2,3]

Although synthesizing tetragonal or orthorhombic PbO_2 polymorphs depends primarily on the solution pH, other parameters such as cations from the solution also affect the PbO_2 structure.[4] For instance, Petersson et al. found that the β-PbO_2 to α-PbO_2 ratio increased with decreasing cation size ($H^+ > Li^+ > Na^+ > K^+$) in perchlorate solutions.[5] Different modifications of PbO_2 also exhibit different physical properties in lead-acid battery applications. β-PbO_2 has a higher discharge capacity, active surface area, and self discharge current than α-PbO_2.[4] Mindt has also studied the electrical property of α- and β-PbO_2. He measured the resistivity of α-PbO_2 films to be 10^{-3} ohm cm, whereas the resistivity of β-PbO_2 films are in the order of 10^{-4} ohm cm.[6] The higher resistivity of α-PbO_2 films result from a lower electron mobility that overcompensates for the effect of a higher electron concentration in this phase.[6] The high electrical

conductivity in PbO_2 most likely comes from the defect chemistry due to non-stoichiometry. However, it is not certain whether the non-stoichiometric composition is caused by cations interstitial or oxygen vacancies.[6,7] Studies by Peterrson et al., however, seem to suggest that PbO_2 phases can be modified by changing cations in the solution.[5]

This study presents some preliminary experimental results on the effects of group I metal ions (Li^+, Na^+, K^+, Cs^+) on the electrodeposition of PbO_2 in highly alkaline solutions. The films were analyzed by chronopotentiometry, X-ray diffraction (XRD), and scanning electron microscopy (SEM). The results are still incomplete and somewhat inconsistent.

EXPERIMENTAL SECTION

The deposition of PbO_2 was carried out at 40 ºC (50 ºC for the reflectance measurements) from a solution of 50 mM $Pb(NO_3)_2$ in 2M XOH (X = Li^+, Na^+, K^+, Cs^+). The working electrode consisted of a stainless steel electrode (area = 1.77 cm^2). A stainless steel wire fitted around the edge of the substrate served as an electrical contact during deposition. The films were deposited on one side of the crystal using the meniscus method. The counter electrode was a Pt wire. A constant current density of 1 mA/cm^2 was applied to the working electrode using an EG&G Princeton Applied Research model 273A potentiostat/galvanostat. To measure the reflectance spectra, the films were deposited on the large area stainless steel plates (area = 7.5 cm^2). Then, an insulating glass slide was attached to the deposits with 3M super glue and used to pull them away from the plates to avoid interference due to reflectance of the stainless steel.

X-ray diffraction measurements were taken with a high-resolution Philips X'Pert diffractometer. The film XRD scan was obtained using Cu Kα source radiation. The

SEM images were taken with a Hitachi S-4700 cold field emission scanning electron microscope. The reflectance spectra were measured at wavelength from $\lambda = 250$ nm to $\lambda = 3000$ nm using a Cary 5 spectrophotometer.

RESULTS AND DISCUSSION

The electrodeposited orthorhombic α-PbO_2 films from a highly alkaline NaOH solution exhibit a strong out-of-plane [100] texture.[3] The XRD pattern exhibits no evidence of a tetragonal or cubic phase, as shown in Figure 1. Other experimental results also reveal that PbO_2 films grown from 2M LiOH, KOH, or CsOH solutions also deposited with an orthorhombic structure. Comparison of the (200) peak in the XRD patterns of the films grown from Li^+, K^+, and Cs^+ does not show any evidence for the peak shift. The potential versus time plot in Figure 2 shows that, at the same current density and bath temperature, a film in LiOH solution deposited with the potential approximately 150 mV higher than other cations. Films grown from just 0.1M $Pb(NO_3)_2$ solution had mixed α- and β-PbO_2. However, when the concentration of LiOH was varied, the XRD patterns show different results. Figure 3 shows XRD θ-2θ scans of PbO_2 grown from 0.5 to 2.0 M LiOH. The asterisks denote the stainless steel substrate peaks. Films grown from 1.5 and 2 M LiOH show only a strong (200) out-of-plane orientation at $2\theta = 36^\circ$, which is similar to the α-PbO_2 film deposited from NaOH or KOH. The film changes from crystalline to amorphous when 1 M LiOH is used indicated by an amorphous hump in the XRD pattern. When the film is deposited from 0.5 M LiOH, the XRD pattern shows that there is reflection from β-PbO_2 in addition to the α-PbO_2 phase. Inductively coupled plasma mass spectrometry (ICPMS) was used to determine the Li content in the samples. The ICPMS results reveal that, for PbO_2

deposited from 0.5, 1.0, and 1.5 M, the Li content in the film are 3.3 mol%, 9.4 mol%, and 13 mol%, respectively, compared to Pb. However, the XRD results revealed that the film structures grown from LiOH solutions are not consistent. Some old samples grown from 2 M LiOH exhibited pure β-PbO_2. The author has attempted to deposit pure β-PbO_2 structure, but it is not reproducible. Mindt suggested that, using low concentration of Pb^{2+} and current density seem to promote the β-PbO_2 growth.[6] It should be noted that, when LiOH is mixed with any other cations in solutions, the results always give an amorphous material as shown in Figure 4. The mixture of cations other than Li^+ always produces α-PbO_2.

Figure 5 shows the scanning electron microscopy (SEM) images of films grown from different cations in the solutions. Figure 5a is an SEM image of an α-PbO_2 nanostructure from 2M NaOH. This film grows with a strong out-of-plane (200) orientation, as shown in Figure 1. Films of α-PbO_2 grown from KOH and CsOH show similar morphologies. An amorphous film grown from a LiOH solution shows a compact structure, but its particle sizes are not uniform as shown in Figure 5b. Figure 5c shows an SEM image of an amorphous film deposited from LiOH and NaOH mixture. The image reveals a very compact structure with uniform, nano-sized particles.

The reflectance spectra for 3 μm thick α-PbO_2 films from different cations are shown in Figure 6. Each film is deposited in 2M XOH at 5 mA/cm^2. The reflectance in the visible range is low, but increases rapidly in the near-infrared due to the plasma edge of the free electrons. The wavelength where the edge occurs gives the information about the carrier concentration. The steepness of the plasma edge is sensitive to the electron mobility. The steeper the edge, the higher the mobilities.[8] From Figure 6, a PbO_2 film

deposited from LiOH has the lowest carrier concentration and the lowest electron mobility. Films deposited from NaOH, KOH, and CsOH have similar carrier concentrations and mobilities. It should be noted that, although the optical spectrum of the film from Li solution is very different from the others, x-ray diffraction shows that this particular film also has α-PbO_2 structure with no other phases present.

REFERENCES

1. Syono, Y.; Akinoto, S. *Mater. Res. Bull*. **1968**, *3*, 153.

2. Hampson, N. A. *The Electrochemistry of Lead*, Kuhn, A. T., Editor, Academic Press, London (1979).

3. Vertegel, A. A.; Bohannan, E. W.; Shumsky, M. G.; Switzer, J. A. *J. Electrochem. Soc*. **2001**, *148*, C253.

4. Ahlberg, E.; Berghult, B. *J. Power Sources* **1990**, *32*, 243.

5. Petersson, I.; Ahlberg, E.; Berghult, B. *J. Power Sources* **1998**, *76*, 98.

6. Mindt, W. *J. Electrochem. Soc*. **1969**, *116*, 1076.

7. Ruetschi, P. *J. Electrochem. Soc*. **1992**, *139*, 1347.

8. Van Leeuwen, R. A.; Hung, C-J.; Kammler, D. R.; Switzer, J. A. *J. Phys. Chem*. **1995**, *99*, 15247.

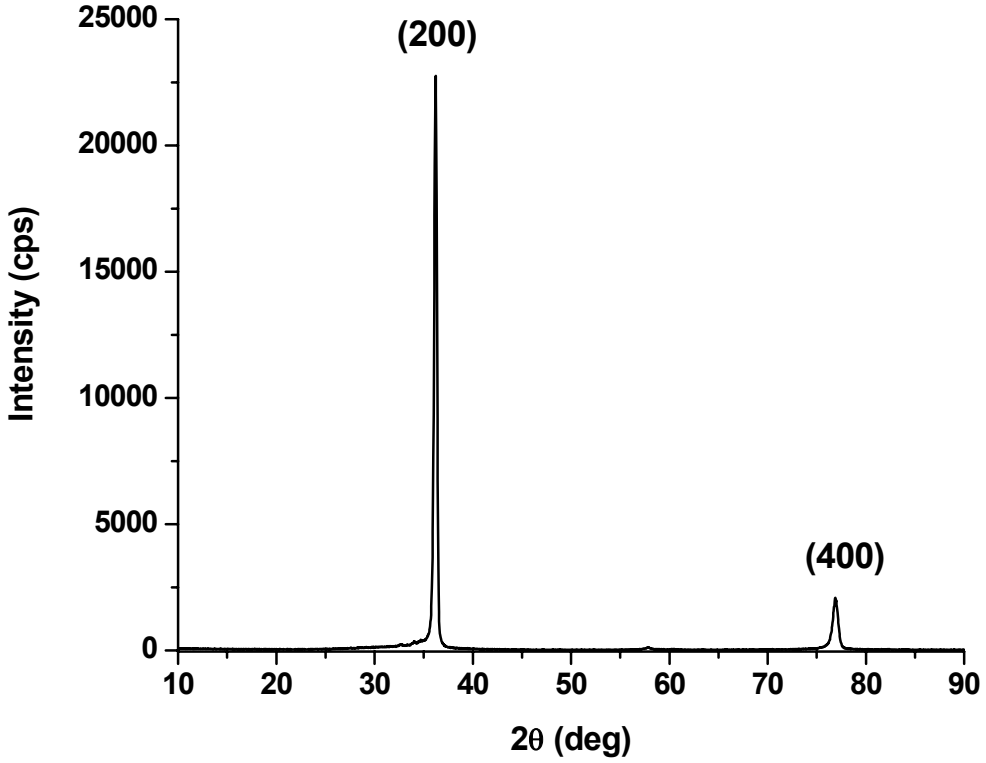

Figure 1: X-ray diffraction θ-2θ scan probing the out-of-plane orientation of α-PbO_2 film 50 mM $Pb(NO_3)_2$ in 2M XOH (X = Na^+, K^+, Cs^+).

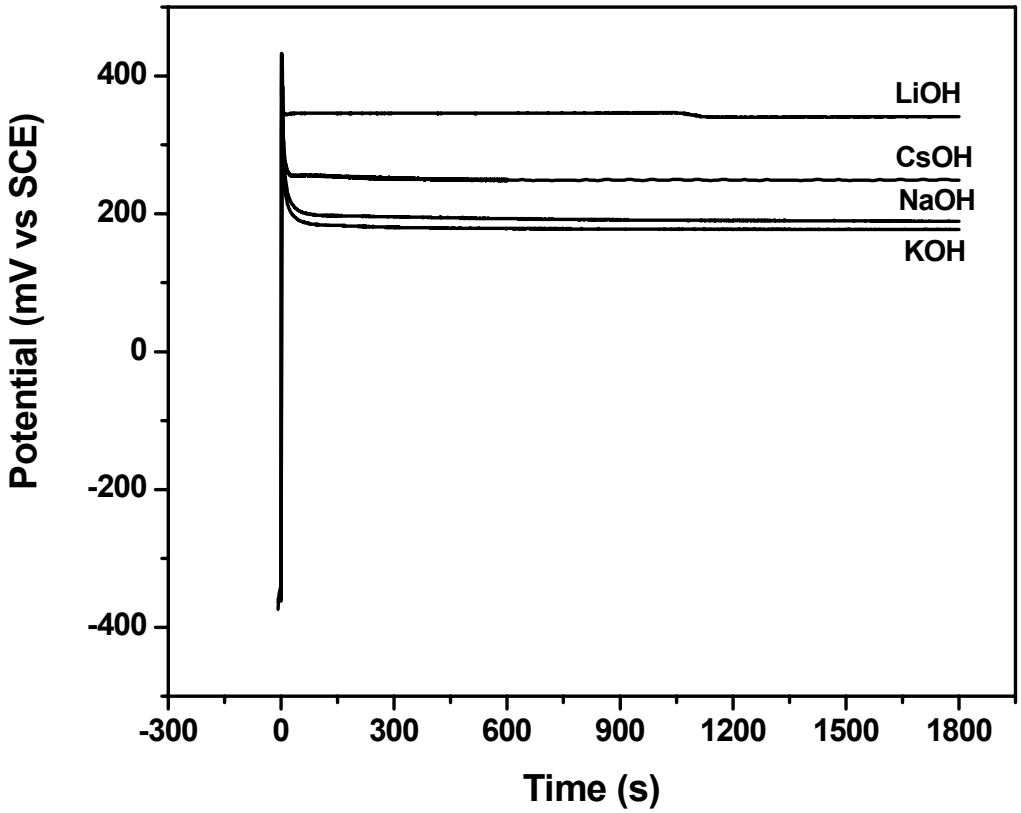

Figure 2: Chronopotentiometry of 50 mM $Pb(NO_3)_2$ solution in 2M XOH (X = Li^+, Na^+, K^+, Cs^+).

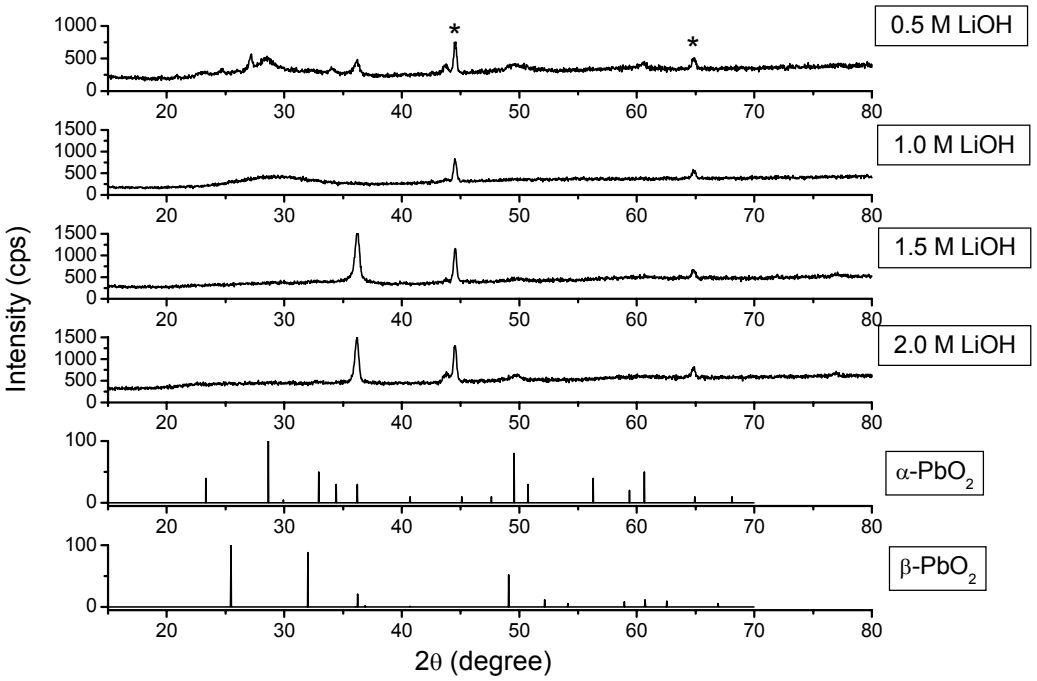

Figure 3: X-ray diffraction θ-2θ scan probing the out-of-plane orientation of α-PbO_2 films deposited from different concentration of LiOH

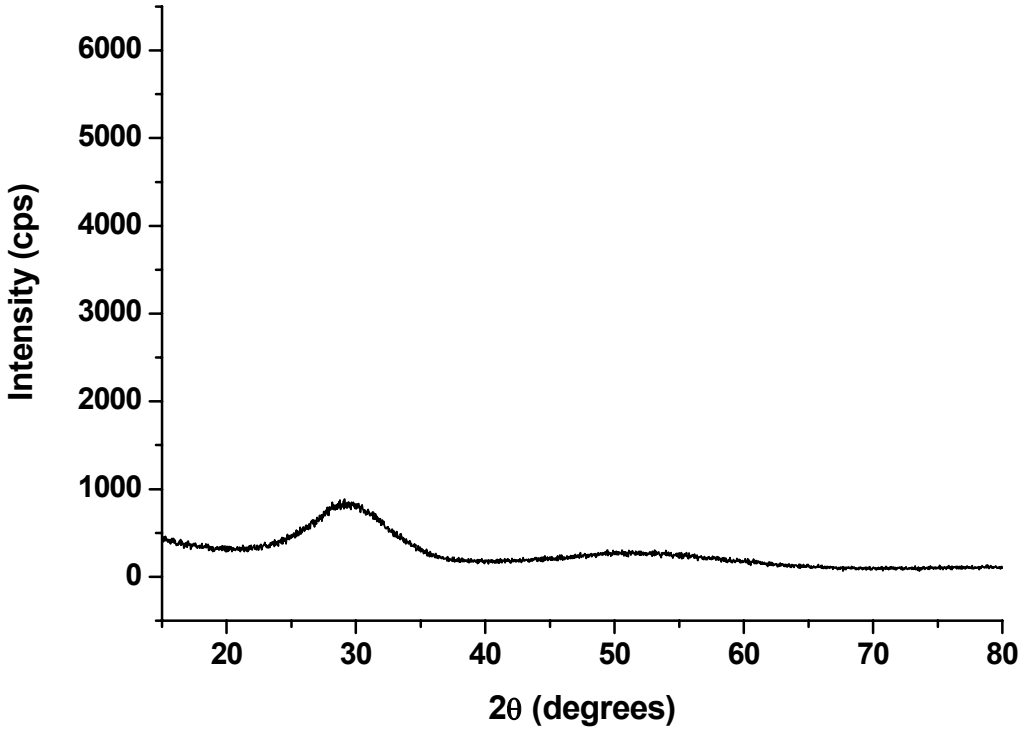

.

Figure 4: X-ray diffraction θ-2θ scan of a PbO_2 film deposited from a mixture of 1M LiOH + 1M NaOH at 1 mA/cm^2.

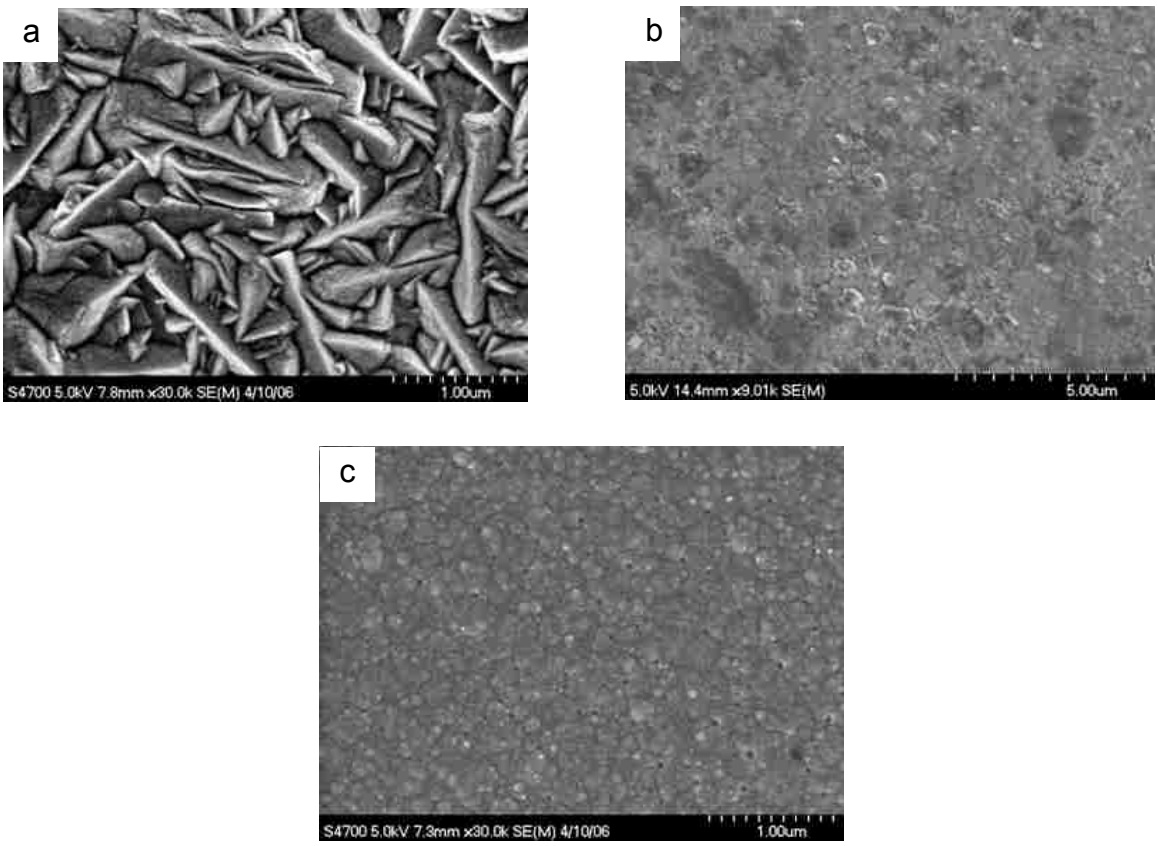

Figure 5: SEM micrographs of PbO_2 deposited from (a) 2M NaOH, (b) 2M LiOH, and (c) a mixture of 1M LiOH+ 1M NaOH.

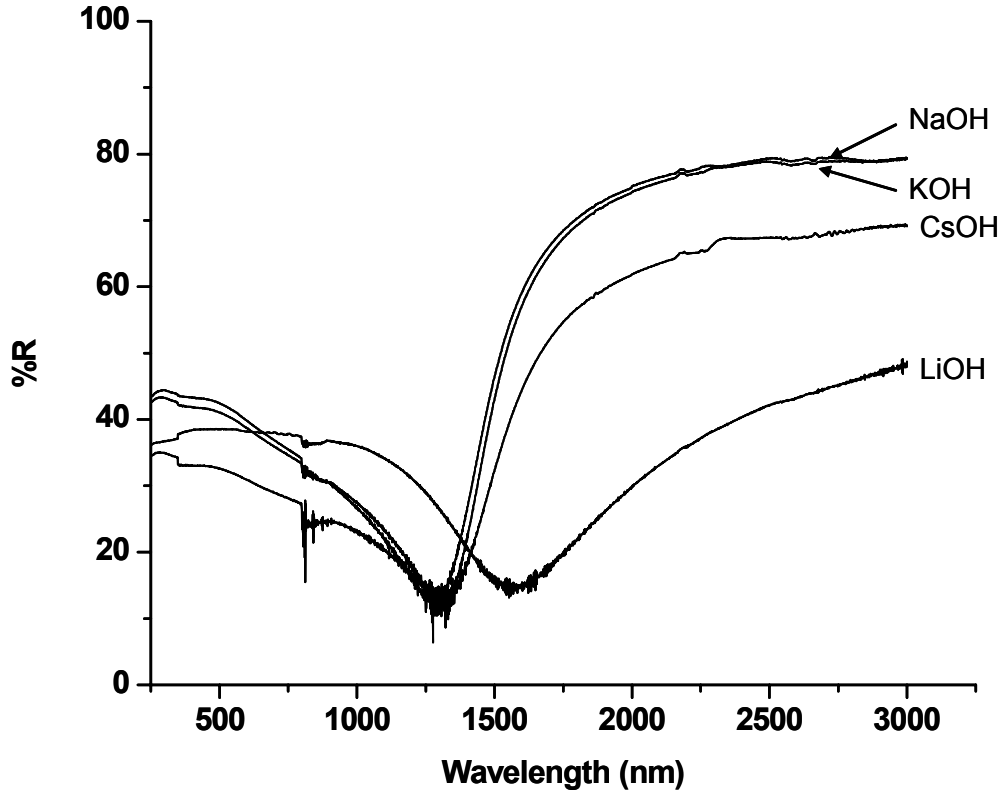

Figure 6: Reflectance spectra for a 3 μm thick α-PbO_2 films from 2M XOH (X = Li^+, Na^+, K^+, and Cs^+).

VITA

Sansanee Boonsalee was born in Uttaradit, Thailand, on October 15, 1977. After finishing her high school education at Triam Udom Suksa School in Bangkok, she received a scholarship from the Royal Thai Government to continue her education in the United States.

She spent her first year in the United States as a high school senior at Choate Rosemary Hall in Connecticut. Subsequently, she enrolled in the chemistry program at the University of Chicago, Illinois, from which she received her Bachelor's degree in chemistry in 2001. She entered the PhD program in chemistry at the Missouri University of Science and Technology (formerly known as the University of Missouri-Rolla) in 2001 and graduated in May 2008.